Volume 41, Issue 8 2010

JOURNAL OF HEAT TRANSFER RESEARCH

SERGUEI A. ZHDANOK
EDITORS-IN-CHIEF

begell house, inc.
publishers

AIMS AND SCOPE

Sponsored by the Heat Transfer division of the American Society of Mechanical Engineers, *Heat Transfer Research* presents translations of important technical and experimental papers selected from the foremost Russian, Ukrainian and Belarussian periodicals, conference proceedings and academic laboratory reports. The journal covers the entire field of heat transfer, including conduction, convection and radiation, boiling phenomena, heat exchanger design and testing, heat transfer in nuclear reactors, mass transfer, geothermal heat recovery, and thermophysical properties of materials, as well as the pertinent areas of fluid mechanics.

HEAT TRANSFER RESEARCH

Volume 41, Number 8 2010

Special Issue 3 of 5:
Turbine-09 symposium, Antalya, Turkey, August 9–14, 2009

Guest Editors:
Terrence W. Simon & Richard J. Goldstein

801 Preface: Gas Turbine Heat Transfer

803 Recent Studies in Turbine Blade Internal Cooling
J-C. Han and M. Huh

829 Heat Transfer and Flow Testing in Engine HP Turbine Cooling System Development
P. Ireland, V. Mittal, D. Jackson, and H. Namgoon

849 Trailing Edge Film Cooling of Gas Turbine Airfoils-Effects of Ejection Lip Geometry on File Cooling Effectiveness and Heat Transfer
T. Horbach, A. Schulz, and H-J. Bauer

867 An Experimental Study of Airfoil and Endwall Heat Transfer on a Linear Turbine Blade Cascade-Secondary Flow and Surface Roughness Effects
M. Lorenz, A. Schulz, and H-J. Bauer

889 Experimental Study of Heat Transfer from Impinging Jet with Upstream and Downstream Crossflow
D. Thibault, M. Fénot, G. Lalizel, and E. Dorignac

901 Experimental and Theoretical Analysis of Heat Transfer Characteristics in a Rectangular Duct with Jet Impingement
U.Uysal, F. Sahin, and M.K. Chyu

Gas Turbine Heat Transfer

This issue has papers selected by the Scientific Committee from the symposium Turbine-09 sponsored by the International Center for Heat and Mass Transfer (ICHMT). *Turbine-09* was held in Antalya, Turkey, August 9–14, 2009. It was the third symposium related to heat transfer in high-performance gas turbines sponsored by the ICHMT. The first, held in Marathon, Greece, in August 1992, resulted in the book *Heat Transfer in Turbomachinery*. The second, Turbine 2000, conducted in Cesme, Turkey, in August 2000, was published in the book *Heat Transfer in Gas Turbine Systems.* The three symposia offered invited keynote lectures and contributed papers by some of the world's best-known authorities on gas turbine heat transfer. Each of the two proceedings volumes and these special issues (Vol. 41, Nos. 6–8, 2010 and Vol. 42, Nos. 1 and 2, 2011) contain a wealth of information from key industrial, academic, and nonprofit laboratories.

The objective of the symposia and of these special issues is to provide an opportunity to present and review the most recent developments in heat transfer and thermal control applied to modern, high-temperature gas turbine systems. Presented are: experimental results and techniques, computational studies and methods, and design recommendations. Aspects of heat transfer in rotating machinery include:

- combustor and transition section heat transfer,
- heat exchange to turbine airfoil and endwall surfaces within the gas path,
- stator internal heat transfer,
- disk cavity and blade internal flow and heat transfer,
- innovative cooling techniques, and
- heat exchange in turbines with combined cycles.

The results published in these issues should be valuable to researchers in heat transfer as well as to designers of gas turbine systems.

The papers for these special issues were selected from the symposium papers by the International Scientific Committee of the Symposium:

- Sumanta ACHARYA, Louisiana State University, U.S.A.
- Tony ARTS, Von Karman Institute for Fluid Dynamics, BELGIUM
- David BOGARD, University of Texas, U.S.A.
- Ronald BUNKER, General Electric Company, U.S.A.
- Cengiz CAMCI, Pennsylvania State University, U.S.A.
- Ping-Hei CHEN, National Taiwan University, TAIWAN
- Minking CHYU, University of Pittsburgh, U.S.A.
- Eva DORIGNAC, LET ENSMA, University of Poitiers, FRANCE

- Ken-ichi FUNAZAKI, Iwate University, JAPAN
- Richard J. GOLDSTEIN, University of Minnesota, U.S.A.
- Je-Chin HAN, Texas A&M University, U.S.A.
- Alexander I. KIRILLOV, St.Petersburg State Polytechnic University, RUSSIA
- Lee S. LANGSTON, University of Connecticut, U.S.A.
- Philip LIGRANI, Oxford University, U.K.
- Joon Sik LEE, Seoul National University, SOUTH KOREA
- Alexander I. LEONTIEV, Moscow State Technical University, RUSSIA
- Francesco MARTELLI, University of Florence, ITALY
- Ricardo MARTINIZ_BOTAS, Imperial College, U.K.
- Pierre MILLAN, ONERA — CERT, FRANCE
- Hee-Koo MOON, Solar Turbines Inc., U.S.A.
- J. Michael OWEN, University of Bath, U.K.
- B.V.S.S.S. PRASAD, Indian Institute of Technology-Madras, INDIA
- Heinz-Peter SCHIFFER, Technische Universität Darmstadt, GERMANY
- Achmed SHULTZ, University of Karlsruhe, GERMANY
- Terrence SIMON, University of Minnesota, U.S.A.
- Kenichiro TAKEISHI, Osaka University, JAPAN
- Zhi TAO, Beihang University, CHINA
- Bernhard WEIGAND, Stuttgart University, GERMANY

Symposium Co-Chairs and Journal Guest Editors:
Prof. Dr. Terrence W. Simon and Prof. Dr. Richard J. Goldstein
Department of Mechanical Engineering
University of Minnesota
Minneapolis MN 55455 USA

Heat Transfer Research, 2010, Vol. 41, No. 8

Recent Studies in Turbine Blade Internal Cooling

JE-CHIN HAN[a*] and MICHAEL HUH[b]

[a]Turbine Heat Transfer Laboratory,
Department of Mechanical Engineering,
Texas A&M University, College Station,
Texas 77843-3123, USA

[b]Department of Mechanical Engineering,
The University of Texas at Tyler,
Tyler, Texas 75799, USA,
MHuh@slb.com

Gas turbines are used extensively for aircraft propulsion, land-based power generation, and industrial applications. The turbine inlet temperatures are far above the permissible metal temperatures. Therefore, there is a need to cool the blades for safe operation. Modern developments in turbine cooling technology play a critical role in increasing the thermal efficiency and power output of advanced gas turbine designs. Turbine blades and vanes are cooled internally and externally. This paper focuses on turbine blade internal cooling. Internal cooling is typically achieved by passing the coolant through several rib-enhanced serpentine passages inside the blades. Impinging jets and pin fins are also used for internal cooling. In the past 10 years there has been considerable progress in turbine blade internal cooling research and this paper is limited to reviewing a few selected publications to reflect recent developments in this area. In particular, this paper focuses on the effects of channel inlet geometry, sharp 180^o turning, and channel cross-section aspect ratio on the coolant passages heat transfer at high rotation number conditions. Rotation effects on the blade leading-edge triangular-shaped channel and trailing-edge wedge-shaped channel with coolant ejection are included.

* * *

Keywords: gas turbines, blade cooling, totating effect

*Address all correspondence to Je-Chin Han E-mail: jc-han@tamu.edu

ISSN1064-2285

1. INTRODUCTION

The forced cooling of gas turbine blades began with crude designs that consisted of circular radial holes that allowed for forced air to convect heat from the blade walls. These simple designs were the first attempts to forcefully cool the turbine blade. As rudimentary as these designs were, the benefits of increasing power and efficiency were quickly realized by the ability to increase the turbine entry temperature. Decades have passed since, and through research, revolutionary steps have been made to allow for ever increasing turbine entry temperatures. Advanced gas turbine blade designs now employ a variety of heat transfer enhancement methods and techniques as shown in Fig. 1. At the leading edge of the airfoil, where heat loads are extreme, internal impingement jets are used to provide high heat transfer coefficients. Shaped internal cooling passages occupy the mid-region of the airfoil. The walls of these passages are lined with turbulence promoters (ribs) to break the hydrodynamic boundary layer and increase near wall turbulent mixing; all resulting in greater heat transfer. The trailing edge portion is susceptible to failure due to the thin material structure. This region is cooled by internal channels incorporating pin fins, ribs and high velocity cooling air slot ejection into the mainstream. Internal convection heat transfer is the foundation for maintaining the life of the turbine blade. Building upon the advancements made through research, pressure losses in the internal cooling channels have decreased. This has allowed for film cooling to be introduced as an additional method to protect the blade. Cooling air that passes through the internal cooling channels is, at some point or another, expelled to the mainstream by means of cooling holes. To further protect the leading edge of the airfoil, shower-head film cooling holes are utilized. The pressure and suction surfaces of the airfoil are covered with strategically placed discrete film cooling holes. The tip region of the blade also utilizes coolant ejection to protect the blade from high velocity leakage flows that im-

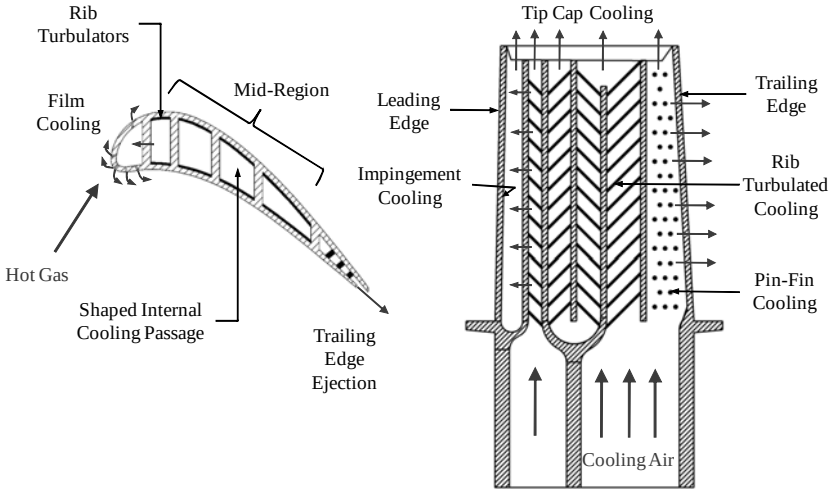

Fig. 1. Internal cooling techniques for gas turbine blades.

pose severe heat loads. Sophisticated cooling schemes and techniques have been developed for both internal and external cooling and are reported in [1]. The authors provide a compilation of the work that has been performed up to the year 2000. Later, Han and Wright [2] focused on the research associated solely with internal heat transfer related to stator vanes and rotor blades. The design of the stator vane is considerably different compared to the rotor blade. Even more important is the difference due to rotation. The interested reader is referred to the prior literature for that topic. This paper is devoted to reviewing the research work performed since 2000, and focuses on advancements made in regard to internal heat transfer of rotor blades. More specifically, the advancements that have been made in achieving more realistic engine parameters during experiments such as high rotation numbers, the influence of developing flow on heat transfer with rotation, cooling channel cross-sectional geometry effects, and heat transfer on the tip inside of the 180^{o} sharp turn along with the sharp turn effects.

2. SHAPED INTERNAL COOLING PASSAGE HEAT TRANSFER

2.1 Modeling Internal Cooling Passages

The gas turbine blade mid-region is cooled convectively with a compressor-bled air passing through the complex shaped internal cooling channels. These channels are specifically designed to fit the blade profile and have irregular cross sections. Since the design of these channels varies from blade to blade, and increased complexities of the flow field are introduced by irregular cross-sectional shapes, researchers have mostly used square and rectangular channels as models in the study of heat transfer. The square and rectangular channels are categorized by aspect ratio as seen in Fig. 2. At this point, it is important to make a comment in regard to aspect ratio definition. There is not a standard that is consistently used in publications for the definition of aspect ratio. Common terminology used to describe the channel and the aspect ratio

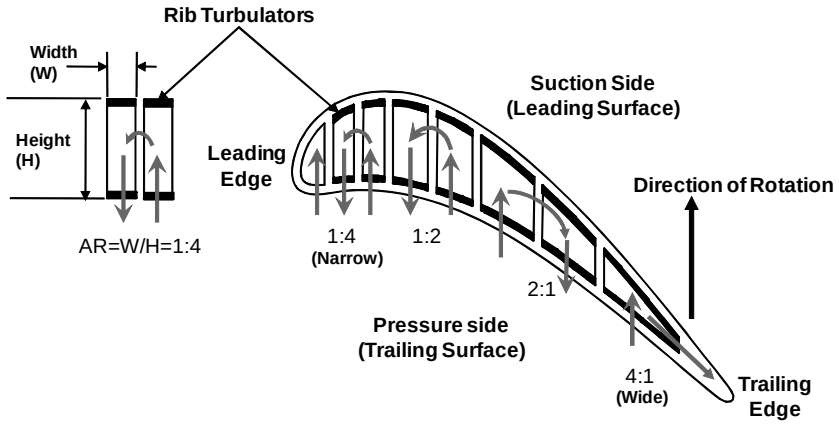

Fig. 2. The various aspect ratios of gas turbine blade internal cooling channels.

is large, small, wide, narrow, etc. Furthermore, some research groups may define the aspect ratio as the ratio of the channel height to the channel width, while others consider the opposite. Even more interesting is that for the same given side of a channel, one group may refer to it as the width while others refers to it as the height. Differences even occur within research groups. Thus, caution is advised when surveying the literature and classifying the channel geometry. It is advisable to consider each journal article by itself. In this review paper, the channel aspect ratio (AR) is defined as the ratio of the channel width (W) to the channel height (H) or AR = W/H. Furthermore, the channel height is the distance from the suction surface to pressure surface as seen in Fig. 2. The channel width is the dimension of the surface on which the rib turbulators are cast. A final point of clarification is in regard to the distinction between leading edge, leading surface, trailing edge and trailing surface. Commonly, the phase leading surface has been used interchangeably with suction side/surface. Likewise, trailing surface is interchangeable with the pressure side/surface.

The internal cooling channels near the blade leading edge have been modeled as narrow rectangular channels with AR = 1:4 and 1:2 [3–6]. The cross section of the cooling channels changes along the cord length of the blade due to the blade profile. In the middle of the blade, the channels become squarer in shape, and studies have modeled this region with square cross sections [7]. Square channels also serve to provide for a more fundamental study by eliminating a parameter since all sides of the channel are of the same dimension. Towards the trailing edge, the channels have wider aspect ratios of AR = 2:1 and 4:1 [8, 9]. An experimental study of the effects of the buoyancy parameter in various aspect ratio channels was performed by Fu et al. [10]. The study considered five different aspect ratio channels (AR = 1:4, 1:2, 1:1, 2:1, and 4:1) with a fully developed flow inlet condition. The results showed that the overall levels of heat transfer enhancement (Nu/Nu_0) for all the ribbed channels were comparable. However, significant differences arose in the pressure losses incurred in each of the channels. The 1:4 channel incurred the lowest pressure penalty; therefore, the thermal performance (TP) of the 1:4 channel was superior to the 1:2, 1:1, and 2:1 channels. It is worth noting that the thermal performance takes into account the pressure penalty (f/f_0) and the heat transfer enhancement, and for a constant pumping power, $TP = (Nu/Nu_0)/(f/f_0)^{1/3}$.

2.2 Rib Turbulated Cooling

Rib turbulators are also widely known as "trip strips" as they simply trip the boundary layer in the internal cooling channel. After the boundary layer is disturbed, redevelopment begins, and high heat transfer is associated with the thin boundary layer. Figure 3 presents conceptual views on the most notable characteristics of the effects of ribs on the mainstream flow. As shown in Fig. 3a, as the mainstream flow near the surface of the channel passes over the rib, it separates from the surface. This separation results in relatively low heat transfer just downstream of the rib, due to a relatively hot cell being trapped in the area of recirculation. However, when the

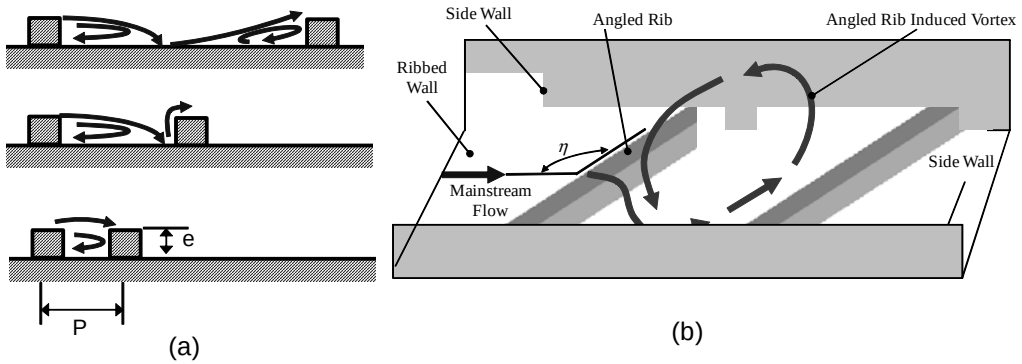

Fig. 3. Rib effects on mainstream flow and secondary flow behavior.

mainstream flow reattaches to the surface (between two ribs), this is an area of relatively high heat transfer due to impingement of the mainstream flow on the surface. This pattern of separation, recirculation, and reattachment continues throughout the channel along with the pattern of repeating ribs.

It is important then to consider the rib spacing effects. The ideal rib spacing is large enough for the mainstream flow to reattach to the surface between the ribs (high heat transfer), but not so large that the boundary layer is allowed to develop freely. By allowing the mainstream flow to develop freely, the advantage of the thin boundary layer is lost. In addition to general flow separation and reattachment, the rib turbulators increase turbulent mixing. The relatively hot fluid near the surface is continuously mixing with the relatively cooler core fluid near the center of the channel. This mixing also serves to increase the heat transfer from the channel wall. It has been shown that the ideal spacing for orthogonal ribs is approximately $P/e = 10$. As conceptually shown in Fig. 3a, with a $P/e = 10$ spacing, sufficient space is given between the ribs for reattachment of the flow between the ribs. However, as the ribs continue to move closer together, the reattachment area becomes jeopardized. After separation, the flow may impinge on the next downstream rib or the flow may completely pass over the next rib, completely eliminating the desired flow behavior.

The application of rib turbulated cooling has been a major milestone in the advancement of turbine blade designs. Even more so, the research work that led to placing the ribs at angle has allowed for an increase in channel heat transfer while simultaneously reducing the pressure losses. This is due to the additional secondary flow induced by the angle of the ribs. The fluid near the surface follows the angle of the rib until it impinges on the side wall as can be seen in Fig. 3b. After impingement on a side wall, the rib-induced secondary flow returns to the other side wall, creating a vortex. This behavior is identical on both the leading and trailing surfaces, so two counter-rotating vortices form in the channel.

Many studies [11–18] have been published that have investigated various aspects of ribbed channel heat transfer and fluid flow. More recently Rallabandi et al. [19] performed systematic experiments to measure heat transfer and pressure losses in a

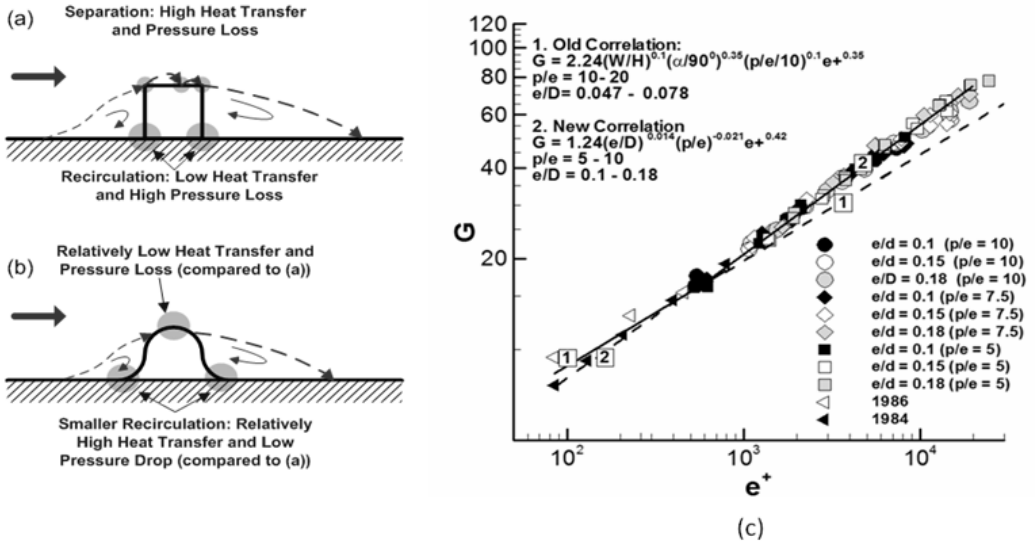

Fig. 4. Profiles of ribs studied (a, b) and heat transfer roughness variation with Reynolds number roughness for sharp ribs (c) [19].

stationary square channel with square/sharp edged ribs at a wide range of Reynolds numbers ranging from 30 K to very high flows of Re = 400 K. These high Reynolds numbers are typical of land-based turbines. Later, Rallabandi et al. [20] included round edged ribs as well to account for manufacturing effects. Figure 4a and b shows the rib profiles that were studied in the respective publications. In both studies, an array of blockage ratios and rib spacing ratios were considered. The correlations of Han [21–23] were modified to fit into the new extended parameter range. The parameters G and R (heat transfer roughness and friction roughness functions, respectively) have been used in literature to absorb the effect of rib height (e/D) and Reynolds number (Re) into one variable. The heat transfer roughness (G) is an indicator of thermal performance. For large values of G, thermal performance will be low. Thus, it is desirable to achieve as low a value for G as possible. These parameters (G and R) have been correlated with e^+ (a nondimensional roughness Reynolds number) and P/e. Expressions of the form $R = C_1(P/e)^m$ and $G = C_2(P/e)^m(e^+)^n$ have typically been utilized to accurately correlate experimental data. In their studies, however, the blockage ratio (e/D) had to be explicitly included in the correlations for R and G. Figure 4c presents the results from the authors work using sharp ribs. Notable is the very well correlating of the heat transfer roughness (G) with the roughness Reynolds number (e^+) which is defined as $e^+ = (e/D)(\mathrm{Re})(f/2)^{1/2}$. This work has extended the e^+ range of previous work from $e^+ = 1000$ (Re = 70 K, $e/D = 0.078$) to $e^+ = 18000$ (Re = 400 K, $e/D = 0.18$). Figure 4b indicates that the correlations for R and G do not agree with the earlier published correlations in the extended range. The authors attribute this to the parameter range differences, specifically the e/D ratio which was considerably larger than in prior work. The authors further explain that the

turbulent boundary layer universal logarithmic velocity profile assumption is valid when the surface roughness is relatively small. Larger rib thickness could however invalidate this assumption owing to greater form drag caused by flow separating and reattaching due to the rib in comparison with the skin friction. This causes a dependence of R and G on e/D, as well as on e^+. However, round edged ribs results coincidently showed agreement between prior correlations and the new data in the extended range. With round edged ribs, the friction was lower, resulting in a smaller pressure drop. In fact, the friction performance for the round edge ribs was quite similar to smaller ribs. The heat transfer coefficients for the round ribs, on the other hand, were similar to sharp edge ribs.

2.3 Rotational Effects on Internal Passage Flow and Heat Transfer

The flowing fluid inside of rotating turbine blade cooling channels is subjected to an inertial force, rotation induced centrifugal force, and the Coriolis force. The inertial force is coincident with the mainstream flow direction, while the centrifugal force continuously acts in the radially outward sense. The Coriolis force acts perpendicular to the mainstream flow direction. Figure 5 shows that with a radially outward flow stream (first pass), the Coriolis force pushes the core fluid mass towards the trailing wall. As the cross-stream translation of the fluid mass occurs, the fluid will collide

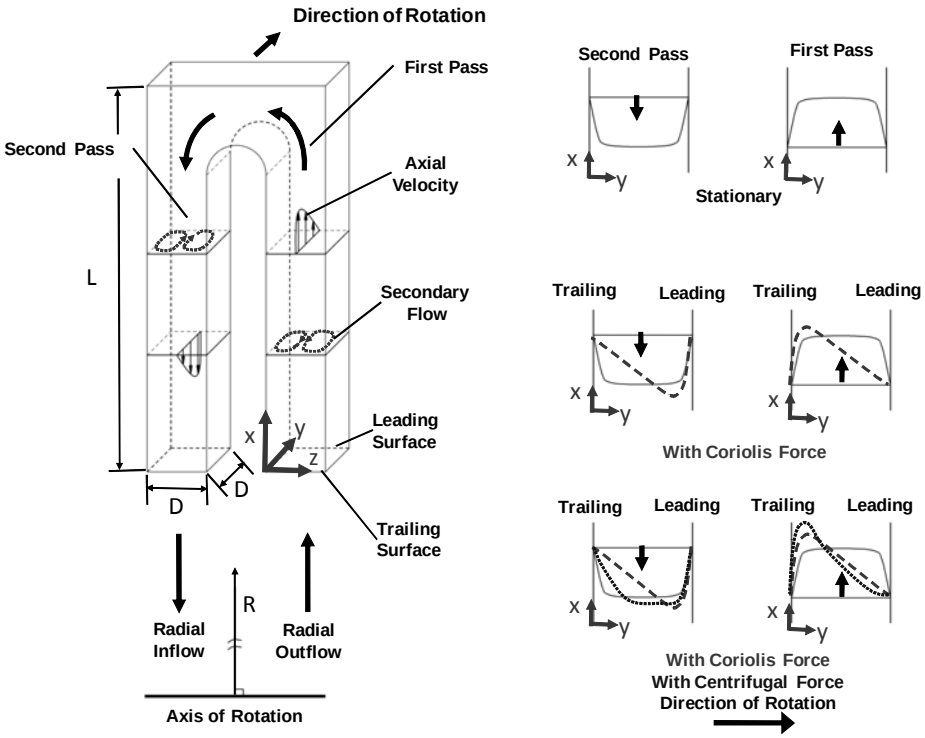

Fig. 5. Coriolis and centrifugal force effects on rotating channel flow field.

with the trailing wall. Due to the continuous replenishment of new fluid, the cross-stream flow will split, reverse its direction, and travel along the side walls of the channel until it once again is turned 180^o back towards the trialing wall. This continuous cross-stream fluid motion results in a pair of cross-stream vortices that, on average, cause the mass of coolant near the trailing wall to be greater than that near the leading wall. Due to mass continuity, the local axial velocity near the trailing wall is increased. Conversely, the local axial velocity near the leading wall decreases. Furthermore, the hot walls of the blade create a temperature gradient throughout the coolant, resulting in a variation of fluid density. The fluid mass near the trailing wall is of lower temperature since the coolant bulk flow velocity is skewed as previously mentioned. The density of the coolant will tend to be greater near the trailing wall. The centrifugal force acts strongly near the trailing wall since the fluid is heavier and accelerates the heavier fluid towards the tip of the channel. The result is a further increase in the local axial velocity near the trailing wall and flow stabilization near the leading wall.

The ramification of the rotational induced Coriolis and centrifugal force with regards to heat transfer then becomes clear by considering the effects on the flow field. Compared to a stationary reference frame, rotation will increase heat transfer on the trailing wall and reduce heat transfer on the leading wall (flow stabilization). If the rotational effects are strong enough, the flow near the leading wall will eventually stagnate (i.e., zero local velocity). At this point, heat transfer on the leading wall can be severally reduced, resulting in very low heat transfer coefficients. However, there is a reverse in the heat transfer trend on the leading wall that occurs due to increased buoyancy effects. Since the flow near the leading wall stagnates, the temperature of the near wall fluid will sharply increase and as such the density of this fluid will be low. Considering the rotational induced centrifugal force, it becomes clear that the buoyancy force acting in the radially inward sense is present. If the rotational effects are strong enough, the near wall flow at the leading wall will actually reverse direction. This flow reversal leads to the increase of heat transfer on the leading wall and the creation of reverse flow cells.

Typical gas turbine internal cooling channels are serpentine in design in order to maximize the cooling potential of the fluid. Thus, a sharp 180^o turn is required to change the flow direction from radially outward towards radially inward. The Coriolis force changes direction when the flow is radially inward and the mainstream velocity is skewed towards the leading wall. The same cross-stream vortices are formed in the radially inward channel, however, these vortices impinge on the leading wall. This tends to increase heat transfer on the leading wall (relative to the stationary frame) and decrease heat transfer on the trailing wall. However, notice that the centrifugal force and the inertial force of the fluid are counteracting in the second pass. Thus, whereas the centrifugal force caused the velocity of the fluid to increase even further (above the Coriolis force effects) on the trailing surface with radially outward flow, now the centrifugal force retards the local axial velocity near the leading wall. Over-

all then, the velocity profile with radially inward flow is not as strongly skewed towards the leading wall. This results in less of a difference between the trailing and leading wall heat transfer coefficients with radially inward flow.

It is worthwhile then to develop nondimensional parameters that may be used to correlate rotating effects to heat transfer. The rotation number (Ro) has been widely accepted to establish the strength of rotation by considering the relative strength of the Coriolis force compared to the bulk inertial force. As such, the rotation number is defined as $\mathrm{Ro} = \Omega D_h/V$. The buoyancy parameter (Bo) is useful to include the effects of density variation (centrifugal effects) and is defined as the ratio of the Grashof number to the square of the Reynolds number; both of which are based on the channel hydraulic diameter. Thus $\mathrm{Bo} = (\Delta\rho/\rho)(\mathrm{Ro}^2)(R/D_h)$.

Typical rotation numbers for aircraft engines are near 0.25 with Reynolds numbers in the range of up to 50,000. One method to achieve conditions similar to a real gas turbine engine in the laboratory is to use air at high pressures. As the pressure of the air increases so will the density. For a fixed Reynolds number, dynamic viscosity, and hydraulic diameter, an increase in density will proportionately decrease the bulk velocity. A lower bulk velocity will in turn increase the rotation number since the rotation number is the ratio of the Coriolis force to bulk inertial force. Increasing the range of the rotation number and buoyancy parameter is very important since gas turbine engineers can utilize these parameters in their analysis of heat transfer under rotating conditions.

Liou et al. [24] investigated the heat transfer in a rectangular channel (AR = 1:2) with 45^o angled ribs under high rotation numbers of up to 2.0 with a corresponding Reynolds number of 5000. Zhou et al. [25] and Zhou and Acharya [26] studied a 4:1 aspect ratio channel with a rotation number of 0.6 at a Reynolds number of 10,000. Chang et al. [27] experimentally studied a square duct with ribs at a rotation number of 1.8 with a corresponding Reynolds number of 7500. Huh et al. [28] increased the range of the rotation number by a factor of 4 for the AR = 2:1 channel. Liu et al. [29] and Huh et al. [30] studied heat transfer in a 1:4 aspect ratio channel. They conducted experiments with air at a pressure of approximately 620 kPa absolute. In their studies, a rotation number of 0.65 was achieved at Reynolds numbers of 10,000. Figure 6 shows that heat transfer on the trailing surface with radially outward flow does indeed increase under rotating conditions due to the flow phenomena previously described. Both the smooth and ribbed channel experience degradation in heat transfer on the leading surface. Rotation reduces the heat transfer in the ribbed channel by a very significant 50%. However, due to buoyancy effects, the leading surface heat transfer trends reverse after a critical rotation number is reached. Physically this implies that the Coriolis force and centrifugal force have skewed the bulk flow so severally towards the trailing surface that reverse flow is occurring on the leading wall. With radially inward flow, the heat transfer in the smooth channel shows the expected behavior on the leading wall. Surprisingly however, due to the aspect ratio of the channel, the heat transfer on the trailing wall also increases. In square channels

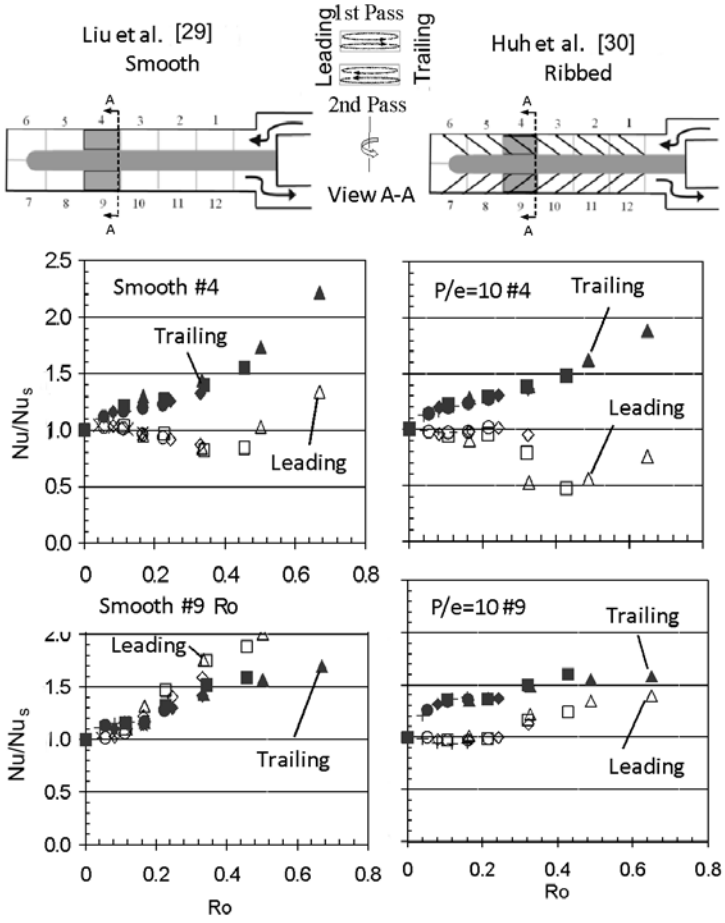

Fig. 6. Rotation number effects on heat transfer in smooth and ribbed 1:4 AR channels.

this is not the case. In ribbed channels the effects of rotation are reduced to the angled rib secondary flows that interact with Coriolis force-induced cross-stream vortices. Overall, these studies showed that the buoyancy parameter and rotation number are useful in correlating the heat transfer enhancement or degradation due to rotation.

Numerical predictions have helped researchers better understand the complex flow phenomena in the cooling passages. Turbulent characteristics are represented by a range of different length and time scale eddies. The dissipation of turbulent kinetic energy is related to small scale eddies while large eddies are similar to the mean flow characteristic length. One approach to numerically solve the flow field is to resolve large eddies through the use of filtered Navier–Stokes equations. This removes eddies which are smaller than the filter and is called large eddy simulation (LES). Abdel-Wahab and Tafti [31] employed the LES in a ribbed rotating duct and investigated the effect of Coriolis and centrifugal buoyancy forces. For the sub-grid stress model the authors employed the dynamic Smagorinsky model. The predictions from

their work showed good quantitative agreement with experimental data from the literature. The second moment closure model used by Chen et al. [32] has been applied to internal cooling channels with a wide range of turbulator configurations and channel aspect ratios. The model was applied to a single pass rotating channel with a square cross section with either 45° or 60° angled ribs by Jang et al. [33]. Al-Qahtani et al. [34] extended these predictions to include 2:1 two pass channels and 4:1 single pass channels with 45° angled ribs. Su et al. [35] used the same second moment closure model to predict the heat transfer coefficients in rotating 4:1 single pass channels with V-shaped ribs. Similar to the experimental studies [10] that cover a wide range of channel aspect ratios, Su et al. [36] performed a complementary study to numerically predict the heat transfer coefficients in the cooling channels with aspect ratios varying from 1:4 to 4:1.

2.4 The Effect of a Developing Flow Entrance

Some gas turbine blade designs provide a developing flow entrance. It is well accepted that due to the thin boundary layer, heat transfer with developing flow is markedly different from fully developed flows. Wright et al. [37] performed experiments in channels with three different entrance geometries. They concluded that the entrance condition would enhance the heat transfer. They also pointed out that the effect of the entrance weakens as the rotation number increases. The influence of the entrance geometry also is stronger in the smooth channel when compared to the ribbed channel.

The previous studies by Liu et al. [29] and Huh et al. [28] considered channels with a developing flow. Liu et al. [29] considered a re-directed sharp bend entrance and Huh et al. [28] studied a sudden expansion from a circular tube to the rectangular cross section of the channel. Figure 7 shows the heat transfer at the channel entrance.

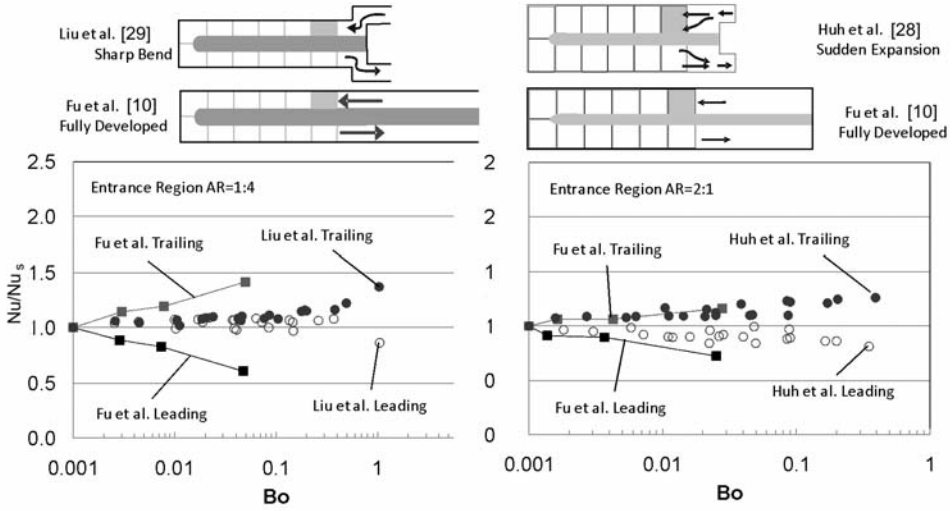

Fig. 7. Local Nusselt number ratios for different entrance conditions.

In these studies the Nusselt number under rotating conditions (Nu) is normalized by the Nusselt number under stationary conditions (Nu_s). Thus, the enhancement/degradation due to rotation (Nu/Nu_s) is extracted. Comparisons are drawn with the work [10] that considered a fully developed flow at the entrance. Notable is the lack of degradation in heat transfer, until large Bo values, on the leading surface for the developing flow cases. Heat transfer is clearly dominated by the entrance.

Also surprising is the different effect of rotation on the trailing surfaces between the two aspect ratios considered. The AR = 2:1 channel shows little difference from the fully developed channel. While the increase (due to rotation) is noticeably different for the AR = 1:4 channel for the different entrance designs (sharp bend and fully developed). Notice also that the buoyancy parameter range is different for the two different aspect ratio channels. This is due to a smaller hydraulic diameter in the AR = 2:1 case. Looking closely however, reveals that for a buoyancy parameter of approximately 0.85 (maximum for the 2:1 case) both AR = 1:4 and AR = 2:1 channels with developing flow, actually have a similar heat transfer enhancement level on the trailing surface due to rotation.

2.5 Effects of Sharp 180^o Turn

The internal cooling passages of the gas turbine blade are connected by 180^o turns. This allows the cooling medium to make multiple passes through the blade so that maximum cooling potential is realized. Flow in the turn region has been studied. Nakayama et al. [38] considered the clearance gap in the turn region and performed experiments using a laser-Doppler velocimetr. The results showed that the downstream separation bubble grew as the clearance decreased. Son et al. [39] used PIV to study the flow field in the sharp turn region. The results showed that the recirculation zone, just downstream of the turn, can occupy a space equal to 30% of the channel hydraulic diameter with maximum reverse flow velocities equal to roughly 50% of the bulk mean speed. Interesting was also the observation that in the midplane of the channel, the flow did not reattach to the separator wall, but the flow was bifurcating instead. Liou et al. [40, 41] also investigated the flow inside the sharp bend region. Their results showed that as the rotation number was increased the characteristic Dean vortices are dominated by rotation and actually form a single vortex that impinges on the leading wall. The separation bubble immediately downstream of the turn likewise decreases in size with increasing rotation number. Iacovides et al. [42] experimentally studied flow and heat transfer in a rectangular channel connected by a U-bend. Lucci et al. [43] numerically studied the three-dimensional turbulent flow and heat transfer in a square U-bend duct. Luo and Razinsky [44] performed a numerical study of the turbulent flows through a number of 2D and 3D 180^o U-ducts, with and without guide vanes, using the Reynolds-averaged Navier–Stokes method.

Liu et al. [29] and Huh et al. [28] considered heat transfer in rectangular channels connected by a sharp 180^o turn with smooth walls. Figure 8 shows the different behavior in heat transfer in the turn portion for the two different aspect ratio ducts. Re-

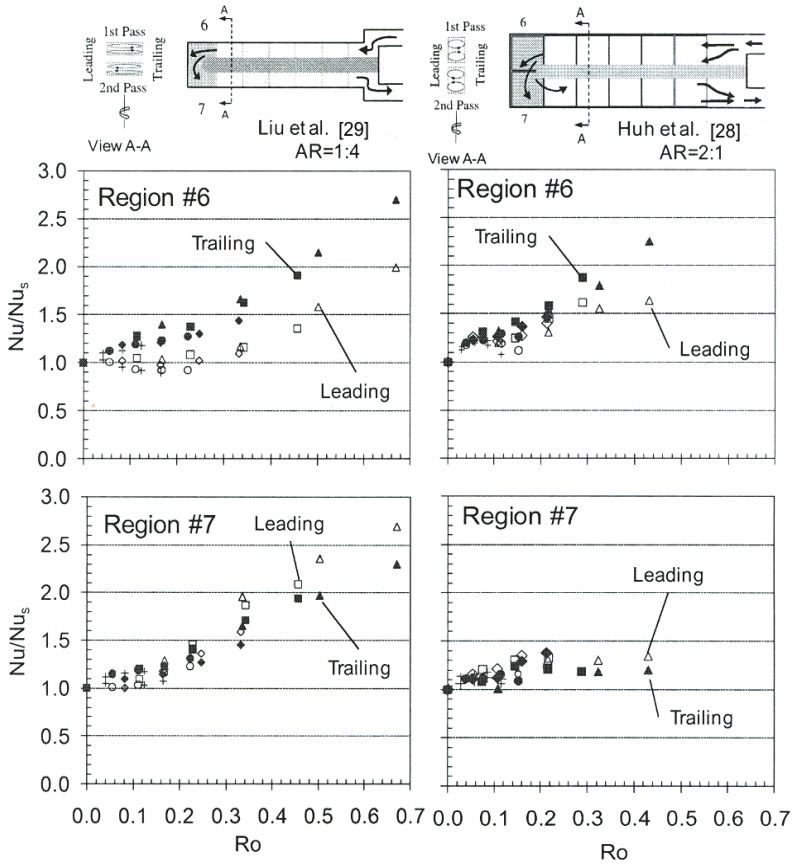

Fig. 8. Heat transfer in the sharp turn of the 1:4 and 2:1 channels.

gion 6 is in the first half of the turn. The heat transfer on the trailing surface for both channels increases more rapidly than the leading because the flow in the first pass is radially outward. The maximum rotation number (Ro = 0.45) for the AR = 2:1 channel is less due to a smaller hydraulic diameter. However, recognize that at this rotation number, the heat transfer enhancement (due to rotation) on both the leading and trailing surfaces is greater for the 2:1 channel compared to the 1:4 one. Most interesting is the stark difference in heat transfer behavior in the second half of the turn (region 7) of the two channels. Clearly, the heat transfer in the 1:4 channel increases on both the leading and the trailing surfaces. However, the leading heat transfer enhancement is greater since the Coriolis force changes direction because the flow is radially inward. The 2:1 channel shows only a modest increase of heat transfer and the effect of rotation levels off even at the higher end values of the rotation number range. The effect of the sharp 180o turn is quite different for these two channels.

2.6 Internal Tip Cooling

A gas turbine blade experiences high heat loads on the tip portion due to high velocity fluid leakage between the rotating blade and casing. Until recently, most of the

studies that have considered heat transfer in multi-pass internal serpentine channels provided minimal information on heat transfer on the inside of the blade tip. Even fewer studies are available that consider the effect of rotation on blade tip cap heat transfer. Jenkins et al. [45] performed experiments using a novel heat flux sensor and the liquid crystal technique. Tests were performed on the tip cap of a 4:1 aspect ratio channel. Bunker [46] used the liquid crystal technique to study the heat transfer on the tip cap of a 2:1 aspect ratio channel. Five tip-cap surfaces were tested including a smooth surface, two different heights of aluminum pin arrays, one more closely spaced pin array, and one pin array made of insulating material [46]. The Reynolds number in the experiments ranged from 200 K to 450 K. The results indicated that by using enhancement techniques, the heat transfer on internal surface of the blade tip cap could be increased by 150%. However, this included the additional area increase as a result of the roughness methods. It was also shown in [46] that by nullifying the area increase a very acceptable increase of 20–30% in the heat transfer coefficient could be obtained. The pressure penalty was negligible. Xie et al. [47] numerically predicted the heat transfer on the tip cap portion of a two-pass rectangular channel with an aspect ratio of 1:2. The study considered pin-fin arrays on the tip

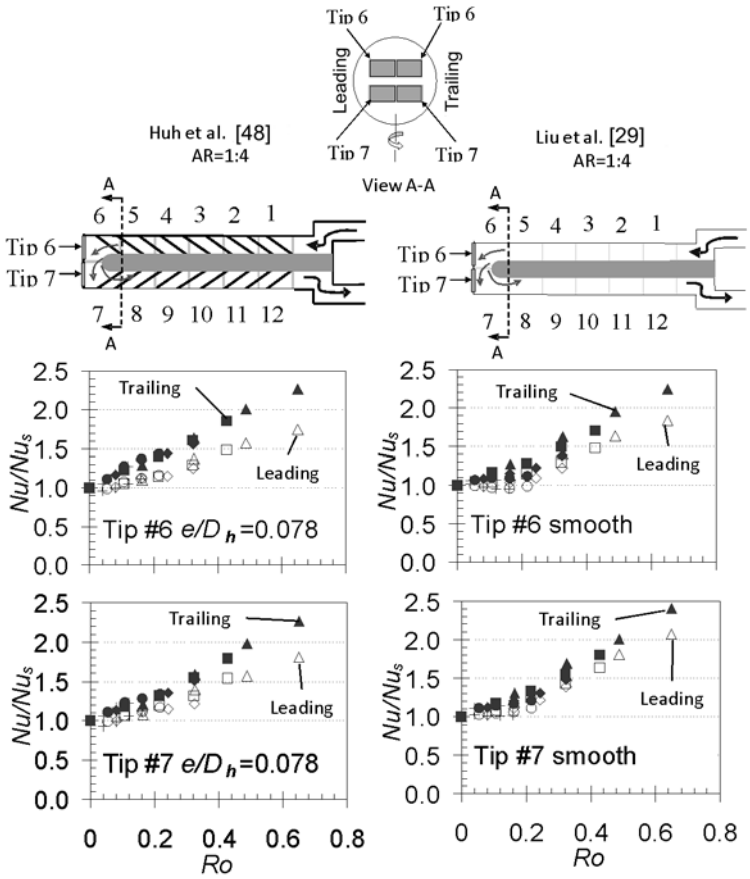

Fig. 9. Effect of rotation on tip cap heat transfer in the AR = 1:4 channel.

portion. The results suggest that heat transfer coefficients obtained with a pin-fin array increased by 84% compared to the smooth tip cap. However, a 35% increase in pressure drop was accompanied in the augmented tip cap design.

The effects of rotation on tip cap internal heat transfer in rectangular channels with AR = 2:1 was presented in [28]. Huh et al. [48] and Liu et al. [29] provide heat transfer results on the tip cap of the 1:4 aspect ratio channel. In that study, the adjacent leading and trailing surfaces of the main passages were lined with ribs. Figure 9 reveals that rotation helps to increase cooling of the blade tip internal surface. Rotation more than doubles the heat transfer coefficients on the tip cap surface near the trailing side in both passages (tip 6 and tip 7). On the portion of the tip located in the second pass (tip 7), the effect of rotation is similar. However, this is not to be confused with less heat transfer, but rather the rotation effects are similar. The reason is because flow is highly turbulent in the turn portion as the mainstream makes the transition from a radially outward to a radially inward direction. The effect of rotation on the heat transfer near the leading side is consistently less than that of the trailing side.

3. COOLING THE TURBINE BLADE LEADING EDGE

The mainstream flow of hot gases exits the combustor and is directed through the nozzle guide vanes and then impinges on the leading edge of the first stage rotor blades. The temperature of these gases may exceed 1500^{o}C, which is clearly well in excess of allowable metal temperatures. These high heat loads require clever cooling schemes to be used at the leading edge of the blade. A commonly employed internal cooling technique is to use jet impingement on the internal surface of the cooling passage at the blade leading edge. Air from the compressor of the gas turbine system is bled off and passed through the internal cooling channels of the gas turbine blade. The internal channel at the blade leading edge utilizes this cooling air for impingement on the blade leading edge inner surface. Selectively placed jet-holes (or nozzles) are located on the leading edge pass inner wall that divides the leading edge channel from other serpentine passages. Flow from the neighboring internal passage is forced through these jet-holes so that impingement occurs on the leading edge inner surface of the blade. The design application of this type of cooling scheme must consider several different factors; namely, the shape of the jet nozzle, the layout of the jet holes, the shape of confinement chambers, the shape of the target surface, the jet-to-target spacing, and cross-flow effects are just a few.

3.1 Enhancement of Impingement Target Surfaces

As a result of advancements made in research of heat transfer enhancement techniques, (i.e., rib turbulators, pin-fins, dimples) designs of leading edge internal cooling passages are now also incorporating these turbulence enhancement methods. Recent studies have considered the combined effects of target surface roughening coupled with jet impingement. Annerfeldt et al. [49] performed experiments on a flat target

plate roughened with triangular, wing, and dashed ribs. Taslim et al. [50] investigated heat transfer on a curved target surface to more realistically simulate the leading edge of the blade. Three different roughening techniques were studied: conical bumps, tapered radial ribs, and sand paper type roughness. Later the study was extended to include horseshoe ribs and notched-horseshoe ribs [51].

Son et al. [52] considered a pin-fin heat transfer enhancement technique for the target surface. These studies concluded that there is a benefit to be gained by roughening the target surface. It was shown that heat transfer enhancement was driven by the additional area increase of the roughening technique. Other studies considered enhancing the target plate heat transfer with dimples. Kanokjaruvijit and Martinez-Botas [53, 54] showed that by impinging on the dimple, higher energetic vortices were generated and thus heat transfer was increased.

3.2 Film Cooling Hole Effects on Impingement

Since the leading edge of the gas turbine blade incorporates a showerhead film cooling design, studies have also included film-cooling holes on the target plate. When an initial cross flow is present, the jet impingement on an effusion target plate has been shown to provide higher heat transfer than impingement on a solid plate alone. Rhee et al. [55] explain that the cross flow effect is reduced due to the film cooling holes. Studies by Cho et al. [56] and Taslim and Khanicheh [57] also have shown that the heat transfer can be significantly increased by including the film cooling holes on the target plate.

3.3 Mach Number Effects on Impingement

Most studies involving impingement heat transfer have varied the jet Reynolds number with the Mach number. Brevet et al. [58] considered the effects of changing Mach number at a constant Reynolds number for a single jet. The highest Mach number in the study was 0.69. From their results, they concluded that at low Mach numbers (<0.2) the influence on heat transfer, by the Mach number, could be neglected. However, at higher Mach numbers, compressibility effects must be considered and it was shown that heat transfer could be increased on the target surface. More recently, Park et al. [59] considered the separate effects of Mach number and Reynolds number of a jet array. They showed that for higher Reynolds numbers at high Mach numbers, previous correlations were inadequate. A new correlation was proposed for the extended range of Reynolds and Mach numbers.

3.4 Jet Geometry

Other studies have considered different jet-hole designs [60] and variable size jet-holes and spacing of the impingement jet array [61, 62].

3.5 Rotating Effects on Jets

All of the studies previously mentioned considered jet impingement heat transfer under stationary conditions. Of course, however, the turbine blade is rotating. A hand-

ful of studies [63–66] are available on rotating effects on jet impingement heat transfer. Overall, the effectiveness of the jet is reduced under rotating conditions due to deflection from the target surface.

3.6 Ribbed Internal Leading Edge Channels

Ahn and Son [67] studied the heat transfer and pressure drop in a roughened equilateral triangular channel used to model the internal cooling passage at the blade leading edge. Their studies considered heat transfer enhancement with ribs at different rib-pitch/rib-height ratios of P/e = 4, 8, and 16. They concluded that the P/e = 8 has the best thermal performance with the Reynolds numbers ranging from 10,000 to 70,000. Haasenritter and Weigand [68] performed a computational study of the heat transfer in a rib-roughened triangular channel. Lee et al. [69] measured the heat transfer and pressure drop in a rotating equilateral triangular channel with three different rib arrangements: 45^o, 90^o, and 135^o. They showed that the thermal performance for 45^o and 135^o angled ribs are very similar and both were higher than the 90^o ribs.

Recently, two studies by Liu et al. [70, 72] modeled the leading edge cavity as an equilateral triangle. The studies collectively considered three different rib configurations. A high rotation number of 0.58 was achieved by using a pressurized system. Figure 10 shows the channel average heat transfer enhancement/degradation due to rotation by considering the ratio of the Nusselt number from rotating experiments to that of stationary experiments (Nu/Nu_s). The Reynolds number range is from 10,000 to 40,000 and the rotational speed was varied from 0 to 400 rpm. In smooth channels the effect of rotation is more pronounced since the added benefits of ribs (secondary flows) are not present. Rotation nearly doubles the heat transfer on the trailing surface in the smooth channel due to impingement of Coriolis force induced secondary flows. The flow near the leading surface begins to stabilize with rotation resulting in slightly reduced heat transfer. The added benefit of ribs is to create secondary flows and increase near-wall turbulent mixing. Both the leading and the trailing surface heat

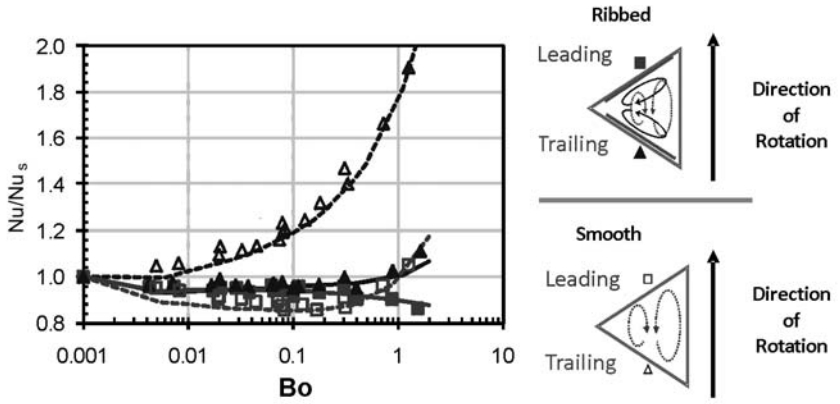

Fig. 10. Buoyancy parameter effects in the equilateral triangle channel of Liu et al. [70].

transfer is considerably increased in the stationary reference frame. Thus, Nu_s will be high. This is the reason why such a small effect of rotation is observed in the ribbed triangular channel. Only when the buoyancy parameter reaches large values is there a change in heat transfer.

4. TRAILING EDGE HEAT TRANSFER

Effective cooling of the trailing edge is required to prevent burnout. The internal cooling passage has been represented with wide aspect rectangular channels [73, 74]. However, the cross-sectional shape is best represented with a wedge or trapezoid. To enhance heat transfer in this region of the blade, the leading and trailing surfaces are roughened with ribs or pin-fins. Further protection is provided with coolant ejection from the narrow portion of the channel. Hwang and Lu [75] studied the effects of lateral-flow ejection, pin shapes, and flow Reynolds number in a trapezoidal duct. Carcasci et al. [76] also investigated heat transfer and pressure drop inside wedge-shaped cooling channels with pedestals (long ribs) and pin-fins. Cunha and Chyu [77] used a liquid crystal technique to obtain heat transfer data inside the wedge-shaped channel with and without discharge through slots or holes. Wright and Gohardani [78] used a traditional copper plate method to investigate the heat transfer in a rectangular (AR = 3:1) and trapezoidal channel. The study considered fully developed and developing flow conditions. The experiments were conducted with and without coolant ejection. Other studies [79, 80] have also considered different aspects of heat transfer and fluid in the trapezoidal/wedge shaped channel.

4.1 Rotating Effects on Trailing Edge Cooling Channels

The aforementioned studies on trapezoidal and wedge shaped cooling passages were all conducted under stationary conditions. However, the additional effects of Coriolis induced secondary flows and centrifugal driven buoyancy alter the heat transfer characteristics. Chang et al. [81] studied heat transfer in rib roughened trapezoidal duct with bleed holes. Wright el al. [82] considered heat transfer in a trailing edge cooling passage with smooth walls. The channel was placed at an angle of 135^o relative to the direction of rotation. Wright et al. [82] showed that the data in a smooth wedge-shaped channel can be correlated as a function of buoyancy parameter. Liu et al. [71] extended the study to include slot ejection. The rotation number in their study was 1.0 based on inlet velocity. Due to ejection from the channel, heat transfer analysis utilized a local rotation number, Reynolds number, and buoyancy parameter. Figure 11 presents their streamwise and spanwise averaged Nusselt number ratios. The data is correlated with the buoyancy parameter by a power law function. Over the range of Reynolds numbers and rotational speeds tested, it is seen that each of the three surfaces follows very distinct trends. The data for each surface collapse on to common curve. Most notably, for all three surfaces, the Nusselt number ratios increase as the rotation number increases. The heat transfer enhancement with slot ejec-

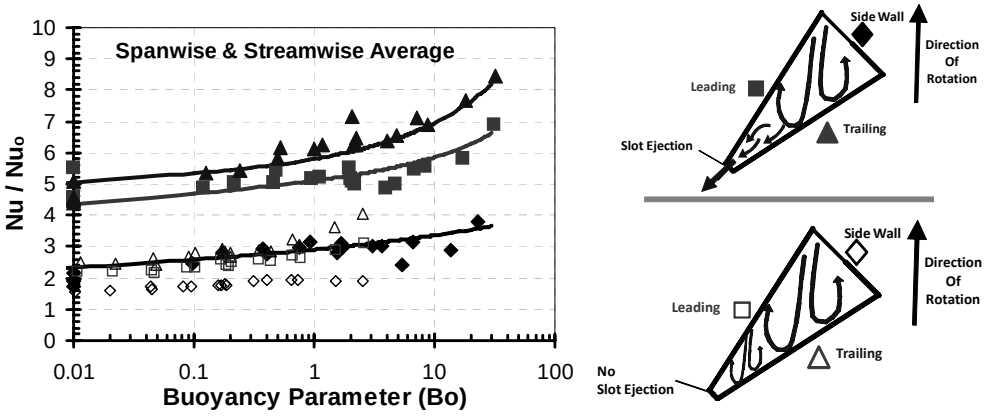

Fig. 11. Rotation number and buoyancy parameter effects on heat transfer in the trapezoidal channel with and without ejection.

tion is much higher than the cases without slot ejection. Even with the effect of slot ejection in the wedge-shaped channel, it is observed that the data can be correlated with the buoyancy parameter from the combination of variable Reynolds numbers and rotational speeds.

5. CONCLUDING REMARKS

Over the past decade, research on gas turbine blade heat transfer has progressed considerably. Many aspects of internal cooling have been considered. Advanced jet impingement studies have coupled the benefits of high heat transfer resulting for impinging jets with surface enhancement techniques.

The additional complications associated with showerhead film cooling ejection have also been taken into account. However, the full realization of the effects of rotation on leading edge jet impingement needs progression as is evidenced by limited literature. Heat transfer studies on the internal serpentine cooling passages found in the mid-portions of the blade have evolved from experiments at low rotation numbers to sophisticated experimental methods that provide more realistic engine conditions. Yet still, progression is needed to provide more information on even higher buoyancy parameter ranges at higher Reynolds numbers. This information will be of great interest to the land based gas turbine designer. Other points of focus involve heat transfer inside cooling channels with bleed hole effects, tip internal surface enhancement methods along with ejection, all under rotating conditions. With advancements being made on alternative fuel sources for turbines (i.e., hydrogen), a step change in the capability of blades to handle higher heating loads is a must. Compound and new cooling concepts need to be developed and explored, such as heat pipe and micro-channel applications for blade tip, leading, and trailing edge cooling. Fundamental studies need to consider the effects of rotation on these new cooling concepts. Development of

this technology will ensure that the blade design is not the limiting factor for increased efficiency and the move to other fuel sources.

NOMENCLATURE

AR	aspect ratio
Bo	buoyancy parameter
D_h	hydraulic diameter
e	rib height
e/D_h	blockage ratio (rib-height to channel hydraulic diameter ratio)
e^+	roughness Reynolds number
f_0	Blasius correlation friction factor
G	heat transfer roughness function
H	channel height
Nu	Nusselt number
Nu_0	Dittus/Boelter correlation Nusselt number
P	rib pitch
P/e	rib-pitch to rib-height ratio
R	friction roughness function
Ro	rotation number
TP	thermal performance
V	velocity
W	channel width

Greek symbols

α	rib angle
$\Delta\rho$	density difference based on inlet temperature and wall temperature
Ω	angular velocity
ρ	density.

REFERENCES

1. Han, J. C., Dutta, S., and Ekkad, S. V. *Gas Turbine Heat Transfer and Cooling Technology*, Taylor and Francis, New York, 2000.
2. Han, J. C. and Wright, L. M. Enhanced internal cooling of turbine blades and vanes. In: *The Gas Turbine Handbook*, U.S. Department of Energy, Office of Fossil Energy, National Energy Technology Laboratory (NETL), 2006, pp. 321–354.
3. Fu, W. F., Wright, L. M., and Han, J. C. Heat transfer in two-pass rotating rectangular channels (AR = 1:2 and AR = 1:4) with 45^o angled rib turbulators, ASME Paper No. GT2004-53261, 2004.
4.

Agarwal, P., Acharya, S., and Nikitopoulos, D. E. Heat/mass transfer in 1:4 rectangular passages with rotation, ASME Paper No. 2003-GT-38615, 2003.

5. Liu, Y. H., Wright, L. M., Fu, W. L., and Han, J. C. Rib spacing effect on heat transfer in rotating two-pass ribbed channel (AR = 1:2), *J. Thermophys. Heat Transfer*, 2007, Vol. 21, No. 3, pp. 582–595.
6. Cho, H. H., Kim, Y. Y., Kim, K. M., and Rhee, D. H. Effects of rib arrangements and rotation speed on heat transfer in a two-pass duct, ASME Paper No. 2003-GT-38609, 2003.
7. Al-Hadhrami, L. and Han, J. C. Effect of rotation on heat transfer in two-pass square channels with five different orientations of 45^{o} angled rib turbulators, *Int. J. Heat Mass Transfer*, 2003, Vol. 46, pp. 653–669.
8. Azad, G. S., Uddin, M. J., Han, J. C., Moon, H. K., and Glezer, B. Heat transfer in a two-pass rectangular rotating channel with 45-deg angled rib turbulators, *J. Turbomachinery*, 2002, Vol. 124, pp. 251–259.
9. Wright, L. M., Fu, W. L., and Han, J. C. Thermal performance of angled, V-shaped, and W-shaped rib turbulators in rotating rectangular cooling channels (AR = 4:1), ASME Paper No. GT2004-54073, 2004.
10. Fu, L. W., Wright, L. M., and Han, J. C. Buoyancy effects on heat transfer in five different aspect-ratio rectangular channels with smooth walls and 45 degree ribbed walls, *J. Heat Transfer*, 2006, Vol. 128, No. 11, pp. 1130–1141.
11. Bailey, J. C. and Bunker, R. S. Heat transfer and friction in channels with very high blockage 45-deg staggered turbulators, ASME Paper No. GT2003-38611, 2003.
12. Casarsa, L., Cakan, M., and Arts, T. Characterization of the velocity and heat transfer fields in an internal cooling channel with high blockage ratio, ASME Paper No. GT2002-30207, 2002.
13. Kiml, R., Mochizuki, S., and Murata, A. Effects of rib arrangements on heat transfer and flow behavior in a rectangular rib-roughened passage: application to cooling of gas turbine blade trailing edge, *J. Heat Transfer*, 2001, Vol. 123, pp. 675–681.
14. Gao, X. and Suden, B. Heat transfer and pressure drop measurements in rib-roughened rectangular ducts, *Exp. Thermal Fluid Sci.*, 2001, Vol. 24, pp. 25–34.
15. Rhee, D. H., Lee, D. H., Cho, H. H., and Moon, H. K. Effects of duct aspect ratios on heat/mass transfer with discrete V-shaped ribs, ASME Paper No. GT2003-38622, 2003.
16. Cho, H. H., Wu, S. J., and Kwon, H. J. Local heat/mass transfer measurements in a rectangular duct with discrete ribs, *J. Turbomachinery*, 2000, Vol. 122, pp. 579–586.
17. Bunker, R. S. and Osgood, S. J. The effect of turbulator lean on heat transfer and friction in a square channel, ASME Paper No. GT2003-38137, 2003.

18. Thurman, D. and Poinsette, P. Experimental heat transfer and bulk air temperature measurements for a multipass internal cooling model with ribs and bleed, ASME Paper No. 2000-GT-233, 2000.
19. Rallabandi, A. P., Yang, H., and Han, J. C. Heat transfer and pressure drop correlations for square channels with 45 deg ribs at high Reynolds numbers, *J. Heat Transfer*, 2009, Vol. 131, pp. 071703-1-10.
20. Rallabandi, A. P., Nawaf, A., and Han, J. C. Heat transfer and pressure drop measurements for a square channel with 45 deg round edged ribs at high Reynolds numbers, ASME Paper No. GT2009-59546, 2009.
21. Han, J. C. Heat transfer and friction characteristics in rectangular channel with rib turbulators, *J. Heat Transfer*, 1988, Vol. 110, pp. 321–328.
22. Han, J. C. and Park, J. S. Developing heat transfer in rectangular channels with rib turbulators, *Int. J. Heat Mass Transfer*, 1998, Vol. 31, No. 1, pp. 183–195.
23. Han, J. C. and Park, J. S. Measurements of Heat Transfer and Pressure Drop in Rectangular Channels with Turbulence Promoters, NASA Report No. 4015, 1986.
24. Liou, T. M., Chang, S. W., Hung, J. H., and Chiou, S. F. High rotation number heat transfer of 45^{o} rib-roughened rectangular duct with two channel orientations, *Int. J. Heat Mass Transfer*, 2007, Vol. 50, pp. 4063–4078.
25. Zhou, F., Lagrone, J., and Acharya, S. Internal cooling in 4:1 AR passages at high rotation numbers, ASME Paper No. GT 2004-53501, 2004.
26. Zhou, F. and Acharya, S. Heat transfer at high rotation numbers in a two-pass 4:1 aspect ratio rectangular channel with 45 deg skewed ribs, *J. Turbomachinery*, 2008, Vol. 130, No. 2, pp. 021019-1–12.
27. Chang, S. W., Liou, T. M., Hung, J. H., and Yeh, W. H. Heat transfer in a radially rotating square-sectioned duct with two opposite walls roughened by 45 deg staggered ribs at high rotation numbers, *J. Heat Transfer*, 2007, Vol. 129, No. 2, pp. 188–199.
28. Huh, M., Lei, J., Liu, Y. H., and Han, J. C. High rotation number effects on heat transfer in a rectangular (AR = 2:1) two pass channel, ASME Paper No. GT2009-59421, 2009.
29. Liu, Y. H., Huh, M., Han, J. C., and Chopra, S. Heat transfer in a two-pass rectangular channel (AR = 1:4) under high rotation numbers, *J. Heat Transfer*, 2008, Vol. 130, No. 8, pp. 081701-1–9.
30. Huh, M., Liu, Y. H., Han, J. C., and Chopra, S. Rib-spacing effect on heat transfer in rectangular channels at high rotation numbers, *J. Thermophys. Heat Transfer*, 2009, Vol. 23, No. 2, pp. 294–304.
31. Abdel-Wahab, S. and Tafti, K. D. Large eddy simulation of flow and heat transfer in a 90 deg ribbed duct with rotation: effect of Coriolis and centrifugal buoyancy forces, *J. Turbomachinery*, 2004, Vol. 126, pp. 627–636.
32. Chen, H. C., Jang, Y. J., and Han, J. C. Computation of flow and heat transfer in rotating two-pass square channels by a Reynolds stress model, *Int. J. Heat Mass Transfer*, 2000, Vol. 43, No. 9, pp. 1603–1616.

33. Jang, Y. J., Chen, H. C., and Han, J. C. Flow and heat transfer in a rotating square channel with 45-degree angled ribs by Reynolds stress turbulence model, *J. Turbomachinery*, 2001, Vol. 123, No. 1, pp. 124–132.
34. Al-Qahtani, M., Jang, Y. J., Chen, H. C., and Han, J. C. Prediction of flow and heat transfer in rotating two-pass rectangular channels with 45-degree rib turbulators, *J. Turbomachinery*, 2002, Vol. 124, pp. 242–250.
35. Su, G., Tang, S., Chen, H. C., and Han, J. C. Flow and heat transfer computations in rotating rectangular channels with V-shaped ribs, *J. Thermophys. Heat Transfer*, 2004, Vol. 18, No. 4, pp. 534–547.
36. Su, G., Chen, H. C., Han, J. C., and Heidmann, D. Computation of flow and heat transfer in two-pass rotating rectangular channels (AR = 1:1, AR = 1:2, AR = 1:4) with 45-deg angled ribs by a Reynolds stress turbulence model, *ASME Paper*, No. GT2004-53662, 2004.
37. Wright, L. M., Fu, W. L., and Han, J. C. Influence of entrance geometry on heat transfer in rotating rectangular cooling channels (AR = 4:1) with angled ribs, *J. Heat Transfer*, 2005, Vol. 127, pp. 378–387
38. Nakayama, H., Hirota, M., Fujita, H., Yamada, T., and Koide, Y. Fluid flow and heat transfer in two-phase smooth rectangular channels with different turn clearances, *J. Turbomachinery*, 2006, Vol. 128, No. 4, pp. 772–785.
39. Son, S. Y., Kihm, K. D., and Han, J. C. PIV flow measurements for heat transfer characterization in two-pass square channels with smooth and 90-degree ribbed wall, *Int. J. Heat Mass Transfer*, 2002, Vol. 45, No. 24, pp. 4809–4822.
40. Liou, T. M., Chen, M. Y., and Tsai, M. H. Fluid flow and heat transfer in a rotating two-pass square duct with in-line 90-deg ribs, *J. Turbomachinery*, 2002, Vol. 124, No. 2, pp. 260–268.
41. Liou, T. M., Chen, C. C., and Chen, M. Y. Rotating effect on fluid flow in two smooth ducts connected by a 180-degree bend, *J. Fluids Eng*., 2003, Vol. 125, No. 1, pp. 138–148.
42. Iacovides, H., Kounadis, D., Launder, B. E., and Xu, Z. Experimental study of the thermal development in a rotating square-ended U-bend, ASME Paper No. GT2006-90846, 2006.
43. Lucci, J. M., Amano, R. S., and Guntur, K. Turbulent flow and heat transfer in variable geometry U-bend blade cooling passage, ASME Paper No. GT2007-27120, 2007.
44. Luo, J. and Razinsky, E. H. Analysis of turbulent flow in 180 deg turning ducts with and without guide vanes, *J. Turbomachinery*, 2009, Vol. 131, No. 2, pp. 021011-1–10.
45. Jenkins, S., Wolfersdorf, J. V., Weigand, B., Roediger, T., Knauss, H., and Kraemer, E. Time-resolved heat transfer measurements on the tip wall of ribbed channel using a novel heat flux sensor. Part II: Heat transfer results, ASME Paper No. GT2006-91131, 2006.

46. Bunker, R. The augmentation of internal blade tip-cap cooling by arrays of shaped pins, *J. Turbomachinery*, 2008, Vol. 130, No. 4, pp. 041007-1–8.
47. Xie, G., Sunden, B., Wang, L., and Utrianen, E. Enhanced internal heat transfer on the tip-wall in a rectangular two-pass channel (AR = 1:2) by pin-fin arrays, *Numer. Heat Transfer*, 2009, Vol. 55, No. 8, pp. 739–761.
48. Huh, M., Liu, Y. H., and Han, J. C. Effect of rib height on heat transfer in a two pass rectangular channel (AR = 1:4) with a sharp entrance at high rotation numbers, *Int. J. Heat Mass Transfer*, 2009 (in press).
49. Annerfeldt, M. O., Persson, J. L., and Torisson, T. Experimental investigation of impingement cooling with turbulators or surface enlarging elements, ASME Paper No. 2001-GT-0149, 2001.
50. Taslim, M. E., Setayeshgar, L., and Spring, S. D. An experimental evaluation of advanced leading edge impingement cooling concepts, *J. Turbomachinery*, 2001, Vol. 123, No. 1, pp. 147–153.
51. Taslim, M. E., Bacteria, K., and Liu, H. Experimental and numerical investigation on a rib-roughened leading-edge wall, *J. Turbomachinery*, 2003, Vol. 125, No. 4, pp. 682–691.
52. Son, C., Dailey, G., Ireland, P., and Gillespie, D. An investigation of the application of roughness elements to enhance heat transfer in an impingement cooling system, ASME Paper No. GT2005-68504, 2005.
53. Kanokkjaruvijit, K. and Martinez-Botas, R. F. Parametric effects on heat transfer of impingement on dimpled surface, *J. Turbomachinery*, 2005, Vol. 127, No. 2, pp. 287–296.
54. Kanokkjaruvijit, K., and Martinez-Botas, R. F. Parametric heat transfer and pressure investigation of dimple impingement, *J. Turbomachinery*, 2008, Vol. 130, No. 1, pp. 011003-1–11.
55. Rhee, D. H., Choi, J. H., and Cho, H. H. Flow and heat (mass) transfer characteristics in an impingement/effusion cooling system with crossflow, ASME Paper No. GT-2002-30474, 2002.
56. Cho, H. H., Rhee, D. H., and Goldstein, R. J. Effects of hole arrangements on local heat/mass transfer for impingement/effusion cooling with small hole spacing, *ASME J. Turbomachinery*, 2008, Vol. 130, No. 1, pp. 041003-1–11.
57. Taslim, M. E. and Khanicheh, A. Experimental and numerical study of impingement on an airfoil leading-edge with and without showerhead and Gill film holes, ASME Paper No. GT2005-68037, 2005.
58. Brevet, P., Dorignac, E., and Vullierme, J. J. Mach number effect on jet impingement heat transfer, *Ann. N.Y. Acad. Sci.*, 2001, Vol. 934, pp. 409–416.
59. Park, J., Goodro, M., Ligrani, P., Fox, M., and Moon, H. K. Separate effects of Mach number and Reynolds number on jet array impingement heat transfer, *J. Turbomahinery*, 2007, Vol. 129, No. 2, pp. 269–280.
60. Taslim, M. E, and Setayeshgar, L. Experimental leading-edge impingement cooling through racetrack crossover holes, ASME Paper No. 2001-GT-0153, 2001.

61. Gao, L., Ekkad, S., and Bunker, R. Impingement heat transfer. Part I: Linearly stretched arrays of holes, *J. Thermophys. Heat Transfer*, 2005, Vol. 19, No. 1, pp. 57–65.
62. Goodro, M., Park, J., Ligrani, P., Fox, M., and Moon, H. K. Effects of hole spacing on spatially-resolved jet array impingement heat transfer, *Int. J. Heat Mass Transfer*, 2008, Vol. 51, Nos. 25–26, pp. 6243–6253.
63. Parsons, J. A. and Han, J. C. Rotation effect on jet impingement heat transfer in smooth rectangular channels with coolant extraction, *Int. J. Rotating Machinery*, 2001, Vol. 7, pp. 87–103.
64. Parsons, J. A., Han, J. C., and Lee, C. P. Rotation effect on jet impingement heat transfer in smooth rectangular channels with four heated walls and film coolant extraction, ASME Paper No. GT-2003-38905, 2003.
65. Hong, S. K., Lee, D. H., and Cho, H. H. Heat/mass transfer in rotating impingement/effusion cooling with rib turbulators, *Int. J. Heat Mass Transfer*, 2009, Vol. 52, Nos. 13–14, pp. 3109–3117.
66. Chiang, H. W. D. and Li, H. L. Jet impingement and forced convection cooling experimental study in rotating turbine blades, ASME Paper No. GT2009-59795, 2009.
67. Ahn, S. W. and Son, K. P. Heat transfer and pressure drop in the roughened equilateral triangular duct, *Int. Comm. Heat Mass Transfer*, 2002, Vol. 29, pp. 479–488.
68. Haasenritter, A. and Weigand, B. Heat transfer in triangular rib-roughened channels, ASME Paper No. NHTC 2001–20245, 2001.
69. Lee, D. H., Rhee, D. H., and Cho, H. H. Heat transfer measurements in a rotating, equilateral triangular channel with various rib arrangements, ASME Paper No. GT 2006-90973, 2006.
70. Liu, Y. H., Huh, M., Rhee, D. H., Han, J. C., and Moon, H. K. Heat transfer in leading edge, triangular shaped cooling channels with angled ribs under high rotation numbers, ASME Paper No. GT 2008-50344, 2008.
71. Liu, Y. H., Huh, M., and Han, J. C. High rotation number effect on heat transfer in a triangular channel with 45^{o}, inverted 45^{o}, and 90^{o} ribs, ASME Paper No. GT 2009-59216, 2009.
72. Liu, Y. H., Huh, M., Wright, L. M., and Han, J. C. Heat transfer in trailing edge channels with slot ejection under high rotation numbers, *J. Thermophys. Heat Transfer*, 2009, Vol. 23, No. 2, pp. 305–315.
73. Griffith, T. S., Al-Hadhrami, L., and Han, J. C. Heat transfer in rotating rectangular cooling channels (AR = 4) with angled ribs, *J. Heat Transfer*, 2002, Vol. 124, pp. 617–625.
74. Wright, L. M., Lee, E., and Han, J. C., Effect of rotation on heat transfer in rectangular channels with pin-fins, *J. Thermophys. Heat Transfer*, 2004, Vol. 18, No. 2, pp. 262–272.

75. Hwang, J. J. and Lu, C. C. Lateral-flow effect on endwall heat transfer and pressure drop in a pin-fin trapezoidal duct with various pin shapes, *J. Turbomachinery*, 2001, Vol. 123, pp. 133–139.
76. Carcasci, C., Facchini, B., and Innocenti, L. Heat transfer and pressure drop evaluation in thin wedge-shaped trailing edge, ASME Paper No. GT2003-38197, 2003.
77. Cunha, F. J. and Chyu, M. K. Trailing-edge cooling for gas turbines, *J. Propul. Power*, 2006, Vol. 22, No. 2, pp. 286–300.
78. Wright, L. M. and Gohardani, A. S. Effect of the coolant ejection in rectangular and trapezoidal trailing-edge cooling passages, *J. Thermophys. Heat Transfer*, 2009, Vol. 23, No. 2, pp. 316–326.
79. Armellini, A., Coletti, F., and Arts, T. Aero-thermal investigation of a rib-roughened trailing edge channel with crossing-jets. Part I: Flow field analysis, ASME Paper, No. GT2008-50694, 2008.
80. Tarchi, L. and Facchini, B. Investigation of innovative trailing edge cooling configurations with enlarged pedestals and square or semicircular ribs. Part 1: Experimental results, ASME Paper No. GT2008-51047, 2008
81. Chang, S. W., Liou, T. M., Chiou, S. F., and Chang S. F. Heat transfer in a high-speed rotating trapezoidal duct with rib-roughened surfaces and air bleeds from the wall on the apical side, J. Heat Transfer, 2008, Vol. 130, No. 6, pp. 061702-1–13.
82. Wright, L. M., Liu, Y. H., Han, J. C., and Chopra, S. Heat transfer in trailing edge, wedge-shaped cooling channels under high rotation numbers, *J. Heat Transfer*, 2008, Vol. 130, No. 7, pp. 071701-1–11.

□◆◆◆□

Heat Transfer Research, 2010, Vol. 41, No. 8

Heat Transfer and Flow Testing in Engine HP Turbine Cooling System Development

PETER IRELAND,[1*] VIKRAM MITTAL,[2] DONGAL JACKSON,[1]

and HOWOONG NAMGOON[1]

[1]Turbines SCU, Rolls-Royce plc, Moor Lane,
PO box 32, Derby, DE24 8BJ, UK

[2]Vehicles and Robotics Group, C.S. Draper Laboratory
555 Technology St, Cambridge, MA 02139 USA
vmittal@draper.com

The speed with which a new aircraft engine is developed prevents extensive experimental testing of key turbine components. For this reason, design engineers rely increasingly on computer simulations to develop and perfect components before committing to final designs. CFD predictions can fail to accurately predict some key features of turbomachinery flows, and design engineers often seek to calibrate their designs and CFD predictions against test data. This paper addresses the use of flow and heat transfer experiments in the context of turbine cooling system development. It reviews how experiments can be used to support both research activity and the engine development program (EDP). The paper describes the state of the art in Perspex model test technology and the introduction of rapid prototyping (RP). This paper reports applications of these models to aerothermal testing of turbine component and reviews the advantages and the shortcomings of such testing. The paper focuses on the stereo-lithography (SL) technique as this remains the most popular method for producing test models for aero-thermal tests. The paper also explains how judicious use of RP test data can be used in cooling system development to arrive at optimal systems.

* * *

*Address all correspondence to Peter Ireland E-mail: peter.ireland@rolls-royce.com

ISSN1064-2285

Keywords: turbine cooling, rapid prototyping, SLA, liquid crystal, heat transfer, turbine heat transfer

1. INTRODUCTION

1.1 Data Context

The requirement for long component life combined with the extremely high gas temperatures used in modern HP turbines requires very detailed predictions of the blade and vane temperatures. In order to design the cooling scheme efficiently, detailed knowledge of the local HTC within the cooling system is necessary. Since the detail of the real engine cooling geometry has an effect on the HTC levels, there is a pressing need to investigate real geometries in order to optimize the cooling schemes. It is often the case that simplification of the geometry makes interpretation of the results to the engine context difficult.

2. PERSPEX MODEL TESTING

Perspex model tests represent the state of the art for heat transfer data accuracy and resolution for blade cooling. The technique was originally developed in the 1980s and has been employed with success by many heat transfer research groups. It is also now used by most of the gas turbine companies. The method relies on subjecting a Perspex model of the cooling passage to a sudden change in gas temperature. The response of the surface temperature is then measured using Thermochromic Liquid Crystal material (TLC) as described in [1].

2.1 Fully Featured Geometry

The technique is very well suited to measuring detailed HTC distributions in complex geometries [2], and one recent development is application to realistic geometries including most of the cooling passage features. Measurement of local coolant temperature variation through the transient experiment allows highly accurate HTC data to be obtained on all internal surfaces of a turbine blade or vane cooling passage [3]. Advanced data analysis and image processing strategies can be employed to allow for local variations in viewing and lighting conditions [4].

There are many reports in the literature that show that the effect of rotation on blade cooling heat transfer coefficients can be significant. The strength of the effect depends on whether secondary flows caused by the Coriolis acceleration and/or buoyancy forces, indicated by high rotation number and buoyancy numbers, respectively, are significant relative to the secondary flows for a stationary passage. One of the most comprehensive studies in this field was performed by Johnson et al. [5] who provided area-averaged data for ribbed passages with inward and outward flow. Such average data finds direct application in the first stage of a blade cooling system de-

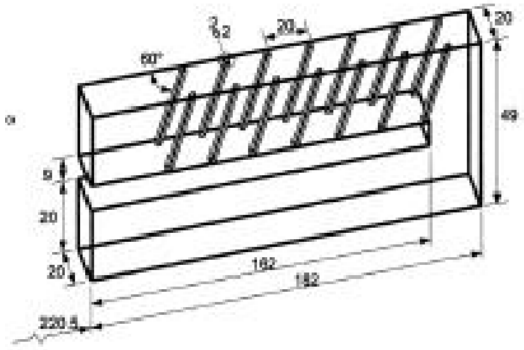

(a)

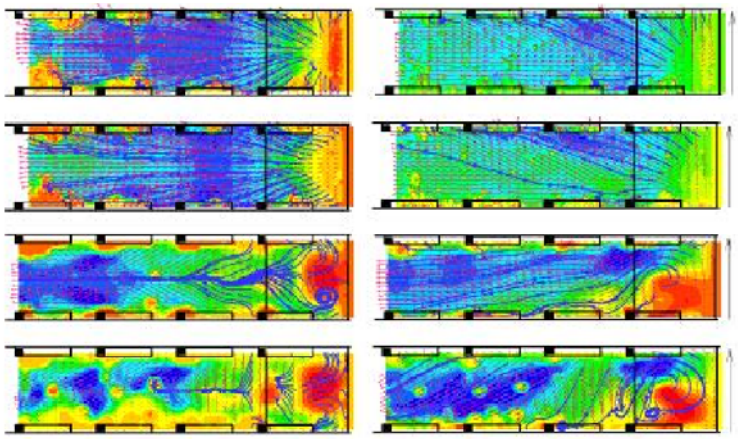

(b)

Fig. 1. PIV measurements of velocity showing the effect of rotation on secondary flows downstream of a bend in a cooling passage with 60° inclined ribs [6]. The velocity data on the left are without rotation.

sign. Over recent years, high-resolution experimental methods have been used to gain understanding of the flow physics and to allow better resolution data to be used in 3D designs. Figure 1 shows the velocity measured downstream of a bend with 60° inclined ribs installed upstream [6]. The rotation number for the data on the right is 0.33. The ribs visible in the images and measurement planes are, from top to bottom, at 5%, 15%, 85%, and 95% from the inner wall. Even with ribs with a height of 10% of the passage hydraulic diameter, rotation is seen to disrupt the pair of counter-rotating vortices present in the non-rotating case. Liu et al. [7] recently measured the effects of rotation on HTC in a triangular shaped passage fitted with 45° and 90° inclined ribs. They showed that rotation had more effect on 90° ribs than 45° ribs. Huh el al. [8] studied the effect of rib pitch in rectangular passages with 45° ribs and concluded that ribs with a pitch as close as 2.5 rib heights produced the best overall cooling.

The considerable amount of work involved in an experimental campaign to study rotating effects on HTC means that it is usually not possible to use rotating heat

Fig. 2. The Rotating Heat Transfer Rig used by Rolls-Royce to study the effect of roration on blade.

transfer measurements directly in an EDP. For this reason, rotating heat transfer experiments are normally used in research activity. A recently launched European FP7 supported program, ERICKA1, will study the effect of rotation on cooling systems with engine realistic geometries. The project will use rotating facilities at Rolls-Royce, Fig. 2, and at ONERA to quantify the effect of rotation on fully featured radial flow and impingement systems.

2.2 Application to EDP

Perspex model heat transfer experiments are used both in research activity and as part of an EDP. In the case of the latter tests, the high-resolution data can be used to check assumptions used in the cooling design. Typically, the heat transfer data

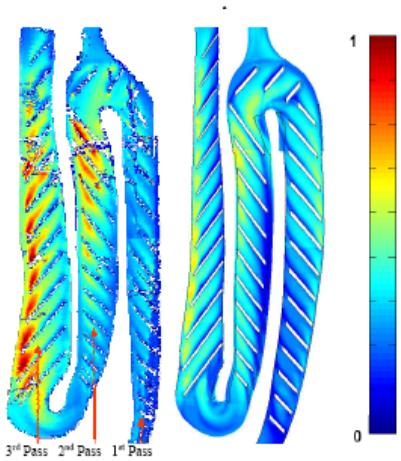

Fig. 3. Comparison between experimental HTC measurements, LHS and CFD predictions, RHS [9].

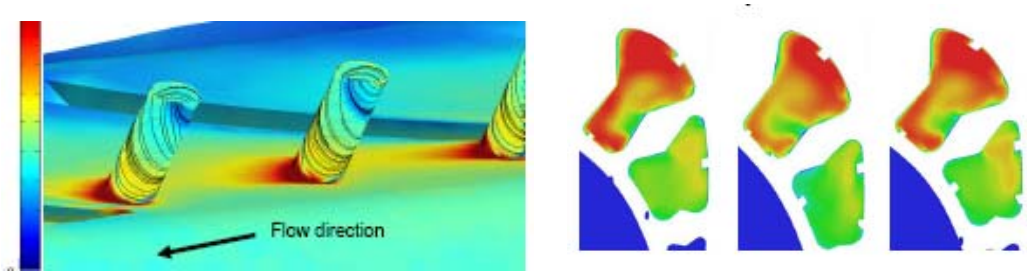

Fig. 4. Example of the fine resolution HTC data available from CFD [9].

Fig. 5. Predicted gas temperature distribution [9].

from a static model is compared to the results from CFD. For a blade cooling design, the CFD is then used to predict conditions under rotation as discussed below. A recent example of the comparison of detailed CFD to static rig test data was reported by Jackson et al. [9]. The computational results were registered to pressure drop and heat transfer measurements in a non-rotating passage. This work formed part of an EPD and enabled assumptions used in the thermal model of the blade to be evaluated before the engine was operated. Figure 3 shows both the CFD and experimental data. At the time of writing, the combined use of experiments and CFD represents the best way of feeding data into a new design. The CFD provides heat transfer data for the full surface of the cooling system so the impact of fine geometric details can be evaluated. Fig. 4 shows the HTC distribution in the vicinity of a set of film cooling hole entrances, together with the path of surface streamlines. The latter confirmed the presence of significant swirl which reduced the discharge coefficient. The latter effect has also been reported by Gritsch et al. [10].The zones of enhanced HTC downstream of the holes were confirmed on the experiments and have been reported before, e.g.,

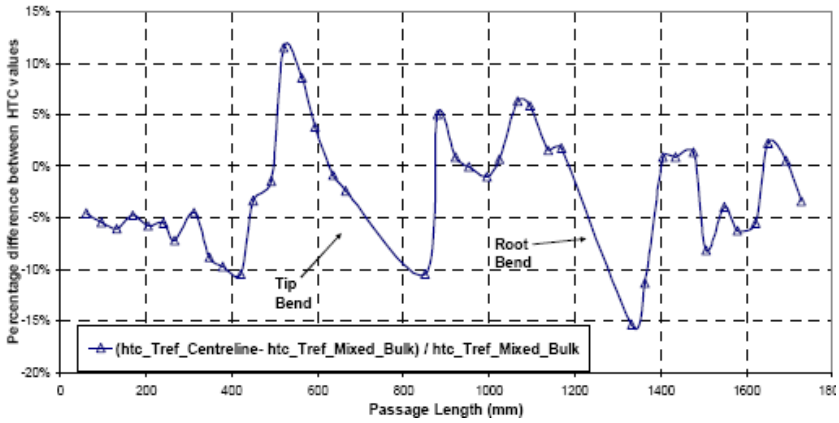

Fig. 6. Percent difference between HTC calculated using center line gas temperature and HTC from mixed bulk temperature [9].

[11]. The CFD was also used to appraise the use of single thermocouples in the experiment at selected planes for the evaluation of heat transfer coefficient. Fig. 5 shows the mid-span predicted gas temperature used to evaluate mixed bulk temperature at planes perpendicular to the flow direction. Fig. 6 shows that the use of one thermocouple per plane leads to an offset in HTC of about ±5% with slightly larger differences downstream of the bends.

Once a detailed comparison of the static rig experimental data and CFD predictions are complete, the effect of rotation is predicted by CFD. This step requires careful selection of the right turbulence model but there are reports that accurate prediction of rotating passage HTC is possible. Sleiti and Kapa [12] showed that a Reynolds Stress Model accurately predicted the 90^o rib data measured in [13]. More recently, Raisee et al. [14] reported the use of a nonlinear k–ε turbulence model in stationary and rotating ribbed ducts. Iacovides and Launder [15] give a recent review of the application of CFD to blade cooling.

3. RAPID PROTOTYPING

Rapid prototyping of components is increasingly used as a means of assessing the performance of new cooling system configurations. The technique cannot provide the high resolution HTC data that Perspex model testing can. But rapid prototype model tests can provide crucial flow data at an early stage of a new design. Once the Computer-Aided Design (CAD) geometry of a component is defined, a model can be produced, literally, overnight so that the shape of the part can be quickly reviewed in the design office. The cost of such a plastic component depends on its manufacture time but for an aircraft engine vane or aerofoil the cost is typically only a few hundred pounds. Thomas and Hodson [16] present a recent review of the application of rapid prototyping in wind-tunnel testing. They compared the geometric accuracy, porosity and practicality of test pieces manufactured by four different rapid prototyping machines.

3.1 Description of Stereo-lithography

Stereo-lithography is a class of rapid prototyping which involves the building up of the three-dimensional model in small, finite layers by hardening resin in a tank using a UV laser, Fig. 7. SL was invented more than twenty years ago [17] and has been readily available to the industry for about 15 years. Recently, aerospace engineers have used SL to manufacture test pieces for aerodynamic experimentation. For example, Dedoussis et al. [18] report application of SL models in compressor testing. Telisinghe et al. [19] used SL models of different aerofoil trailing edge models to assess the relative aerodynamic loss of different trailing edge film cooling geometries. The SL component is produced in a tank of ultraviolet (UV) curable photopolymer resin by using a laser to draw the component shape in three dimensions The CAD file is converted into a sliced (SLI) file, by chopping the model into thin layers, typi-

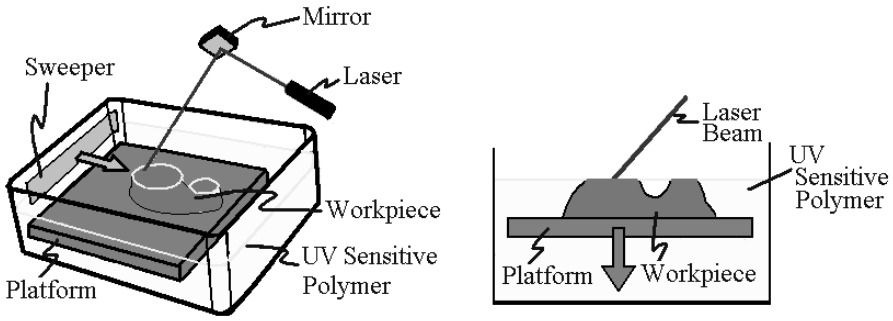

Fig. 7. The SL process [20].

cally 0.1-mm thick. The UV laser traces the full shape of the first layer and causes the liquid to solidify in a thin sheet on the surface of a horizontal platform immersed in a tank of resin. After the layer is complete, a sweeper passes through the tank at the height of the top of the layer. The sweeper prevents unhardened resin from sticking to any surface and also flattens the surface of the hardened layer. The platform then drops down by one layer thickness, and the laser solidifies the next layer. This process repeats, layer by layer, until the model is complete. The solid component is then rinsed with a solvent to remove unhardened resin. At this stage the amount of cross-linking of the polymer triggered by the laser results in a weak structure. Further hardening of the component is achieved by baking it in an ultraviolet oven to fully cure the resin.

3.2 Geometry of the SL Model

3.2.1 *Staircase roughness*

All rapid prototyping methods result in a surface roughness that can affect the flow under study. A typical modern SL machine uses a step size in the range 50×100 μm. The sides of the perimeter of each layer are essentially vertical which means that models with surfaces that are not vertical take on a staircase form. These steps inevitably create a periodic surface roughness. The size of the step can be minimized to reduce the roughness, but this is at expense of increased build time and cost.

The height and pitch of the roughness elements depend on the angle at which the surface is built relative to a horizontal platform. For small components and high speed flows, the roughness height can result in a surface that is not hydraulically smooth. In cases where the flow swept surface is on the outside of the component, the surface roughness can be reduced by gently polishing with sand paper. However, in the case of a cooling passage, it is not possible to access the internal surface.

The potential effect of this roughness on flow through passages was considered in detail by Mittal et al. [21]. Figure 8 shows four circular pipe tests pieces grown at different angles to study the effect of staircase roughness on friction factor. Each piece is shown with inlet and outlet flanges. Four 100 mm long pieces had internal

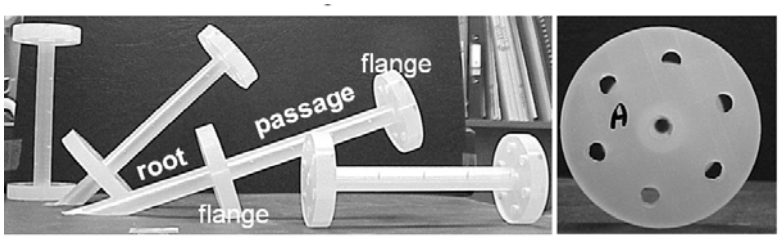

Fig. 8. Circular pipes grown at different angles to platform [21].

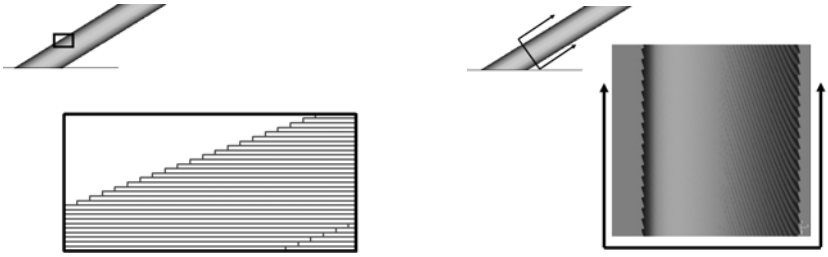

Fig. 9. Diagram showing schematically the form of the surface roughness of SL components [21].

diameters of 5 mm were grown at 0^o, 20^o, 45^o, and 90^o to the platform. Two smaller pipes with diameter 3 mm and one square section pipe with hydraulic diameter 5 mm were also tested.

The SL produces internal surface roughness that varies around the perimeter as indicated in Fig. 9. The shape of each circular section pipe surface is analogous to the shape formed from stacking a set of washers with elliptic holes. It can be seen that:

- The step size varies around the perimeter of the passage. The inset diagram to the left indicates that the step size is greatest at the highest (and lowest) points.
- The steps form grooves that are inclined to the flow direction at the build angle.

The SL pipes were tested in the small blow-down facility shown in Fig. 10. The operating pressure and scale of the models meant that engine cooling Reynolds numbers could be achieved.

To achieve a range of engine representative Reynolds numbers in the laboratory the experiments were run inside of a pressurised chamber. The chamber was pressurized to 6.89 bar (100 psi), and the test pipe vented through a calibrated choked orifice. As the pressure drops in the chamber, the density and temperature of the air also decrease and the mass flow through the pipe reduces. A set of low range, piezoresistive differential pressure transducers were used to measure the static pressure difference between pairs of adjacent tappings. The transducers were placed inside the pressure chamber in order to minimize common-mode error and to enable the use of sensitive transducers.

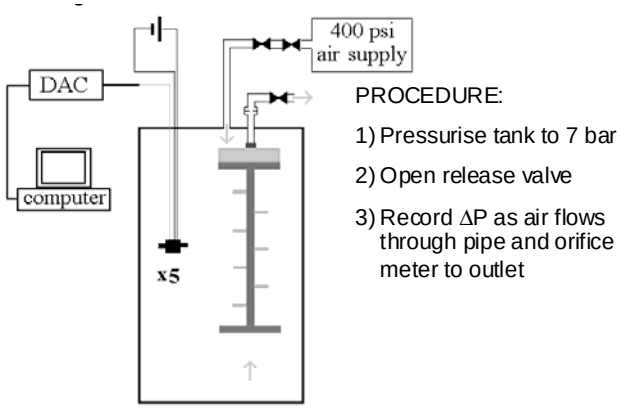

Fig. 10. Schematic of facility used to measure *f* for SL pipes [21].

Data from a representative blow-down experiment is shown in Fig. 11 where each line is the signal from an individual transducer.

Figure 12 shows the measured friction factor as a function of Reynolds number for all of the pipes tested. The top left hand chart shows the data for a smooth brass pipe used to confirm the accuracy of the experimental method. The SL pipe data confirm that the surface roughness has increased the friction factor. The green dashed line was calculated from the Colebrook equation [22] where the area average equivalent sand grain roughness of the SL process has been estimated from a Talysurf measurement of the greatest roughness line multiplied by $2/\pi$ and by the cosine of the build angle. The law of the wall method was an attempt to account for the change in roughness with perimeter in the SL pipe by adapting an approach used for passages with two facing rib walls and two connecting smooth walls. The latter was introduced for rib passages by Mayle [23] and its development for SL pipes is reported in [24]. This approach gives better agreement to the data but requires more calculation.

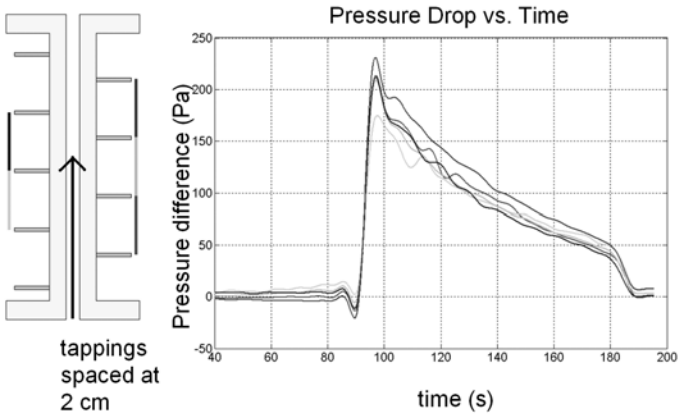

Fig. 11. Raw pressure data for the 5-mm diameter pipe grown at 20^{o} [21].

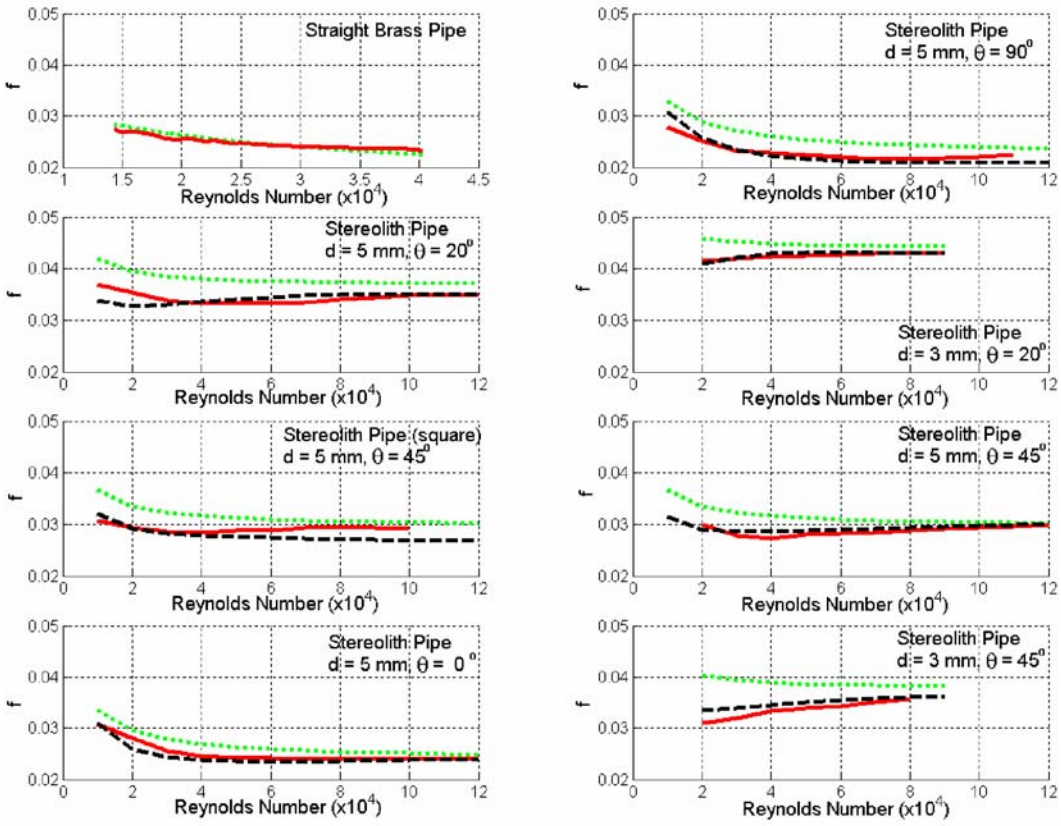

Fig. 12. Friction factor results: experimental (red solid), law of the wall prediction (black dashed), and Colebrook prediction [22] (green dotted) [21].

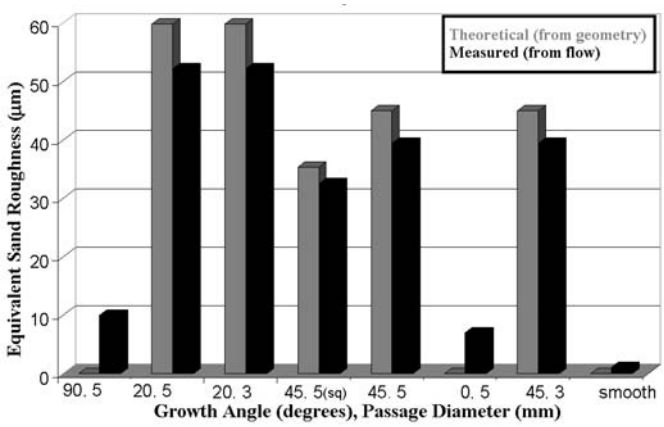

Fig. 13. Equivalent sand grain roughness in microns. The data labels are growth angle and pipe diameter, respectively.

The friction factor data was then used to calculate the equivalent sand from the Colebrook equation and the results are presented in Fig. 13. The results show that pieces with the same growth angle exhibit the same equivalent sand roughness regardless of pipe diameter. The step height at the wall is equal to the build step size times the cosine of the build angle. If we ignore the pipe grown at 0^o, the test pieces grown at 20^o should have the highest element height and greatest equivalent sand roughness. The pieces grown at 90^o should have the smallest element height and equivalent sand roughness. Both of these observations are consistent with the data. Theoretically, the pipe grown at 0^o has the largest steps, but these steps are aligned with the flow to form ridges. This feature indicates that the use of a simple derived step height to calculate equivalent sand grain roughness is an approximation to SL surface roughness.

3.2.2 *Shrinkage and growth*

The resin curing process results in linear shrinkage of the model which can be compensated for. The amount of shrinkage depends on the resin used but is typically 0.1–0.2% in directions parallel to the platform. Shrinkage in the orthogonal direction is normally smaller than this. Most SL machines allow this to be compensated for during manufacture and, in practice, this is not usually a problem. Early SL resins absorbed moisture over time which led to a gradual swelling of the component. More recent resins are moisture resistant which increases the stability of the model.

3.2.3 *Other deviations*

When the SL component grows at inclination to the vertical, it is often necessary to include a support structure, or scaffold, to strengthen the model. The scaffold is removed once the model is taken out of the tank and the attachment locations smoothed by abrasion. It is not possible to include supports for internal walls so accuracy of the latter depends on the strength of the model. This effect can cause the walls of inclined film cooling holes to sag and this reduces the flow area. For this reason, SL models are often grown with orientations resulting in the film axes growing at 90^o to the platform.

3.3 Accuracy of Flow Controlling Areas

Many cooling system designs include part of the flow path with a flow area being significantly smaller than the rest of the system. This area effectively sets the coolant flow rate and is usually accurately manufactured by laser or by Electro Discharge Machining. Fortunately, this means that this zone of an RP model is also accessible for machining — specifically drilling.

3.4 Heat Transfer Measurements

The conventional transient heat transfer technique is not used for SL models for two reasons.

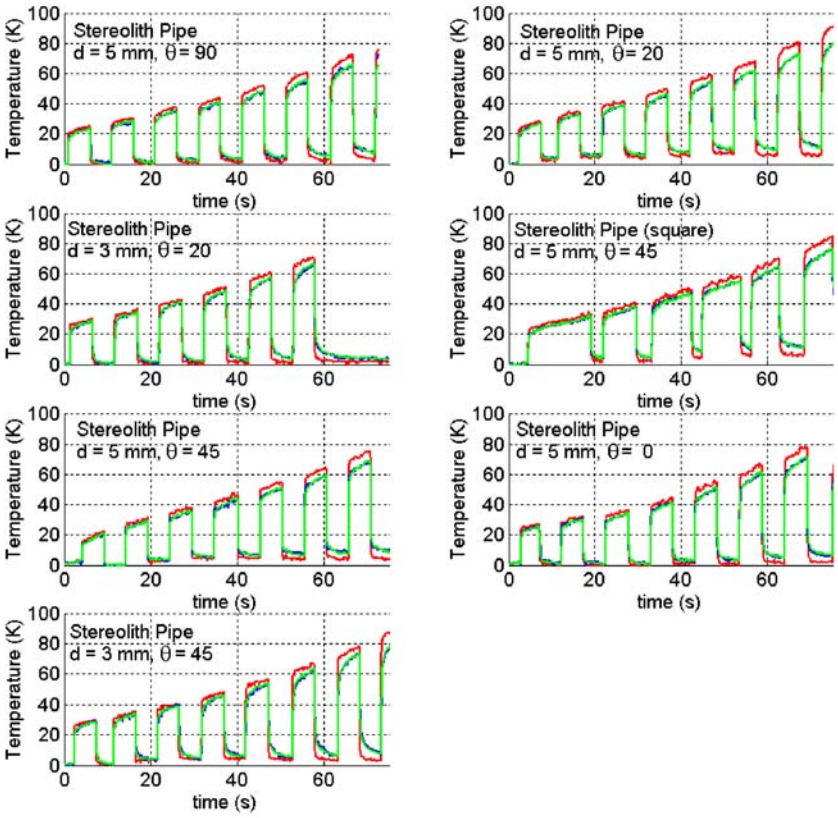

Fig. 14. Gas temperature measurements for the SL pipes tested by Mittal et al. [21]. The red line is the inlet temperature, the blue line is the measured outlet temperature, and the green line is predicted from a regression procedure — after [24].

- SL resin is not transmissive so there is no optical access to a coating applied to the inner surface. Techniques that rely on measuring the temperature on the outer surface of the test piece are known to be inaccurate. However, it is worth noting that recent progress in SL technology has introduced plastics that, when polished, are transmissive so this constraint may disappear.
- The thermal properties are not well characterised and are not isotropic.

Sl models can be used to determine average HTC between planes where gas temperature measurements can be made. This approach was employed in Perspex models [25], and it uses the enthalpy change between planes to determine heat loss. In its simplest form, the method extrapolates the temperatures to the start of a thermal transient when the model temperature is uniform and known. The technique used by Mittal et al. [21] models the temperature of the test piece during gas temperature transients to enable the temperature changes following a series of gas temperature transients to be analysed.

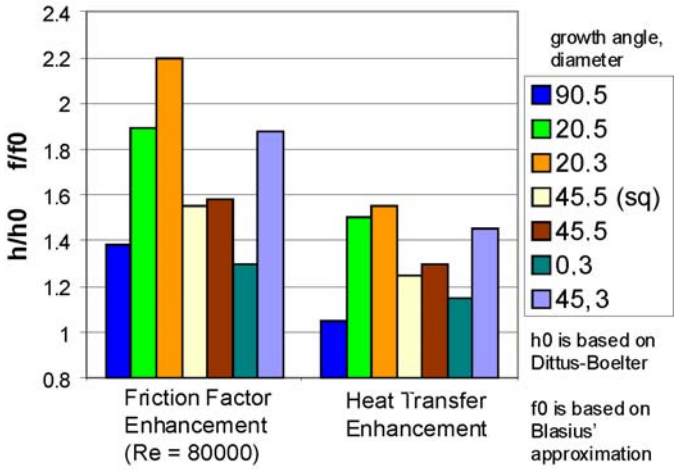

Fig. 15. HTC and f enhancement data for the SL pipes [24]. Key is growth angle and hydraulic diameter, respectively.

Figure 14 shows data used to determine the change in HTC caused by the staircase roughness intrinsic in the SL process.

The HTC enhancement is compared to the friction factor increase in Fig 15. The chart shows that:

- SL models cannot be used to represent smooth passages when the models have small diameters.
- The SL roughness is worse for shallow growth angles, although zero degrees is an exception.
- Friction factor enhancement is greater than the HTC enhancement.

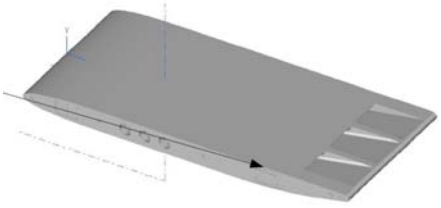

Fig. 16. CAD model of trailing edge cut back model used by Telisinghe [26].

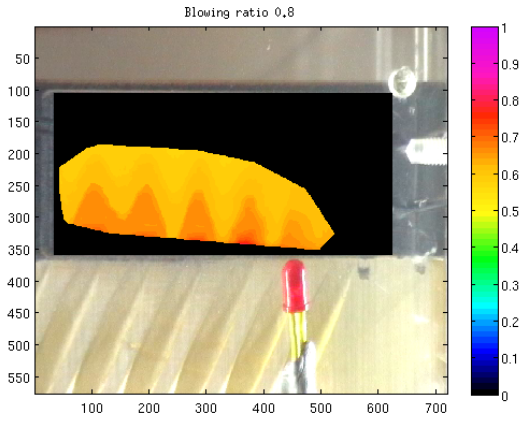

Fig. 17. Film effectiveness measured at the trailing edge of an SL model by Telisinghe [26].

Another means of making heat transfer measurements with SL models is to insert an insulated heater pad into the region of interest. This approach was used by Telisinghe et al. [19] who studied the cooling effectiveness and aerodynamic loss of different trailing turbine blade edge models. Their original flat plate geometry, Fig. 16, was derived from the engine CAD model which enabled the results to produced in time to influence the engine project. Figure 17 shows the film effectiveness measured at the trailing edge.

4. USE OF EXPERIMENTS IN OPTIMISATION STUDIES

The successful integration of parameterized CAD, meshing and CFD software has enabled engineers to perform extensive parametric studies of the effect of key geometric parameters on performance. Namgoong et al. [27] recently applied this strategy to the reduction of pressure loss around a 180 bend and arrived at a geometry that reduced the bend loss by 67%. The optimum geometry was derived from CFD that has known limitations for the accurate prediction of separations. Since all of the geometries studied had, of necessity, been CAD modeled, it was straightforward to confirm the performance of the optimum bend by low pressure testing with SL models.

During the optimization phase, the U-bend was parameterized by using NX2-Knowledge-Fusion. The design variables were chosen to be control point locations of a spline curve as shown as the black dots in Fig 18. The passage is symmetric so the red dots are not independent.

A total of 24 parameters were used and each design variable bounded to reflect practical constraints. Figure 19 shows an example parameterized U-bend. The U-bend optimization process requires a Navier–Stokes solver to model the effect of viscosity on the bend flow. In order to obtain a converged solution for this problem, FLUENT required about three hours computational time using 8 parallel Intel 2.4 GHz CPUs.

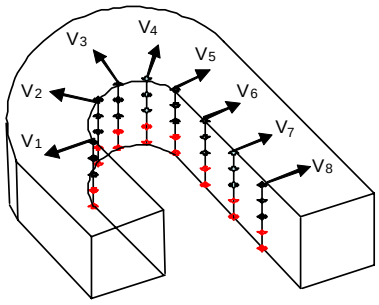

Fig. 18. Schematic of design variables.

Fig. 19. U-bend modeled by using NX-Knowledge-Fusion.

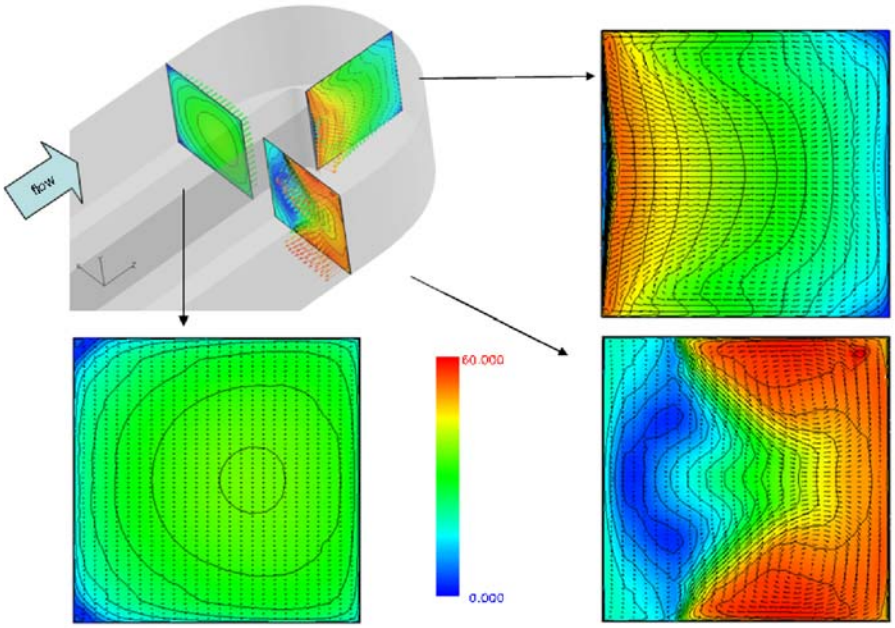

Fig 20. Contours of velocity for the standard bend showing the large separation at the inner wall.

A typical mesh comprised 6.3 million elements with y^+ levels of approximately 1.1. This high computational cost meant that it is prohibitively expensive to use a direct numerical optimization approach. This is the case, even for gradient-based optimization which requires less computational time than a stochastic based algorithm, i.e., Genetic Algorithm (GA). This heavy computation cost led the authors to use a DOE (Design of Experiment) based data set generation and surrogate design space approach. The use of a surrogate model for object function evaluation is much cheaper than the CFD evaluation but depends on the surrogate model accurately representing the design space.

Operation of the NX, ICEM CFD, and FLUENT programs was combined using a script code to complete DOE data set with input design variables from iSIGHT and output values, i.e., static pressure difference (objective function values) for the surrogate design space model. Because each CFD run is computationally expensive, it was necessary to reduce the computational time as much as possible. For this reason, interpolation of the solution from the base geometry was used for initialization which reduced the time for convergence significantly. To further save computational time, a one equation turbulence model [28] was selected. Figure 20 shows the predicted separation at the inner wall of the standard bend. The separation ensures that the flow is not diffused reversibly, and this leads to a bend loss coefficient of 1.8. Figure 21 shows that changes to the inner wall shaped for the 2D optimum passage have kept the flow attached to the wall.

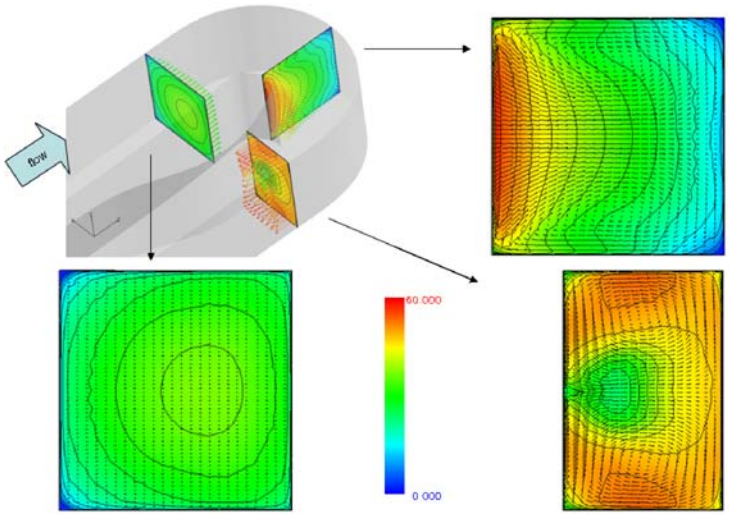

Fig. 21. Contours of velocity for the optimized bend showing the elimination of the separation at the inner wall.

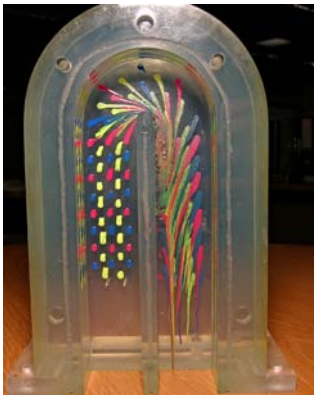

Fig. 22. SL model of the standard bend.

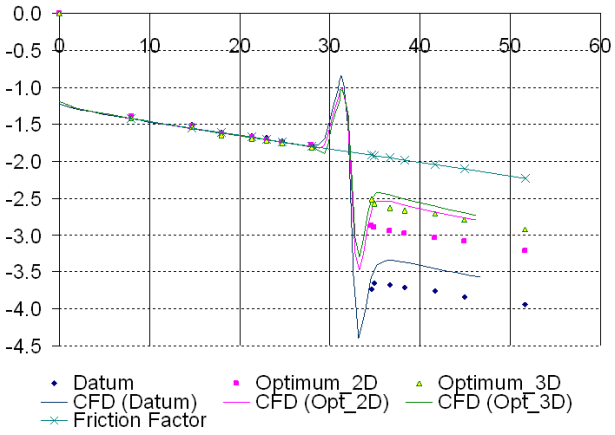

Fig. 23. Static pressure divided by dynamic head (vertical axis) versus distance divided by passage.

Figure 22 shows the SL model of the datum bend with the cover plate removed. Flow enters from the bottom left. The oil dots confirm the size of the inner wall separation. The SL models were instrumented with static pressure tappings and Fig. 23 shows the reduction in static pressure, divided by duct dynamic head for the passages modeled. The straight line labeled "friction factor" is calculated from an equation for turbulent flow through ducts. The excellent agreement to the data ahead of and downstream of the bend confirms that the SL roughness has not affected the

pressure drop. In these cases, the models were grown with zero inclination to the SL platform with square section dimension of 30 mm. Close inspection of the results shows that there is a slight discrepancy between the CFD and experimental results. The disagreement is greatest at 14% for the datum configuration, the standard bend, which has the largest separation. It can be seen that the CFD predicts the loss for the bends studied in the correct order and most importantly, the optimization strategy has produced a bend with significantly less loss than the datum. The speed at which the models were produced and tested enabled data to be available for the EDP.

5. CONCLUSIONS

Perspex models are still used in flow and heat transfer tests in the development of gas turbine cooling systems. Their traditional application is in research programs where experiments are performed to develop CFD simulations. Current research activity in this field includes studies of fully featured and rotating cooling systems. In addition, the level of accuracy of HTC required for an EDP means that Perspex tests are required to register the CFD on static experiments.

For many internal cooling geometries it is not possible to smooth the surface of an SL model before tests. In such cases, the suitability of a SL model for engine simulation depends on whether the model can be designed at a scale that makes the SL roughness small enough to leave the passage hydraulically smooth. In practice, this means that experiments need to be designed carefully so that roughness effects do not influence the conclusions of an experimental program.

Provided the experiments are carefully designed, SL models can play an important part in the development of news systems. The speed with which models can be manufactured from an existing CAD geometry means that flow experiments can be performed in time to play a part in an engine project. A recent example is in the confirmation of the performance of a new bend share derived entirely from CFD.

ACKNOWLEDGMENTS

The author thanks Rolls-Royce for permission to publish this paper. He is also very grateful to Dr. Janendra Telisinghe who performed the film cooling work and Mr. Nick Carter who produced all of the models in the rapid prototyping facility at Rolls-Royce Bristol.

REFERENCES

1. Ireland, P. T. and Jones, T. V. Liquid crystal measurements of heat transfer and surface shear stress, *Meas. Sci. Technol.*, 2000, Vol. 11, pp. 969–986.
2. Weigand, B., Semmler, K., and von Wolfersdorf, J. Heat transfer technology for internal passages of air-cooled blades for heavy-duty gas turbines. In: *Heat*

Transfer in Gas Turbine Systems, *Annals New York Acad. Sci.*, Vol. 934, pp. 179–193, 2001.

3. Poser, R., von Wolfersdorf, J., and Semmler, K. Transient heat transfer experiments in complex passages, *ASME Heat Transfer Conf.*, San Francisco, HT 2005–7226, 2005.
4. Poser, R., von Wolfersdorf, J., and Lutum, E. Advanced evaluation of transient heat transfer experiments using thermochromic liquid crystals. In: *Proc. Inst. Mech. Engineer, Part A: J. Power Energy*, 2007, Vol. 221, pp. 793–801.
5. Johnson, B. V., Wagner, J. H., and Steuber, G. D. Effects of Rotation on Coolant Passage Heat Transfer, NASA Contractor Report 4396, Vol. II, 1993.
6. Brossard, C., Servouze, Y., Gicquel, P., and Barrier, R. Caracterisation par PIV de l'ecoulement dans un canal en U tournant et muni de perturbateurs, *Congres Francophone de techniques laser*, Toulouse, 19–22 Septembre, 2006.
7. Liu, Huh, Moon, and Han,**[Q3]** High Rotation Number Effect on Heat Transfer in a Triangular Channel with 45, Inverted 45 and 90 Degree Ribs, ASME Paper GT2009-59216, 2009 (presented at the Int. Gas Turbine Conf. in Orlando).
8. Huh, Liu, Han, and Chopra, **[Q4]**.Effect of Rib Spacing on Heat Transfer in a Two-Pass Rectangular Channel (AR = 1:4) with a Sharp Entrance at High Rotation Numbers, ASME Paper GT2008-50311, 2008 (presented at the Int. Gas Turbine Conf. in Berlin).
9. Jackson, D., Ireland, P. T., and Cheong, B. Combined experimental and CFD study of a HP blade multi-pass cooling system, ASME Paper GT2009-60070, Turbo Expo Orlando, 2009.
10. Gritsch, M., Schulz, A., and Wittig, S. Effect of internal coolant crossflow on the effectiveness of shaped film cooling holes, *J. Turbomachinery*, 2003, Vol. 125, pp. 547–554.
11. Shen, J.-R., Ireland, P. T., Wang, Z., and Jones, T. V. Heat transfer enhancement within a turbine blade cooling passage using ribs and combinations of ribs with film cooling holes, *J. Turbomachinery*, 1996, Vol. 118, pp. 428–434.
12. Sleiti and Kapa, 2004 **[Q2]**
13. Wagner, J. H., Johnson, B. V., Graziani, R. A., and Yeh, F. C. Heat transfer in rotating serpentine passages with trips normal to the flow, *J. Turbomachinery*, 1992, Vol. 114, pp. 847–857.
14. Raisee, M., Naeimi, H., Alizadeh, M., and Iacovides, H. Prediction of flow and heat transfer through stationary and rotating ribbed ducts using a non-linear k–ω model, *Flow Turb. Comb.*, 2009, Vol. 82, pp. 121–153.
15. Iacovides, H and Launder, B. E. Internal blade cooling: the cinderella of CFD research in gas turbines. In: *Proc. Inst. Mech. Engineers, Part A: J. Power Energy*, 2007, Vol. 221, pp. 265–290.
16. Thomas, R. and Hodson, H. P. Rapid prototyping for wind tunnel testing and instrumentation, *XIX Biannual Symp. on Measuring Techniques in Turbomachinery*, April 7–8, 2008, ISBN 978-2-930389-32-X, 2008.

17. Hull, C. Apparatus for Production of Three-Dimensional Objects by Stereolithography, U.S. Patent 4,575,330, 1986.
18. Dedoussis, V., Canellidis, V., and Mathioudakis, K. Aerodynamic experimental investigation using stereolithography fabricated test models: the case of a linear compressor blading cascade. In: *Virtual and Physical Prototyping*, Vol. 3, Issue 3, 2008, pp. 151–157.
19. Telisinghe, J. C., Ireland, P. T., Jones, T. V., Barrett, D., and Son, C. Comparative study between a cut-back and conventional trailing edge film cooling system, ASME Paper GT2006-91207, Turbo, Barcelona, Spain, 2006.
20. Jacobs, P. F. Stereolithography and Other RP&M Technologies, ASME Press, Fairfield, NJ, 1996.
21. Mittal, V., Ireland, P. T., and Mitchell, M. Predicting the friction factor and Nusselt number in stereolith pipes, *9th UK Nat. Heat Transfer Conf.*, Manchester, **[Q5]** 2005.
22. Colebrook, C. F. Turbulent flow in pipes, with particular reference to the transition region between the smooth and rough pipe laws, *J. Inst. Civ. Eng. Lond.*, 1939, Vol. 11, pp. 133–156.
23. Mayle, R. E. Pressure Loss and Heat Transfer in Channels Roughened on Two Opposed Walls, ASME Paper 89-GT-86, 1980.
24. Mittal, V., Ireland, P. T., and Mitchell, M. An analytic model of roughness and its effects on friction factor in circular pipes made by stereolithography, submitted for publication in *J. Aerospace Eng*., 2009. **[Q6]**
25. Tsang, C. L., Ireland, P. T., and Dailey, G. M., Reduced instrumentation testing of blade cooling passages. In: *Proc. AVT Conf. Advanced Flow Management*, Leon, Norway, 2001. **[Q7]**
26. Telisinghe, J. C. Trailing Edge Film Cooling Systems, D. Phil., University of Oxford, 2009.
27. Namgoong, H., Son, C. M., and Ireland, P. T. U shaped turbine blade cooling passage optimization, *12th AIAA/ISSMO Multidisciplinary Analysis and Optimization Conf.*, **[Q8]** Seattle, 2008.
28. Spalart, P. R. and Allmaras, S. R. A One-Equation Turbulence Model for Aerodynamic Flows, AIAA Paper 1992-0439, 1992.

[Q4] Cheong, C. Y., Ireland, P. T., and Siebert, A. W. High performance single phase liquid coolers for power electronics, *3rd Int. Conf. on Microchannels and Minichannels*, **[Q9]** June 13–15, 2005, Toronto, Canada, 2005.

[Q4] Poser, R., von Wolfersdorf, J., Lutum, E., and Semmler, K. Transient Heat Transfer Experiments in Blade Cooling Circuits Using Thermochromic Liquid Crystals, ASME Paper GT2008-50364, *Turbo Expo*, Berlin, June 2008.

[Q4] Tsang, C. L., Gillespie, D. R. H., Ireland, P. T., and Dailey, G. M. Detailed thermal analysis of transient heat transfer experiments. In: *Proc. 8th Int. Symp. Transport Phenomena and Dynamics of Rotating Machinery*, **[Q10]** Hawaii, USA, 2000.

□◆◆◆□

Heat Transfer Research, 2010, Vol. 41, No. 8

Trailing Edge Film Cooling of Gas Turbine Airfoils — Effects of Ejection Lip Geometry on Film Cooling Effectiveness and Heat Transfer

TIM HORBACH,* ACHMED SCHULZ, and HANS-JOERG BAUER

Institut fuer Thermische Stroemungsmaschinen (ITS),
Karlsruhe Institute of Technology (KIT), 76131 Karlsruhe, Germany

The present paper concentrates on trailing edge film cooling of modern high-pressure turbine blades using cooling ejection through planar slots with a pressure side cutback. The experimental test section consists of a generic scaled-up trailing edge model. The effects of different geometric configurations on the structure and the performance of the cooling film are investigated in terms of film cooling effectiveness, heat transfer coefficients, and discharge behavior. The interaction between an internal turbulator array of ribs with the ejection slot lip is of major interest. Different designs of the cooling ejection lip are applied. Four different ratios of lip thickness to ejection slot height (t/H = 0.2, 0.5, 1.0, 1.5) are investigated, as well as three different lip contours representing typical manufacturing imperfections and wear. The experiments are performed at engine-realistic density ratios. The blowing ratios are varied between $0.2 < M < 1.25$. The results show a strong dependency on ejection lip thickness and only marginal changes when the lip shape is varied.

* * *

Keywords: rib array, heat transfer coefficients, discharge coefficients, blade cooling, flow interaction, internal turbulators, cooling design, slot, blowing ratio

1. INTRODUCTION

The development of gas turbine engines is determined by growing economical and ecological requirements. Recent developments of gas turbines for aeropropulsion show

*Address all correspondence to Tim Horbach E-mail: tim.horbach@its.uni-karlsruhe.de

ISSN1064-2285

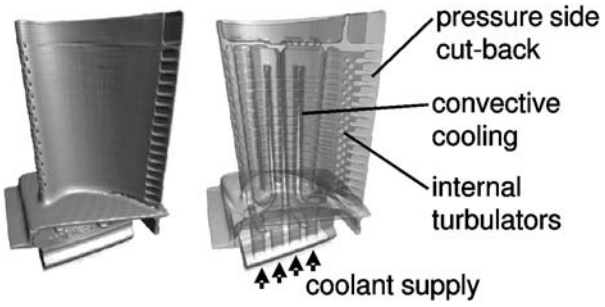

Fig. 1. Cooling design of a high pressure turbine blade.

overall pressure ratios beyond 50 and turbine inlet temperatures in excess of 2000 K. Sophisticated cooling schemes, therefore, play a pivotal role in the design process of hot gas components like, e.g., combustor liners and high pressure turbines. The cooling design has to bridge the gap between continuously increasing hot gas temperatures and pressures (coolant temperatures) and the allowable material temperatures, which increased marginally during recent years.

Trailing edge cooling, in particular, is subject to structural and aerodynamic constraints. Heat needs to be removed from a region of the airfoil, which should be as thin as possible to minimize aerodynamic losses. Cutting back the pressure surface at the trailing edge of an airfoil and forming a continuous ejection slot is a well established technique to satisfy this requirement (see Fig. 1). The ejected cooling film acts as an insulating layer to prevent hot gas from impinging onto the wall and serves at the same time as a convective sink for the heat transferred to the suction surface and conducted through the wall. To counteract the structural weakening by the ejection slots, the opposing walls forming the trailing edge coolant passage are connected by arrays of ribs or pins. Their purpose is not only to account for the airfoil's structural integrity, but also to act as turbulators to enhance the internal convective heat transfer in the coolant passage.

Numerous studies on film cooling have been published in the past. Only few publications dealing with cooling ejection on a trailing edge pressure-side cutback exist. The effects of the ejection lip thickness on the film cooling effectiveness, e.g., have been experimentally investigated by Kacker et al. [1] and Sivasegaram et al. [2]. Two-dimensional slots without internal geometry were investigated at density ratios close to unity. They found a significant influence of the ejection lip thickness. More investigations on this subject were done by Taslim et al. [3]. Besides ejection angle, slot width, and density ratio, they varied the slot lip thickness to height ratio between 0.5 and 1.25 and concluded that the film cooling effectiveness decreases as the lip thickness is increased due to intensified vortex shedding effects at the ejection lip. Numerical and experimental studies were done by Holloway et al. [4], who identified unsteady vortex shedding from the ejection lip as the major driving mechanism for the mixing of a coolant and hot gas.

Martini et al. [5–7] performed various numerical and experimental studies on the variation of internal cooling design including pin fin and rib arrays. An increasing number of authors used numerical methods to visualize and analyze the mixing processes involved in film cooling. Martini et al. [8] and Joo and Durbin [9] apply hybrid turbulence models in their numerical approaches, since the complex three-dimensional mixing flow structure cannot be predicted reliably by conventional statistical methods (RANS). To gain an indepth understanding of the coolant mixing processes, the present study focuses on the interaction between internal geometry and the ejection lip. It is to be observed, how the lip shape affects the mixing and how the findings can be exploited in future designs.

2. EXPERIMENTAL SETUP

2.1 Test Facility

The experiments are conducted in an atmospheric open loop wind tunnel. A schematic of the facility together with its characteristic data is given in Fig. 2. The test rig is supplied with air by a radial compressor. The air is heated up in an electric heater unit and passes mixers and flow straighteners before it enters the rectangular test channel (105 mm × 220 mm) through a high contraction nozzle. By this, a homogeneous temperature and velocity field at the entrance of the test section are guaranteed. Upstream of the test section, a turbulence grid is inserted into the flow channel to set a turbulence level of Tu = 7% at the slot exit. In order to establish a new boundary layer with a well defined state and thickness at the ejection lip, part of the main flow is bled off through the bottom wall. The bleed air bypasses the test section and is fed back downstream of the test section.

The coolant air is supplied by a rotary screw compressor at ambient temperature. Its maximum mass flow of approximately 50 g/s is sufficient to cover all operating conditions. The coolant enters the test section through the bottom wall, where the tur-

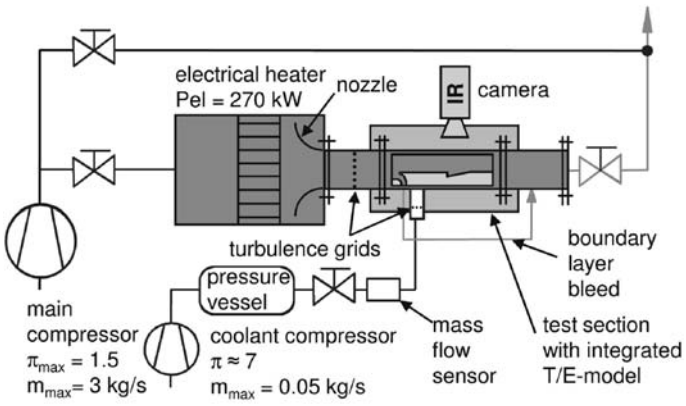

Fig. 2. Trailing edge test facility.

bulence level is increased by a grid. The coolant mass flow is measured upstream of the test section by a hot film mass flow.

2.2 Test Section

The test section contains the generic model of a film-cooled high-pressure turbine blade with a pressure-side cut back configuration. The scaled-up model represents the trailing edge section of the airfoil with tangential slot ejection. A detailed drawing is given in Fig. 3. The main flow enters the test section from the left side. A guiding element separates the incoming boundary layer. The tip of the guiding element passes over into a planar surface that represents the pressure side wall of the airfoil (L0–L2). The linear slot for the cooling ejection is located 158 mm downstream of the leading edge of the boundary layer bleed.

The coolant flow enters the test section from the bottom side. It is guided through an arrangement of turbulators before being ejected onto the cut-back surface. The turbulator section comprises two different regions with two rows of ribs. A convergent region (L1) is followed by a channel with constant cross-sectional area containing a second row of ribs (L2). Since the L2-ribs are shorter than the whole L2-region, a lip overhang with the length of two slot heights remains to support the development of a closed cooling film downstream of the ribs. The cooling air is ejected tangentially onto the inclined test surface.

The L3-region, where the mixing of coolant and main flow takes place, is the primary object of this study. Therefore, a sapphire window is mounted in the top channel wall opposite the L3 surface to provide optical access for the infrared measurement technique applied. The test plates, where the thermographic measurements are taken, consist of different materials, depending on whether a nearly adiabatic experiment or a heat flux experiment is conducted. All other parts of the test section are made of

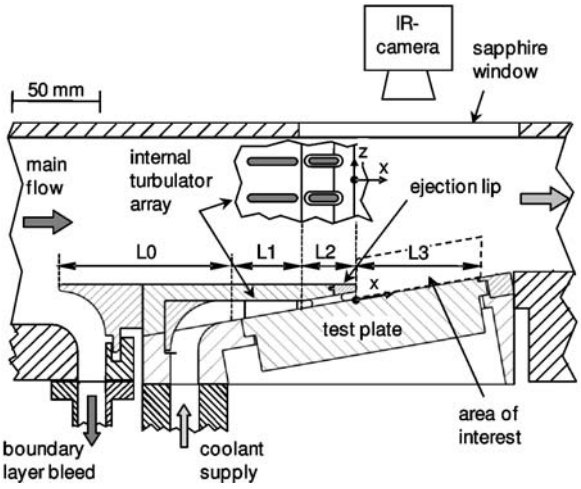

Fig. 3. Generic test section for trailing edge film cooling experiments with varying ejection lip geometry.

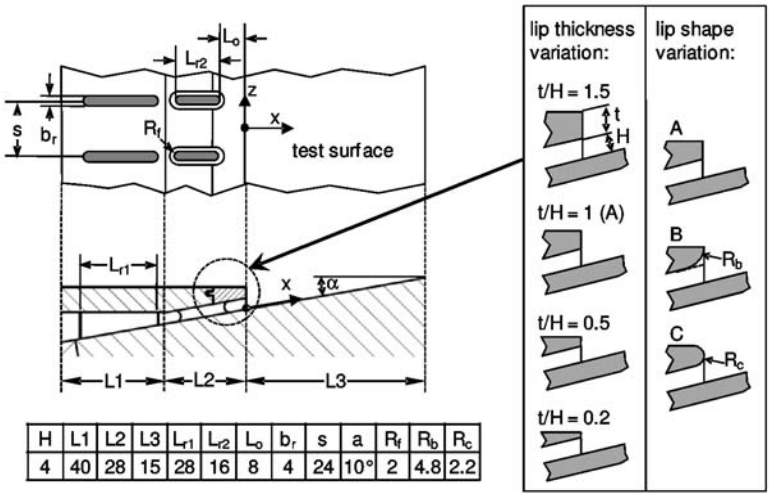

H	L1	L2	L3	L_{r1}	L_{r2}	L_o	b_r	s	a	R_f	R_b	R_c
4	40	28	15	28	16	8	4	24	10°	2	4.8	2.2

Fig. 4. Geometry description (all dimensions in mm).

steel. The test section also offers very good accessibility from the lateral walls, allowing for various measuring techniques like, e.g., laser optical diagnostics or schlieren visualization.

The modular design of the test section permits an easy assembly of different cooling configurations. The arrangement and shape of turbulators and ribs can easily be varied. In the present study, a double in-line rib array is chosen as internal geometry. A detailed description of the arrangement is given in Fig. 4. The thickness of the ejection lip is varied from t/H = 0.2 to t/H = 1.5. The shape of the ejection lip is varied, as well. The rounded contours represent typical features of manufacturing (Shape B) and wear (Shape C). The shape modifications are derived from the reference case (Shape A) with a lip thickness of t/H = 1. Material was taken off to generate the rounded contours. Hence, these cases can be considered to have a nominal lip thickness of t/H = 1, as well.

The measurements concentrate on the film-cooled surface in the near slot region with a stream wise length of 15 times the slot height (L3). To determine the adiabatic film cooling effectiveness and the heat transfer coefficients two experiments are conducted for each operating point with different thermal boundary conditions along the L3-wall. This is done by using two different test plates with a wall thickness of 30 mm each in order to maximize the accuracy of the wall heat flux measurements (Bi ≈ 1). One is made of polyetheretherketone (PEEK), a high temperature resistant plastic material with a very low thermal conductivity of λ = 0.25 W/(m·K). This nearly adiabatic test plate extends approximately 60 mm into the coolant cavity. The second test plate is used for experiments with an elevated wall heat flux. It is made of a titanium alloy ($TiAl_6V_4$) and covers solely the L3-region. A solid copper block is fixed to the bottom side of this test plate. The copper block is heated by means of a controlled electric heater (1.5 kW). To ensure a uniform temperature dis-

tribution at the lower surface of the test plate the thermal contact between copper block and test plate is supported by a liquid metal heat-conductive paste ($\lambda \approx 40$ W/(m·K)). To reduce the step in surface temperature from the L2- to the L3-region, the suction side equivalent wall upstream of the test plate is heated by heater foil elements.

2.3 Operating Conditions

All experiments were conducted at constant main flow conditions. The hot gas temperature was set to 500 K and the Reynolds number was defined as follows:

$$\mathrm{Re}_{\mathrm{hg}} = \frac{u_{\mathrm{hg}} \rho_{\mathrm{hg}} L}{\mu_{\mathrm{hg}}} = \frac{u_{\mathrm{hg}} \rho_{\mathrm{hg}} (\mathrm{L0+L1+L2})}{\mu_{\mathrm{hg}}} \tag{1}$$

and set to $\mathrm{Re}_{\mathrm{hg}} = 250{,}000$. The corresponding main flow velocity was 57 m/s. The relevant flow quantities of the main flow were measured by a thermocouple and a traversable Pitot probe in the hot gas flow above the ejection slot ($x = 0$). Additional flow field measurements revealed that the boundary layer thickness of the main flow at the slot exit is approximately $\delta_{99}/H \approx 1.6$. The coolant flow was varied to cover a wide range of the blowing ratio, which is defined as the ratio of mass fluxes of coolant and main flow:

$$M = \frac{\rho_{\mathrm{c}} u_{\mathrm{c}}}{\rho_{\mathrm{hg}} u_{\mathrm{hg}}} = \frac{\dot{m}_{\mathrm{c}}}{A_{\mathrm{c}} \rho_{\mathrm{hg}} u_{\mathrm{hg}}}, \tag{2}$$

A_{c} represents the area of the mere coolant slot, without considering the throat between the ribs. The test matrix of each geometric configuration comprises eight different blowing ratios ranging between $0.2 < M < 1.25$ in steps of 0.15. Depending on the operating point the coolant temperature at the slot exit varies from 300 K to 330 K, which results in engine-realistic density ratios ranging from $\rho_{\mathrm{c}}/\rho_{\mathrm{hg}} = 1.5$ to 1.65.

2.4 Measuring Technique and Data Processing

The thermographic measurements are mainly performed with an infrared camera (FLIR SC6000) that uses an InSb-type FPA detector. The spectral range of the detector is 3.0 to 5.0 microns and the dimensions and speed of the FPA is 640 × 512 at 30 frames per second. The camera is placed above the test channel and provides a spatial resolution of the test surface of approximately 0.30 mm per pixel with the used optical setup. Noise reduction is achieved by averaging 10 single frames at each measurement. The radiance of the test plate is enhanced by using a special high-emissive coating with a constant emissivity of $\varepsilon = 0.95$ over a wide range of viewing angles. The wall temperatures are derived by an in-situ calibration method, which utilizes several thermocouples embedded into the test surface. The thermocouples are spread over the surface in order to cover most of the temperature range on the test

surface. The response curve of the camera is determined in advance by an adequate test setup. The raw signal is then fitted to the thermocouple readings. Further details on the calibration technique are given in [10].

The local conductive heat flux distributions through the test surface are derived from a numerical 3D heat flux calculation using a finite volume approach. The thermographically gained surface temperature distributions serve as a boundary condition on a three-dimensional model of the test plate. The bottom side boundary condition is gained from an interpolation of the thermocouple readings at the lower test plate wall and the lateral wall boundary conditions are considered as adiabatic. Heat transfer coefficients in convective flows are based on the convective heat flux. Hence, a small deviation between the conductive heat flux from the simulation and the convective heat flux caused by radiation with surrounding walls needs to be taken into account. Since there is a considerable temperature difference between the mean test surface temperature and the temperatures of the surrounding walls, radiation cannot be neglected. In this study, this is accounted for by a three-dimensional surface-to-surface radiation simulation including all channel walls of the test section. This approach uses locally measured wall temperatures to obtain local ambient temperatures that are relevant for a proper correction of the conductive heat flux.

Once the temperature and convective heat flux distributions on the test surface are obtained, the local adiabatic film cooling effectiveness

$$\eta_{\mathrm{aw}} = \frac{T_{\mathrm{hg}} - T_{\mathrm{aw}}}{T_{\mathrm{hg}} - T_{\mathrm{c}}} \tag{3}$$

and the isoenergetic heat transfer coefficients

$$h_{\mathrm{f}} = \frac{q_{\mathrm{conv}}}{(T_{\mathrm{aw}} - T_{\mathrm{w}})} \tag{4}$$

can be derived. Both definitions are based on the local adiabatic wall temperature T_{aw}, which represents the local cooling film temperature and is a priori unknown. A well-known method to obtain the unknown variables is the superposition approach of film cooling [11, 12]. It utilizes the linear relationship between the wall heat flux and the dimensionless wall temperature θ in the case of constant flow conditions. A formal derivation can be obtained by combining Eqs. (3) and (4), which leads to

$$\frac{q_{\mathrm{conv}}}{T_{\mathrm{hg}} - T_{\mathrm{w}}} = h_{\mathrm{f}}(1 - \eta_{\mathrm{aw}}\theta) \tag{5}$$

with

$$\theta = \frac{T_{\mathrm{hg}} - T_{\mathrm{c}}}{T_{\mathrm{hg}} - T_{\mathrm{w}}}.$$

All quantities in Eq. (5) except for h_{f} and η_{aw} are measured within one experiment. In order to obtain the values of these two variables, a second experiment needs

Table 1.
Experimental uncertainties

Quantity	Uncertainty
Main flow Reynolds number (Re_{hg})	<2%
Blowing ratio (M)	<3%
Discharge coefficient (CD)	<4%
Film cooling effectiveness (η_{aw})	<5%
Heat transfer coefficient (h_f)	<12%

to be conducted at different thermal boundary conditions. The only chance to alter the thermal boundary condition without changing the flow field is to alter the wall temperature T_w, i.e., to enhance the wall heat flux. The two test plates described earlier are used for the two experiments. One establishes nearly adiabatic conditions utilizing a low conductive material, whereas the other one induces a heat flux from the wall into the cooling film.

The discharge coefficient C_D is a dimensionless representation of the pressure losses of a film cooling ejection. It is defined as follows:

$$C_D = \frac{\dot{m}_{c,real}}{\dot{m}_{c,ideal}} = \frac{\dot{m}_{c,real}}{p_{1,t} \cdot \left(\frac{p_2}{p_{1,t}}\right)^{\frac{\gamma+1}{2\gamma}} \cdot A_c \cdot \sqrt{\frac{2\gamma}{(\gamma-1)\cdot R \cdot T_{1,t}} \cdot \left[\left(\frac{p_{1,t}}{p_2}\right)^{\frac{\gamma-1}{\gamma}} - 1\right]}}. \quad (7)$$

The ideal coolant mass flow in the denominator is derived from an isentropic expansion of the coolant from the stagnation pressure $p_{1,t}$, which is measured by a pressure tap in the coolant plenum directly upstream of the L1-region, to static pressure p_2 in the hot gas channel. The value of p_2 is measured by means of a pressure tap at midheight of the channel side wall at $x = 0$. Thus, p_2 depends only on the hot gas flow conditions. Local aerodynamic effects of the cooling ejection and the geometry variations have negligible influence on this pressure value.

The experimental uncertainties for the film cooling experiments are determined by the method of [13]. The values are listed in Table 1.

3. RESULTS

3.1 Discharge Coefficients

The measured discharge coefficients are plotted versus blowing ratio M for different ejection lip thicknesses (Fig. 5) and varying lip shape (Fig. 6), respectively. A general trend towards higher discharge coefficients with increasing blowing ratio can

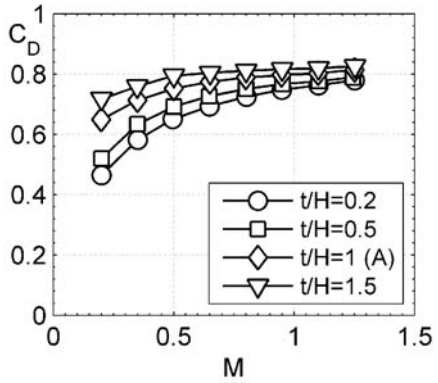

Fig. 5. Discharge coefficients for varying lip thickness versus pressure ratio.

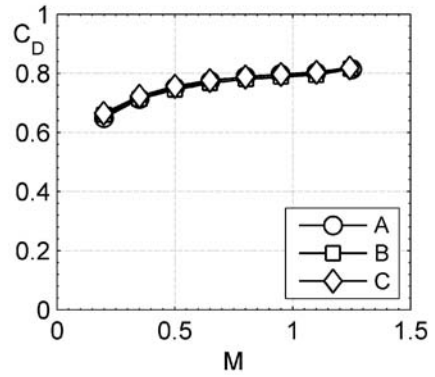

Fig. 6. Discharge coefficients for varying lip shape versus pressure ratio.

be observed in both diagrams. A discharge coefficient of $C_D \approx 0.8$ is obtained for the highest blowing ratio of $M = 1.25$. In case of the lip thickness variation a strong influence on the discharge coefficient is apparent. The level of discharge coefficients increases as the lip thickness is increased. This behavior is much more pronounced for lower blowing ratios, where differences between thickest and thinnest lip of up to 35% may occur. This can be explained by the local flow field immediately downstream of the ejection lip. The wake region grows with increasing lip thickness and hence local pressure is reduced. Unlike the static pressure p_2 in the main flow, the pressure inside the coolant cavity $p_{1,t}$ decreases as well, which consequently leads to higher C_D values. The lower the blowing ratio, the more the flow field approximates a backward facing step flow, which increases this wake effect even more.

In contrast to that, the discharge coefficients for the various lip shapes show no significant differences. All three configurations have the same pressure levels in the wake region. There doesn't seem to be any difference in the separation behavior despite the varying guidance of the flow along the ejection lip.

3.2 Adiabatic Film Cooling Effectiveness

Typical contour plots of local film cooling effectiveness downstream of the coolant ejection are shown in Fig. 7 demonstrating the qualitative effect of the ribs on the film cooling performance for two different lip thicknesses and three different blowing ratios. In the wake region of the ribs the mixing of the cooling film is increased due to higher turbulence levels within this region. Looking at the thin ejection lip (t/H = 0.2) this leads to lower film cooling effectiveness downstream of the ribs compared to the space in between the ribs. At an increased lip thickness (e.g., t/H = 1) an inverse effect can be observed at a blowing ratio of M = 0.8. Unsteady vortex shedding from the blunt ejection lip causes a drop of film cooling effectiveness between the ribs, whereas the wake region behind the ribs suppresses the vortex shedding and, therefore, stabilizes the cooling film. Only at the highest blowing ratio and for a lip thickness of t/H = 1 the wake region of the rib starts to dominate the mixing of the cooling film again, whereas the space in between the ribs shows the highest film cooling effectiveness.

For a more detailed discussion, the laterally averaged film cooling effectiveness along test surface is shown in Fig. 8 for different blowing ratios. Starting at a film cooling effectiveness of approximately unity, it begins to drop at x/H = 5. This is almost independent of the blowing ratio. Only the thin lip configurations retain a stable cooling film for a longer distance at higher blowing ratios. The decay of the effectiveness is smaller and the thinnest configuration still has a film cooling effectiveness of $\eta_{aw} \approx 0.9$ at x/H = 15, whereas the thickest configuration at the same location causes a drop down to $\eta_{aw} \approx 0.55$ at M = 0.8.

Since the decrease of the laterally averaged film cooling effectiveness occurs monotonously along the streamwise distance, a good comparison of the qualitative be-

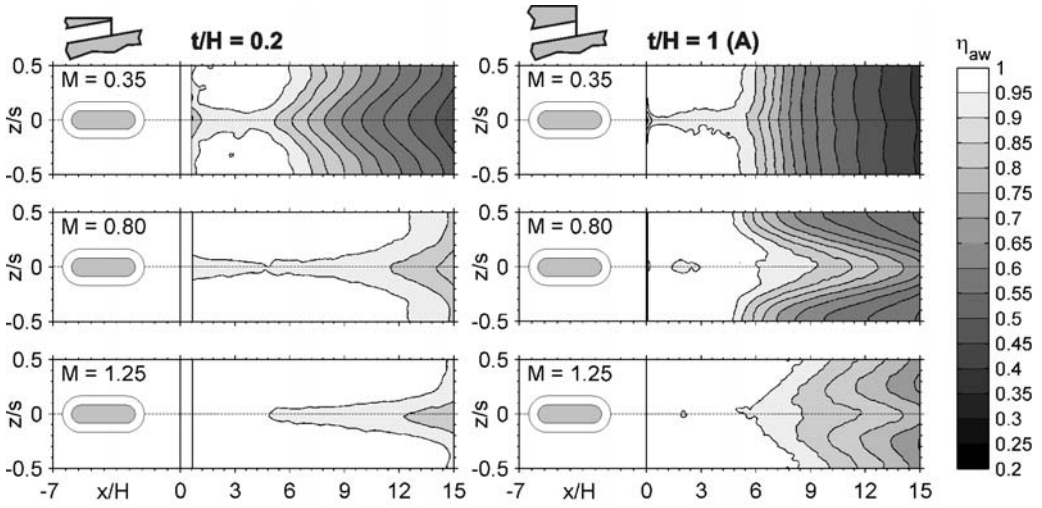

Fig. 7. Contours of local adiabatic film cooling effectiveness downstream of the ejection slot at different blowing ratios for two different lip thicknesses.

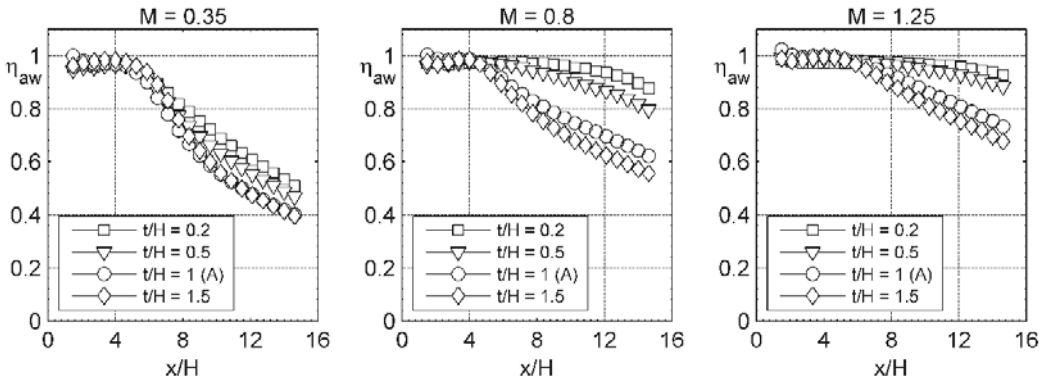

Fig. 8. Laterally averaged film cooling effectiveness for lip thickness variation.

havior can be obtained by plotting the laterally averaged values versus the measured blowing ratios at one representative streamwise position (see Fig. 9). This diagram reveals the strong influence of the ejection lip thickness on the cooling performance. In the case of the reference configuration (t/H = 1) the film cooling effectiveness increases with higher amount of cooling air. But this is only true for low blowing ratios. For blowing ratios of $0.65 < M < 0.95$ the cooling effectiveness decreases. The film cooling effectiveness recovers again for blowing ratios above M = 0.95. This behavior was already observed in [7] and can be attributed to the intensification of the vortex shedding at the ejection lip in this operating range. The effect is not visible in thin lipped geometries (t/H = 0.2; 0.5). These cases show monotonously increasing cooling performance with increasing blowing ratio over the whole measured range. The vortex-shedding phenomenon seems to play an inferior role in these configurations. Even at downstream position of x/H = 10 the thin lip configurations show an almost intact cooling film with an effectiveness well above η_{aw} = 0.9.

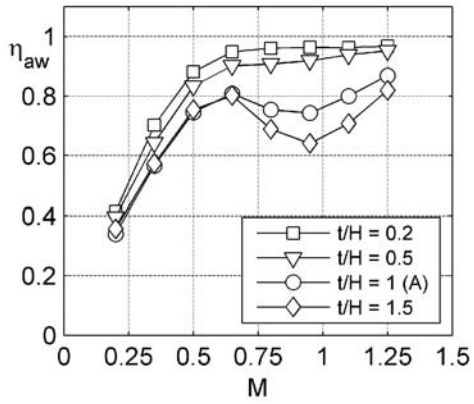

Fig. 9. Laterally averaged film cooling effectiveness for lip thickness variation vs. blowing ratio at x/H = 10.

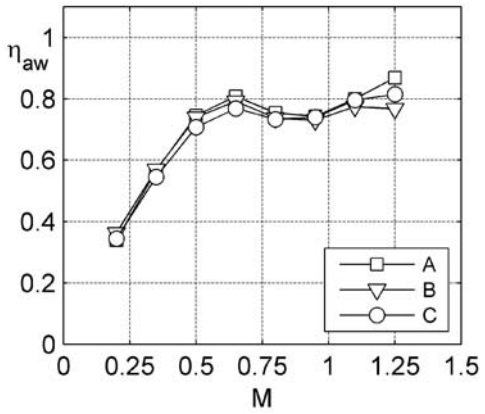

Fig. 10. Laterally averaged film cooling effectiveness for lip shape variation vs. blowing ratio at x/H = 10.

The test cases for the varied lip shape are discussed only briefly here, for the deviations from the reference case (t/H = 1 (A)) are only very marginal. However, an example of the results for these geometry variations is given in Fig. 10, where the laterally averaged film cooling effectiveness is plotted with the blowing ratio at x/H = 10. Except for the highest blowing ratio all three configurations show almost perfectly matching results, which are well within the precision range of the measurement technique. Hence, no significant effect of the lip shape can be observed. Only at M = 1.25 the reference case (A) shows the highest film cooling effectiveness followed by the fully rounded profile (C). The maximum difference between the investigated cases is approximately 13% at the highest blowing ratio. To conclude any physical effects for this blowing ratio might be hasty, since any possible effect is represented only by one operating point. Further investigations with higher blowing ratios are advisable to gain a deeper understanding of the effects occurring here.

3.3 Heat Transfer

The heat transfer coefficients shown in this section are normalized by a heat transfer correlation for a turbulent boundary layer flow on a flat plate according to [14]:

$$h_0 = 0.0287 \cdot \mathrm{Pr}^{-0.4} \cdot \mathrm{Re}_{\mathrm{hg},x}^{-0.2} \cdot \rho_{hg} \cdot c_{\mathrm{p,hg}} \cdot u_{\mathrm{hg}}. \tag{8}$$

The hot gas Reynolds number $\mathrm{Re}_{\mathrm{hg},x}$ is formed with the distance from the ejection slot. Figure 11 shows the local normalized heat transfer distributions for some representative cases. At first sight, a noticeable low level of heat transfer is visible in the near-slot region between the ribs. According to [7], this can be attributed to two effects. First, a separation bubble forms directly downstream of the slot, where the flow between the ribs behaves very similar to a 2D slot ejection. The second reason is the strong acceleration of the coolant in the convergent part of the coolant cavity and the

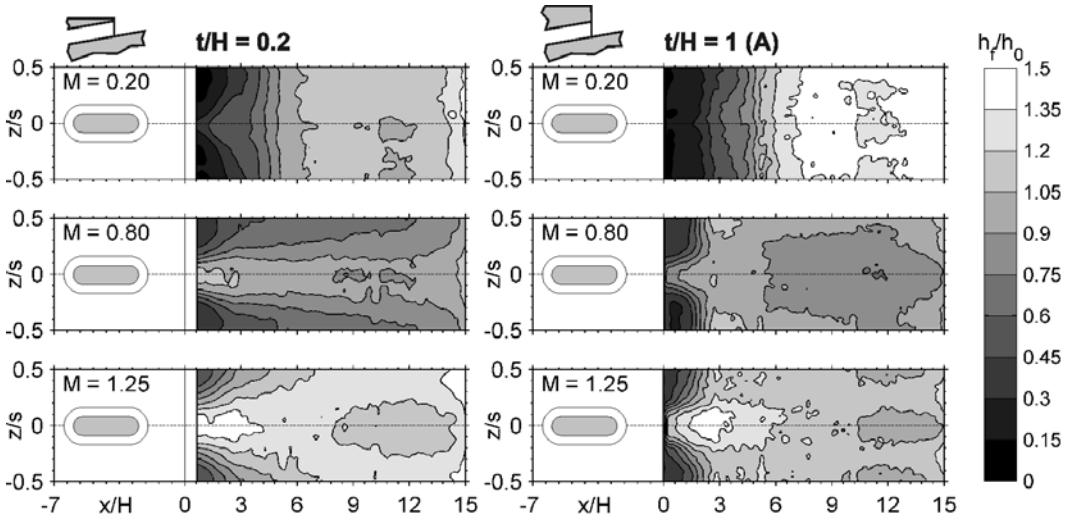

Fig. 11. Contours of local normalized heat transfer coefficient distributions at different blowing ratios for two different ejection lip thicknesses.

throat between the ribs. The strong acceleration causes a reduction of turbulence and might even lead to relaminarization of the coolant flow. This assumption is supported by internal heat transfer measurements that revealed relatively low internal heat transfer coefficients for this geometry, which can be expected to extend into the L3-region.

For low blowing ratios only small lateral differences are visible, which are localized in the immediate vicinity of the ejection lip. At a downstream distance of approximately three times the slot height, the lateral distribution becomes uniform. The very low momentum of the coolant leads to a flow field, which is very similar to a backward facing step flow. Downstream of the point, where reattachment would be expected ($x/H \approx 3$), a rapid increase in the heat transfer can be observed. The thicker ejection lip produces more turbulence, which results in a higher level of heat transfer farther downstream. The heat transfer along the L3-surface is mainly driven by the hot gas flow.

With an increasing blowing ratio ($M = 0.8$), the two compared configurations show completely different characteristics. In the case of the thin ejection lip the lateral distribution is very nonuniform. Reduced heat transfer is present in the regions between the ribs, whereas significantly increased heat transfer is found in the rib's wake region. The configuration with a thicker ejection lip ($t/H = 1$) shows a completely different behavior as it could already be observed with the film cooling effectiveness. The distribution in the rib's wake region is somewhat comparable to the thin-lipped geometry, whereas the region between the ribs is, again, strongly influenced by the unsteady vortex shedding from the ejection lip. This causes an increase of heat transfer coefficients between the ribs, especially in the vicinity of the slot at $x/H = 3$,

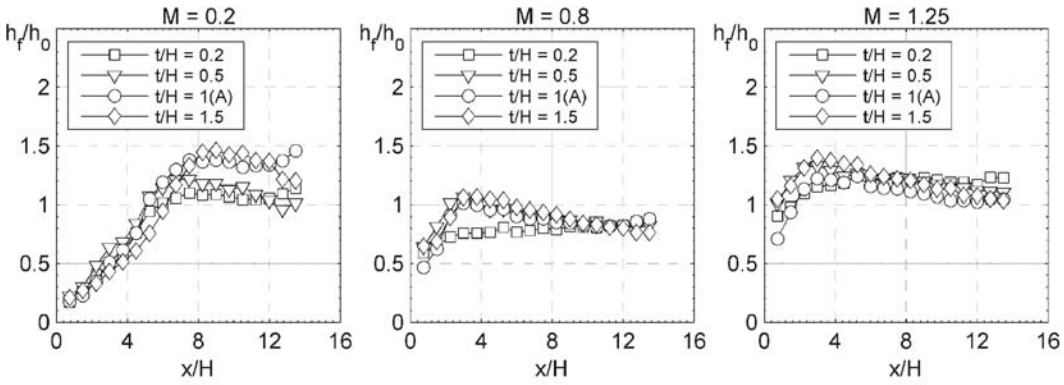

Fig. 12. Laterally averaged normalized heat transfer coefficients for lip thickness variation.

where the impact of the vortices on the L3-surface is strong. At the highest blowing ratio (M = 1.25) the wake flow of the ribs becomes dominant as can be seen from the local heat transfer coefficients of both, the thin lip geometry and the thick lip geometry.

The corresponding laterally averaged values of the heat transfer coefficients are shown in Fig. 12. There is a general trend towards higher heat transfer coefficients with increasing lip thickness. At M = 0.2, the lip thickness seems to significantly affect the heat transfer. In this case, the heat transfer coefficients increase from very low values near the ejection lip to values of h_f/h_0 = 1.5 further downstream for the thickest lip geometry. In the wake region close to the ejection lip, the low momentum of the coolant results in low heat transfer coefficients. In analogy to a backward-facing step, the hot gas flow is directed towards the L3-surface and, therefore, strongly increases the heat flux by distinct impingement. The result is a mixing region dominated by the hot gas flow with high heat transfer coefficients. The thicker the ejection lip, the stronger the impact on the heat transfer coefficients. At M = 0.8, where the most intensive vortex shedding was observed, the laterally averaged heat transfer coefficients show only small differences between the different lip thicknesses, except for the thinnest lip case. The effect of vortex shedding impact on the wall is marginal at this operating point. This results in a gradual rise of the heat transfer coefficients along the L3-region for t/H = 0.2. The difference diminishes further downstream, where the wall flow is more and more influenced by the hot gas.

At the highest blowing ratio of M = 1.25 the differences between the configurations is reduced. The overall level of heat transfer is increased compared to M = 0.8, which can be ascribed to the high velocity of the coolant ejected. The momentum of the coolant flow is approximately 2.5 times higher than the momentum of the main flow. This wall jet results in a reduced boundary layer thickness along the wall and, therefore, increased heat transfer compared to the lower blowing ratios.

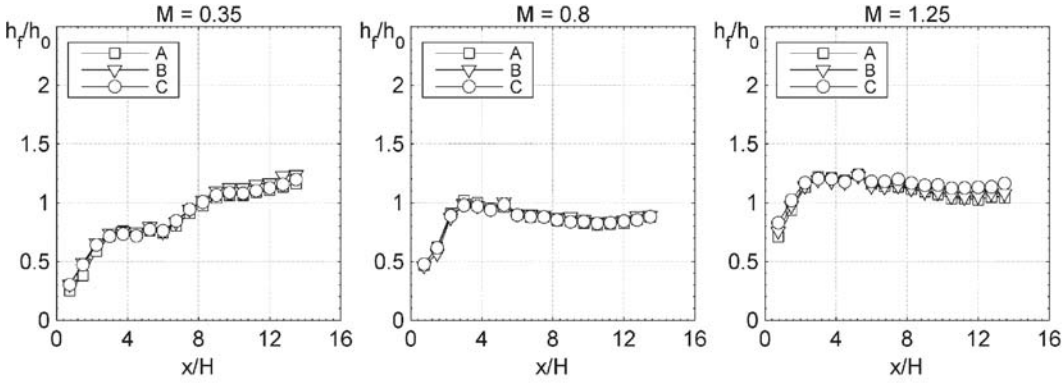

Fig. 13. Laterally averaged normalized heat transfer coefficients for lip shape variation.

The comparison of the lip shape variation cases reveals, again, no significant differences, as can be seen in Fig. 13. The general trends of the heat transfer coefficients with an increasing surface distance are the same as shown and discussed in the previous paragraph for various lip thicknesses.

4. CONCLUSIONS

Experimental data on the variation of the ejection lip thickness and shape of a trailing edge have been presented. In summary, it can be stated that the cooling performance is predominantly determined by the blowing ratio. Moreover, the variation of the ejection lip thickness has a pronounced effect on the mixing process of the cooling film, as well as on the discharge coefficients. Heat transfer, however, is only moderately affected by the various geometric modifications, with a tendency towards increased heat transfer coefficients with thicker lips. In the case of a trailing edge film cooling application, where the purpose of the cooling film is to remove heat from the suction surface, higher heat transfer coefficients would be appreciated.

The variation of the ejection lip shape has no noticeable effects on the discharge coefficients. In terms of cooling performance it can be the concluded that the investigated variations of the ejection lip shape have a negligible effect on both, the film cooling effectiveness and the heat transfer coefficients. Thus, design imperfections or deviations that may result from manufacturing or wear, as they were generically investigated in this study, can be considered to be irrelevant for the cooling performance of the investigated configuration with internal ribs.

ACKNOWLEDGMENTS

This study was partly funded by the European Union through grant of the European research project "Aerothermal Investigations of Turbine Endwalls and Blades 2"

(AITEB-2) under Contract No. AST4-CT-2005-516113. The authors wish to express their gratitude to the partners involved in the program for the permission to publish this paper.

NOMENCLATURE

b_r	rib width, mm
C_D	discharge coefficient
h_f	isoenergetic heat transfer coefficient, W/(m·K)
H	slot height, mm
L	characteristic length
M	blowing ratio
$p_{1,t}$	total pressure in the coolant cavity, Pa
p_2	static pressure at slot exit, Pa
P_{el}	electric power, W
s	pitch, mm
t	ejection lip thickness, mm
Tu	turbulence intensity

Greek symbols

δ_{99}	boundary layer thickness, mm
ε	emissivity
η_{aw}	adiabatic film cooling effectiveness
θ	dimensionless wall temperature
π	pressure ratio

Subscripts

0	reference case
ad	adiabatic
c	coolant
conv	convective
hg	hot gas
max	maximum
o	overhang
r1	rib in the L1-region
r2	rib in the L2-region
t	total value
w	wall
x	in stream wise direction.

REFERENCES

1. Kacker, S. C. and Whitelaw, J. H. An experimental investigation of the influence of slot-lip thickness on the impervious wall effectiveness of the uniform-

density, two dimensional wall jet, *Int. J. Heat Mass Transfer*, 1969, Vol. 12, pp. 1196–1201.
2. Sivasegaram, S. and Whitelaw, J. H. Film cooling slots: the importance of lip thickness and injection angle, *J. Mech. Eng. Sci*., 1969, Vol. 2(1), pp. 22–27.
3. Taslim, M. E., Spring, S. D., and Mehlmann, B. P. An Experimental Investigation of Film Cooling Effectiveness for Slots of Various Exit Geometries, AIAA Paper No. AIAA-90-2266, 1990.
4. Holloway, D. S., Leylek, J. H., and Buck, F. A. Pressure Side Bleed Film Cooling. Part 2: Unsteady Framework for Experimental and Computational Results, ASME Paper No. GT-2002-30472, 2002.
5. Martini, P., Schulz, A., Whitney, C. F., and Lutum, E. Experimental and numerical investigation of trailing edge film cooling downstream of a slot with internal rib arrays. In: *Proc. Inst. Mech. Eng*., Part A, 2003, Vol. 217, pp. 393–401.
6. Martini, P. and Schulz, A. Experimental and numerical investigation of trailing edge film cooling by circular wall jets ejected from a slot with internal rib arrays, *J. Turbomachinery*, 2004, Vol. 126, pp. 229–236.
7. Martini, P., Schulz, A., and Bauer, H.-J. Film cooling effectiveness and heat transfer on the trailing edge cut-back of gas turbine airfoils with various internal cooling designs, *J. Turbomachinery*, 2006, Vol. 128, pp. 196–205.
8. Martini, P., Schulz, A., Bauer, H.-J., and Whitney, C. F. Detached eddy simulation of film cooling performance on the trailing edge cut-back of gas turbine airfoils, *ASME J. Turbomachinery*, 2006, Vol. 128, pp. 292–299.
9. Joo, J. and Durbin, P. Simulation of turbine blade trailing edge cooling, *J. Fluids Eng*., 2009, Vol. 131, pp. 021102-1–021102-14.
10. Ochs, M., Horbach, T., Schulz, A., Koch, R., and Bauer, H.-J. Novel calibration method for an infrared thermography system applied to heat transfer experiments, *Meas. Sci. Technol*., 2009, Vol. 20(7), 075103.
11. Gritsch, M., Baldauf, S., Martiny, M., Schulz, A., and Wittig, S. The Superposition Approach to Local Heat Transfer Coefficients in High Density Ratio Film Cooling Flows, ASME Paper No. 99-GT-168, 1999.
12. Choe, H., Kays, W. M., and Moffat, R. J. The superposition Approach to Film-Cooling, ASME Paper No. 74-WA/HT-27, 1974.
13. Kline, S. J. and McClintock, F. A. Describing uncertainties in single sample experiments, *Mech. Eng. (Am. Soc. Mech. Eng.)*, 1953, Vol. 75, pp. 3–8.
14. Kays, W. M., Crawford, M. E., and Weigand, B. *Convective Heat and Mass Transfer*, McGraw-Hill International Editions, Mechanical Engineering Series, ISBN 978-0072990737, 2004.

□◆◆◆□

Heat Transfer Research, 2010, Vol. 41, No. 8

An Experimental Study of Airfoil and Endwall Heat Transfer on a Linear Turbine Blade Cascade — Secondary Flow and Surface Roughness Effects

MARCO LORENZ,* ACHMED SCHULZ, and HANS-JOERG BAUER

Institut fuer Thermische Stroemungsmaschinen, Karlsruhe Institute of Technology (KIT), 76131 Karlsruhe, Germany

The present study is part of a comprehensive heat transfer analysis on a highly loaded turbine blade and endwall with varying surface roughness. In this paper, a smooth airfoil with an endwall of varying surface roughness is considered in order to investigate secondary flow and surface roughness effects on airfoil and endwall heat transfer. The measurements have been conducted in a linear cascade with low pressure blades at several freestream turbulence levels (Tu_1 = 1.4% to 10.1%) and varying inlet Reynolds numbers ($Re_{1,c}$ = 50,000 to 250,000). Aerodynamic measurements have been carried out on the airfoil at midspan and complemented by oil paint visualization on airfoil and platform. Heat transfer on both the full-span suction and pressure surfaces of the airfoil and endwall is shown for smooth surfaces. Moreover, rough endwall surfaces are compared to the smooth reference case showing a maximum increase of local heat transfer of up to 240% due to surface roughness.

* * *

Keywords: turbine airfoil, platform, horseshoe vortex, turbulence, surface roughness

1. INTRODUCTION

In modern gas turbines high thermodynamic efficiency is reached by increasing turbine inlet temperature, which is far beyond the material's melting point and, thus, requires sophisticated cooling concepts. In order to predict the lifetime of turbine components under such severe operating conditions and to optimize the cooling, an

*Address all correspondence to Marco Lorenz E-mail: Marco.Lorenz@kit.edu

ISSN1064-2285

exact knowledge of surface heat transfer in the turbine is necessary. Heat transfer is affected by various factors, like pressure distribution, wakes, surface curvature, freestream turbulence, secondary flow effects, and surface roughness. In contrast to the first five factors the surface roughness is not constant during the lifetime of gas turbines but changes due to erosion, corrosion or particle deposition.

Extensive investigation of heat transfer at midspan of airfoils has been made by Schulz [1] and Dullenkopf et al. [2], who observed a strong influence of freestream turbulence on heat transfer especially on the onset of laminar–turbulent transition on the suction side. Moreover, they showed that heat transfer is increased by freestream turbulence in highly accelerated laminar boundary layers appearing at the suction side leading edge and on the pressure side. These experimental results were part of the database used by Mayle [3] who developed a correlation for the onset of laminar–turbulent transition, as well as a model accounting for the influence of freestream turbulence on accelerated laminar boundary layer heat transfer [4, 5]. Schiele et al. [6] numerically designed a turbine airfoil with minimum overall external heat transfer and confirmed the strong influence of freestream turbulence on laminar–turbulent transition by additional measurements. Bons and McClain [7] show flat plate heat transfer measurements of real turbine roughness. Stripf et al. [8] systematically investigated surface roughness effects on midspan heat transfer which led to a further correlation describing the strong effect of surface roughness on laminar–turbulent transition and turbulent boundary layer heat transfer on rough surfaces [9].

Since in modern gas turbines the endwall region becomes more and more thermally loaded, an increasing focus lies on airfoil heat transfer in the close vicinity of the endwall and on the endwall itself, where secondary flows dominate the heat transfer behavior. A comprehensive review of early investigations of those until 1985 is given by Sieverding [10]. A continuation of this work including more recent findings can be found in [11]. Detailed aerodynamic measurements in a linear turbine blade cascade have been performed by Langston et al. [12]. Figure 1 shows the summary

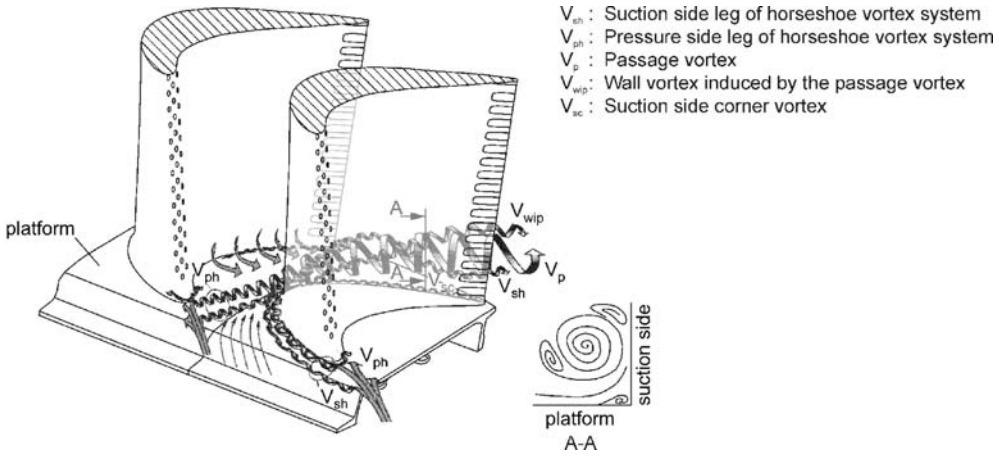

Fig. 1. Vortex pattern of Wang et al. [13].

of the three dimensional vortex system given by Wang et al. [13]. Chen and Goldstein [14] and Goldstein et al. [15] used the analogy between heat and mass transfer performing measurements using the naphthalene sublimation technique, which gave a high-resolution picture of convective transport on the surface of a turbine blade. The measurements revealed a remarkable heat transfer augmentation due to secondary flows on the suction side, which was attributed to four major vortices: the suction side horseshoe vortex V_{sh}, the passage vortex V_p, a suction side corner vortex V_{sc}, and a new vortex V_{wip} which is induced by the passage vortex. Detailed external heat transfer measurements on a smooth turbine blade and endwall by Graziani et al. [16] using thermocouples show strong secondary flow effects on airfoil and endwall heat transfer and a strong influence of platform boundary layer thickness. Blair [17] investigates airfoil and platform heat transfer for a smooth reference case in comparison to a roughened surface and reports an increase in heat transfer of up to 40% due to surface roughness. Further work by Stripf et al. [18] systematically examines different surface roughness and its effect on heat transfer on an airfoil close to the endwall.

The present experimental study is part of a comprehensive heat transfer analysis on a highly loaded low-pressure turbine blade and platform with varying roughness. Whereas a first publication [19] concentrated on midspan heat transfer of a smooth airfoil, in this paper the full-span heat transfer distribution on the blade and on its platform will be analyzed. Measurements are conducted at varying freestream turbulence and different inlet Reynolds numbers. Furthermore, a variation of platform surface roughness and its effect on external heat transfer will be shown.

2. EXPERIMENTAL SETUP AND MEASURING TECHNIQUE

2.1 Test Facility

The measurements are conducted on a highly loaded linear turbine cascade in a hot wind tunnel as shown in Fig. 2. The compressed air is heated up to 350 K by an electric heater. After passing a settling chamber and a honeycomb flow straightener, the air is guided through a nozzle into the test section with a rectangular cross section (100-mm wide and 250-mm high).

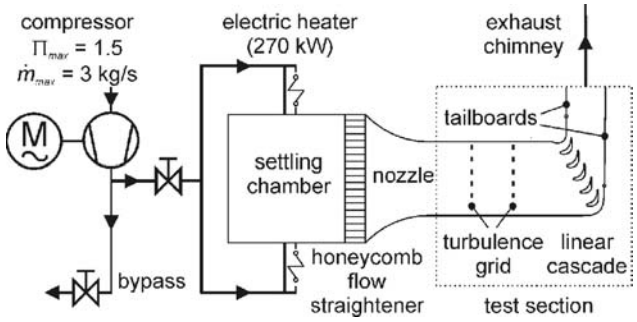

Fig. 2. Schematic view of the test facility.

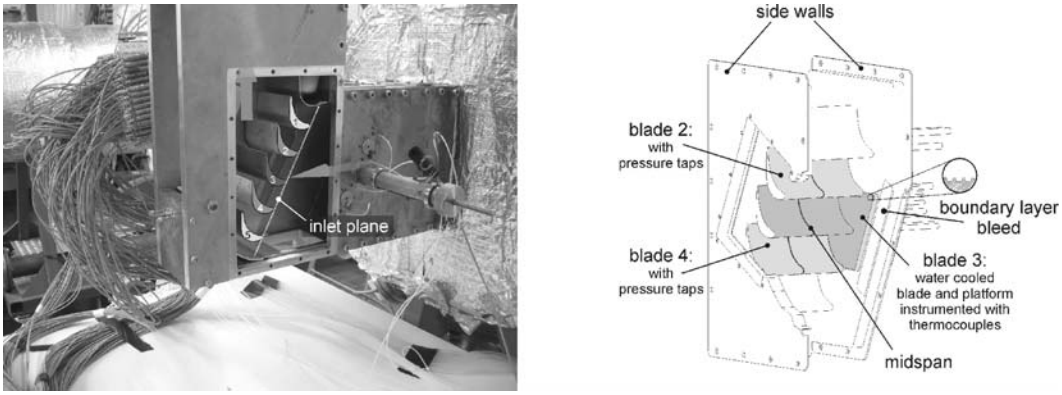

Fig. 3. Test facility (left) and cascade with instrumented airfoils (right).

The cascade consists of five untwisted turbine blades of which the inner three blades are instrumented as indicated in Fig. 3. Blades 2 and 4 are equipped with pressure taps for measuring the pressure distribution. These pressure taps are staggered in a band of ±10 mm around midspan in such a manner that a possible effect of one pressure tap on the boundary layer flow does not influence the measurement on a pressure tap further downstream on the airfoil. Blade 3 consists of a water cooled blade and platform and is instrumented for heat transfer measurements.

The upper and the lower boundaries of the test section are contoured according to streamlines and lead to adjustable tailboards which ensure a periodic flow through the cascade. In order to tune the tailboards and assure periodicity the pressure distributions on blades 2 and 4 at midspan are measured and matched.

Two different turbulence grids with rectangular bars can be placed at two locations either 345 mm (Position I) or 205 mm (Position II) upstream of the leading edge of blade 3 in order to generate different freestream turbulence levels. Thus, the turbulence intensity at the cascade inlet plane Tu_1 can be varied from 1.4 % (without grid) to 10.1%. The turbulence intensity is measured at eleven locations downstream of each grid by means of hot wire constant temperature anemometry, and the turbulent dissipation length scale L_ε is determined from the decay of turbulence using simplified k–ε transport equations according to [18, 20]. The values of Tu_1 and $L_{\varepsilon,1}$ at the cascade entry summarized in Table 1 are found to be fairly constant for varying inlet Reynolds numbers $Re_{1,c}$. Furthermore, the turbulent dissipation length scale determined in this manner matches very well additional measurements of the turbulent power spectrum that are conducted downstream of the turbulence grids and represent the basis for the turbulent length scale data with no grid installed. Since the turbulence decay is negligibly small in this case, determination of $L_{\varepsilon,1}$ is not possible in the above-described manner.

The wall upstream of the platform of blade 3 is thermally insulated from the environment and can be considered as adiabatic. The cooled platform is also insulated

Table 1.
Test parameters

Grid	Position	$Re_{1,c}$, 10^5	Tu_1 %	$L_{\varepsilon,1}$, mm
–	–	0.5 1.0 1.5 2.0 2.5	1.4	37
1	II	0.5 1.0 1.5 2.0 2.5	4.2	7.8
2	I	0.5 1.0 1.5 2.0 2.5	7.0	22.4
2	II	0.5 1.0 1.5 2.0 2.5	10.1	16.5

from the surrounding hot walls. The aerodynamic boundary layer developing on the side wall has been measured at the starting point of the thermal boundary layer at $x/c_{ax} = -0.38$ (see, e.g., Fig. 6 for coordinate system) by means of hot wire constant temperature anemometry. In all cases given in Table 1 the aerodynamic boundary layer was turbulent and its displacement thickness δ_1 varied in a range from 0.3 to 1.1 mm depending on inlet Reynolds number and turbulence grid configuration. In order to investigate the influence of boundary layer thickness on platform heat transfer, a boundary layer bleed is integrated into the adiabatic wall upstream of the cooled platform.

2.2 Heat Transfer Measurement Technique

For the heat transfer measurements smooth or rough metal foils are glued on the surface of an instrumented airfoil using a highly heat conductive adhesive and a vacuum bagging technique formerly described in [8] providing a good reproducibility of the bonding procedure. Thus, heat transfer can be measured for both smooth and rough surfaces.

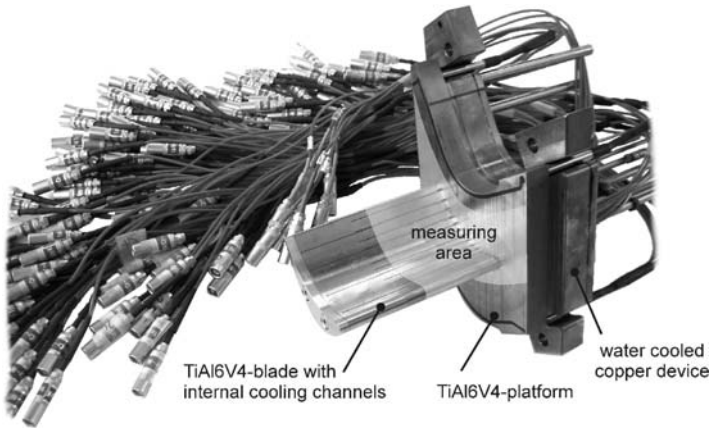

Fig. 4. Water-cooled blade and platform for heat transfer measurements.

The heat transfer measuring airfoil and its platform (Fig. 4) are made of titanium alloy ($TiAl_6V_4$) with thermal conductivity of $k \approx 7.0$ W/(m·K). The airfoil is convectively water-cooled by 8 cylindrical cooling channels, which results in an average airfoil surface temperature of 289–326 K depending on the heat transfer level. Furthermore, heat flux on the airfoil's platform can also be induced by a water-cooled copper device that is in direct contact to the platform's backside, leading to a surface temperature between 295 and 337 K. The temperature distribution all over the airfoil, as well as on the platform, is measured by 134 thermocouples, with a diameter of 0.25 mm, embedded in grooves on the surface. The midspan of the blade is equipped with 35 thermocouples providing a very good spatial resolution. Figures 5 and 6 show the thermocouples' location on the blade and platform, assuming a symmetric distribution of heat transfer on the blade and periodic heat transfer on the platform. The airfoil material was selected as a result of a one-dimensional error analysis following the method of Kline and McClintock [21] and described in detail by Stripf [22] taking into account the uncertainties of the materials' thermal conductivities, the

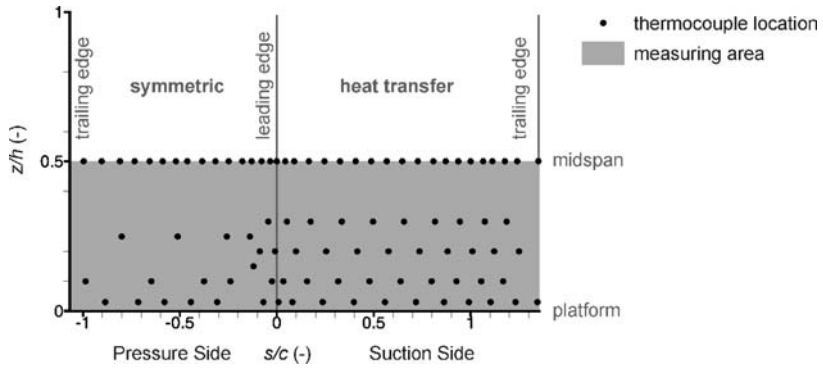

Fig. 5. Thermocouple locations on the blade.

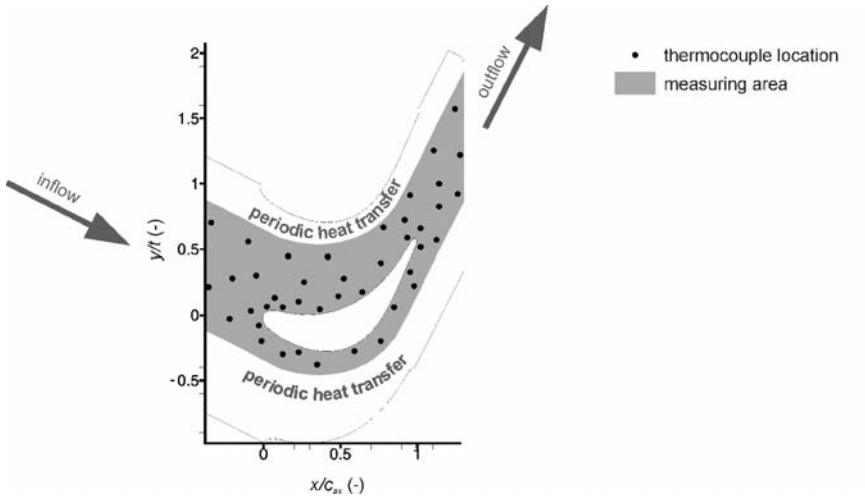

Fig. 6. Thermocouple locations on the platform.

thermal transmittance of the adhesive joint, the positioning of the thermocouples, the heat transfer coefficients in the cooling channels, and the temperature measurement. Thus, errors for the heat transfer coefficients were estimated below 10% for most of the blade and platform surface and up to 15% on the airfoil near the leading and the trailing edge, where the distance between the thermocouples and the cooling channels is relatively small and positioning uncertainties have a noticeable effect.

For determining heat transfer coefficients the method described by Turner [23] and Wittig et al. [24] is used, which was adapted by Stripf et al. [8] in order to account for the thermocouple grooves, adhesive joint, and metal foil. For each cooling channel the water temperature at the inlet and the outlet, as well as the coolant mass flow are measured. With a correlation for a turbulent flow in pipes the heat transfer coefficient in the cooling channels can be determined using the mass flow and the water temperature that is linearly interpolated between inlet and outlet values. As the platform is in direct contact with the water-cooled copper device, the temperature on its backside is extremely homogenous (due to the high thermal conductivity of copper) and can be measured with only 6 additional thermocouples. The temperature distribution around the airfoil and the platform underneath the metal foil and adhesive joint is measured by 134 thermocouples, and the total gas temperature at the cascade inlet is determined using a thermocouple in a Pitot probe.

As the temperature distribution is not measured directly on the surface but underneath the metal foil, the following iterative procedure is taken to determine the heat transfer distribution $h(s, z)$ on the airfoil and $h(x, y)$ on the platform, respectively:

1. A starting heat transfer distribution h has to be given on the outer surface, e.g., a constant value.
2. With a finite element method the equation for heat conduction is solved within the airfoil and the platform. The estimated heat transfer distribution h in com-

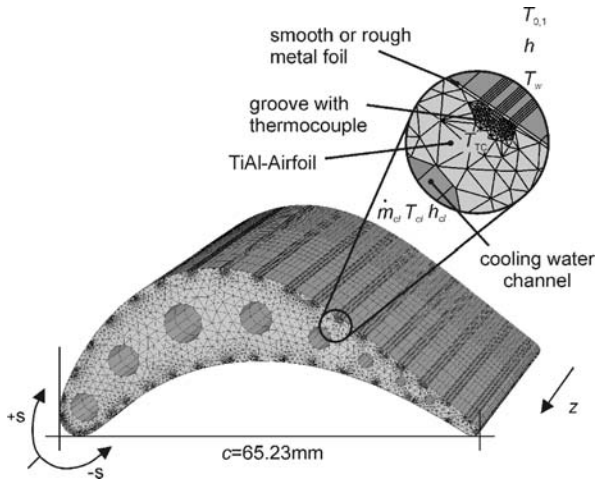

Fig. 7. Finite element mesh.

bination with the total temperature of the hot gas $T_{0,1}$ is used as boundary condition on the outer surface of the blade. In the cooling channels the mean water temperature together with the coolant heat transfer coefficients is taken as boundary condition, whereas the measured, uniform temperature is known on the backside of the platform. It is sufficient to model only half of the airfoil since the flow field and the heat transfer distribution in the midspan region is two-dimensional and, hence, the heat flux normal to the midspan plane can be neglected. Additional measurements show no influence of the platform cooling on the midspan temperature distribution. Thus, the midspan plane is taken as symmetry plane. For simplicity Fig. 7 only shows the airfoil part of the finite element model. The platform is modeled accordingly assuming periodic heat transfer. Not only the airfoil and platform material but also the thermocouples and the metal foil including the adhesive joint are resolved by the finite element mesh.

3. The temperatures measured at all thermocouple locations are compared to the values calculated in step 2. If they differ, the heat transfer distribution h is adjusted appropriately.
4. If the difference between measured and calculated values in step 3 is not sufficiently small, a new temperature field is calculated in step 2 using the adjusted heat transfer distribution. Otherwise the iteration is stopped. Usually, a converged solution is reached after 10 to 15 iterations.

2.3 Surface Roughness

The rough metal foils glued on the platform are produced in a photolithographic process formerly described by Stripf et al. [25] copying a pattern of a mask on a metal foil coated with photoresist. The roughness element base diameter d and the distances t_1 and t_2 are determined in this first step. Figure 8 shows the geometry of

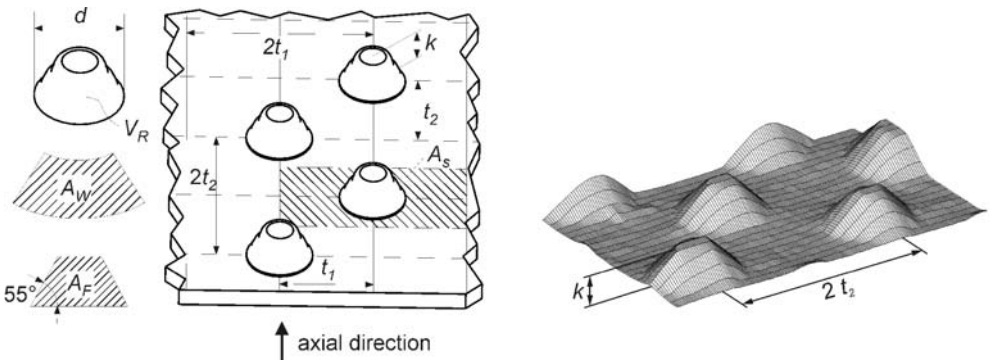

Fig. 8. Surface roughness (left: schematic drawing, right: perthometer scan).

the deterministic surface roughness investigated. The following wet etching process creates the three-dimensional structure seen in Fig. 8, resulting in truncated cones. The roughness element height k is controlled by the etching time. Besides the rough metal foil, a smooth one is investigated, too, serving as a reference. For fully rough surfaces Waigh and Kind [26] give a correlation to characterize the aerodynamic effects of regular three-dimensional roughness in terms of the equivalent sand grain roughness $k_{s,eq}$. Defining the roughness density parameter Λ_R they distinguish between a dense regime with closely packed roughness elements and a sparse regime with sparely distributed roughness elements. Hereby, surfaces with roughness density parameters of $\Lambda_R \approx 6$ result in maximum equivalent sand grain roughness. Such surfaces have been chosen to investigate the effect on heat transfer in this work. Table 2 gives an overview of the roughness geometry and further surface roughness parameters such as the surface increase $\Delta A/A_S$, the meltdown height h_m as well as the arithmetic average roughness height R_a. As the experiments have been conducted with a geometrically scaled airfoil, the roughness parameters describing the roughness height must always be considered in comparison to the airfoil size, e.g., the chord length c. The relative roughness height k/c of the investigated rough surfaces lies between values of $0.54 \cdot 10^{-3}$ for r40 and $1.23 \cdot 10^{-3}$ for r80. The thermal conductivity of the roughness elements depends on the choice of the foil material and is $k \approx 33$ W/(m·K).

Table 2.
Surface roughness parameters

Roughness type	k, µm	d, µm	t_1, µm	t_2, µm	Λ_R, (–)	$k_{s,eq}$, µm	$\Delta A/A_S$, %	h_m, µm	R_a, µm	k/c, 10^{-3}
smooth	hydraulically smooth									
r40	35	100	110	110	5.2	119	17.9	6.7	9.5	0.54
r80	80	200	220	220	5.7	289	19.5	14.1	20.0	1.23

3. EXPERIMENTAL RESULTS

Before showing airfoil and platform heat transfer data some aerodynamic characteristics of the airfoil have to be discussed. Figure 9 reveals the Mach number distribution of the airfoil at midspan, which is obtained from surface pressure measurements as follows:

$$M_{is} = \sqrt{\frac{2}{\gamma - 1}\left[\left(\frac{p_{stat}(s)}{p_{0,1}}\right)^{\frac{1-\gamma}{\gamma}} - 1\right]} \tag{1}$$

with $p_{stat}(s)$ representing the local static pressures measured by pressure taps and $p_{0,1}$ as total inlet pressure. As can be clearly seen, the Mach number distribution of blades 2 and 4 match very well showing an excellent periodicity of the flow through the cascade. On the pressure side the flow is strongly decelerated from 10% to about 30% to 40% of the chord depending on the inlet Reynolds number $Re_{1,c}$, which results in negative acceleration parameters:

$$K = \frac{\nu}{u_\infty^{\,2}} \frac{du_\infty}{ds}. \tag{2}$$

In this region, boundary layer separation can be expected. Further downstream, there follows a region of high acceleration with K exceeding the minimum value for relaminarization ($K = 3.0 \cdot 10^{-6}$, according to [27]. On the suction side the flow is slightly decelerated at 10% chord before reaching its maximum velocity at about 70% of the chord. Towards the trailing edge a large separation bubble appears for low inlet Reynolds numbers as can be clearly seen in the acceleration parameter distribution in Fig. 9.

However, the separation bubble is still present for relatively high inlet Reynolds numbers at low turbulence intensity as shown by oil paint visualizations in Fig. 10.

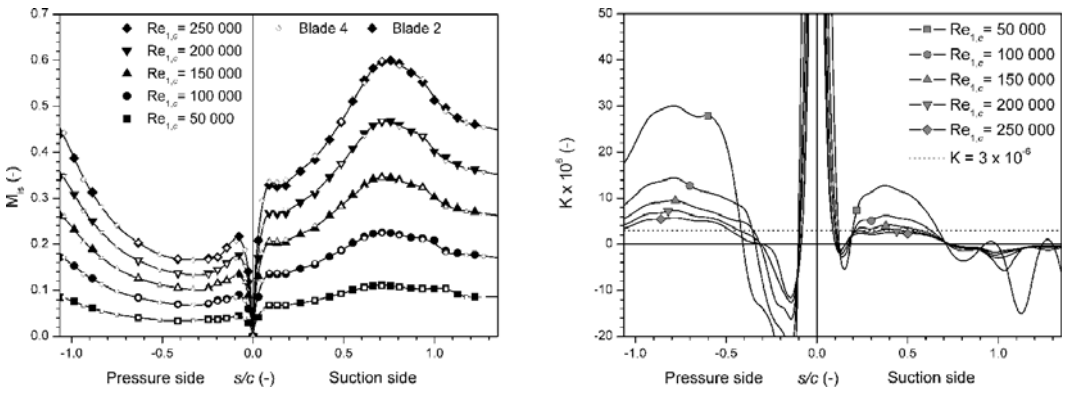

Fig. 9. Mach number distribution and acceleration parameter at $Tu_1 = 1.4\%$.

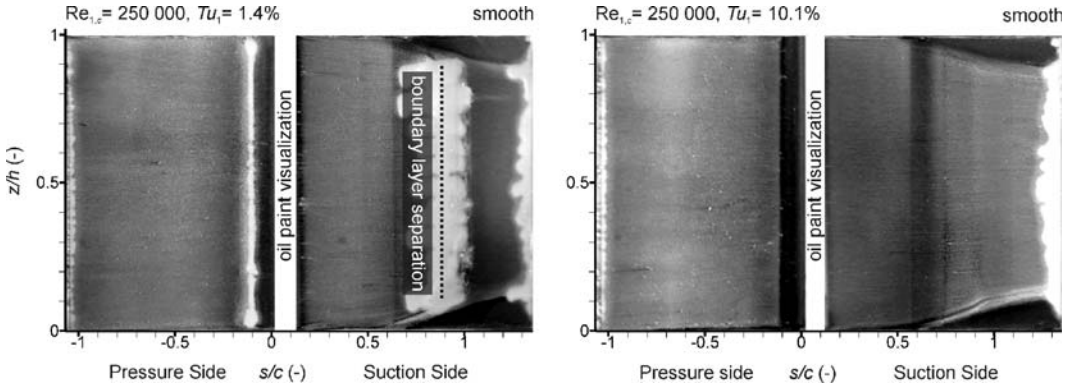

Fig. 10. Oil paint visualization on airfoil at different turbulence intensities.

External heat transfer for both airfoil and endwall is shown in terms of Nusselt number distributions. The Nusselt number is determined using the local heat transfer coefficient h, the airfoil chord length c, and a constant thermal conductivity for air k = 0.03 W/(m·K) as indicated by Eq. (3). The heat transfer coefficient h refers to the temperature difference between total inlet temperature $T_{0,1}$ and wall temperature T_w:

$$\mathrm{Nu} = \frac{h \cdot c}{k} = \frac{\dot{q}}{T_{0,1} - T_w} \frac{c}{k} \quad . \tag{3}$$

3.1 Airfoil Heat Transfer

As can be observed in Fig. 11, the inlet Reynolds number has a major influence on the level of heat transfer. Furthermore, turbulence intensity has a large impact on heat transfer in the stagnation point, on the pressure side as well as on the suction side of the airfoil. Heat transfer on the pressure side is mainly affected by turbulence intensity at about 10% of the chord where boundary layer separation takes place and reattachment follows much sooner at high turbulence levels. Moreover, a strong influence of freestream turbulence on stagnation point heat transfer can be observed leading to an augmentation in heat transfer for increasing turbulence intensity. As Fig. 11 reveals, only at high Reynolds numbers suction side heat transfer is affected by freestream turbulence: For low turbulence levels a laminar boundary layer develops downstream of the stagnation point until boundary layer separation takes place at 90% of the chord followed by turbulent reattachment connected with increased (turbulent) heat transfer downstream of the separation bubble. For high turbulence levels boundary layer transition takes place upstream of the potential separation region leading to transitional boundary layers (with increased heat transfer) and resulting in smaller separation bubbles or a complete suppression of those (see Fig. 10). A detailed discussion on heat transfer at midspan is given in [19].

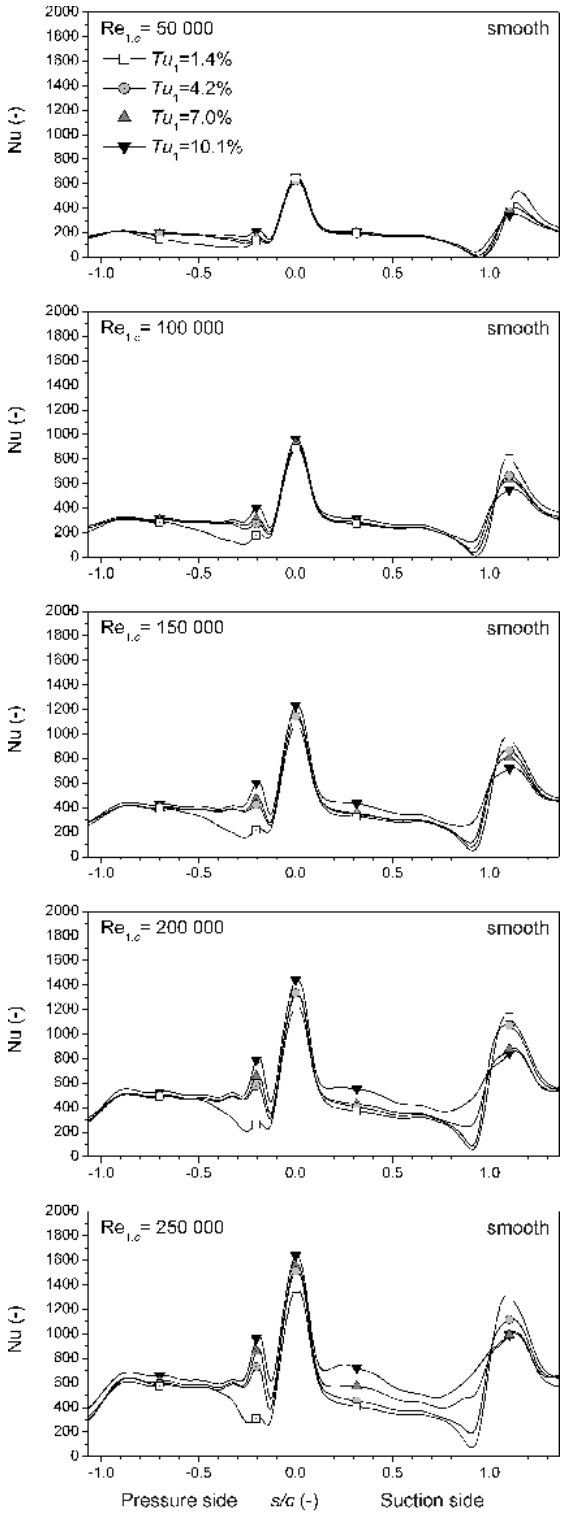

Fig. 11. Heat transfer distribution for a smooth blade at midspan at varying Reynolds number and freestream turbulence.

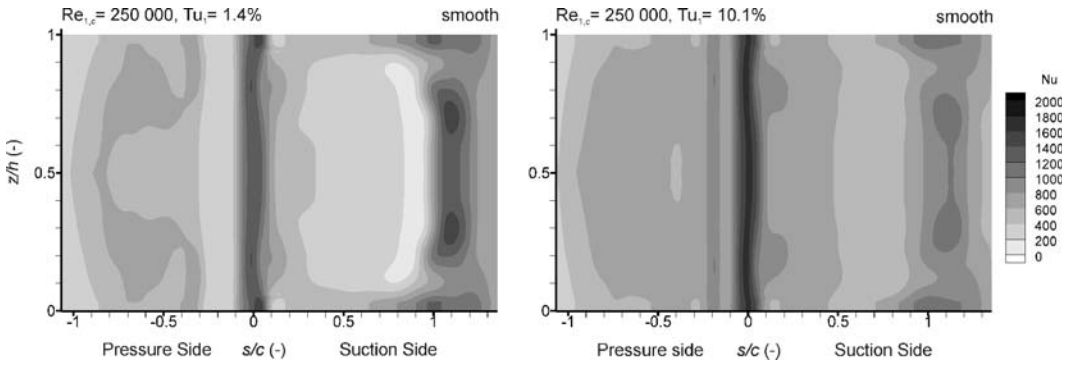

Fig. 12. Full-span heat transfer distribution for a smooth blade at different freestream turbulence.

Figure 12 additionally reveals the influence of secondary flow effects on airfoil heat transfer near the platform. Whereas secondary flow hardly affects heat transfer on the pressure side, the effects of the passage vortex moving on the suction side from the platform towards midspan can be clearly seen. The passage vortex also leads to a deflection of the suction side horseshoe vortex into the same direction causing locally increased heat transfer near the endwall (compare Fig. 1 and Fig. 11).

3.1 Endwall Heat Transfer

In contrast to airfoil heat transfer the Nusselt number distribution on the endwall does not depend as strongly on the level of freestream turbulence (see Fig. 13). In the measuring setup an adiabatic wall upstream of the cooled platform is provided ensuring a well defined start of the thermal boundary layer at the left boundary of the

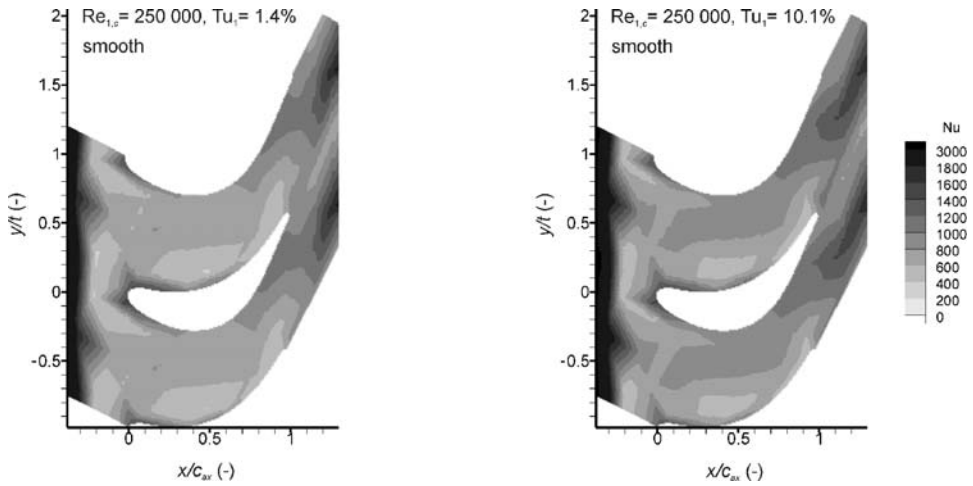

Fig. 13. Heat transfer distribution for a smooth platform at different freestream turbulence.

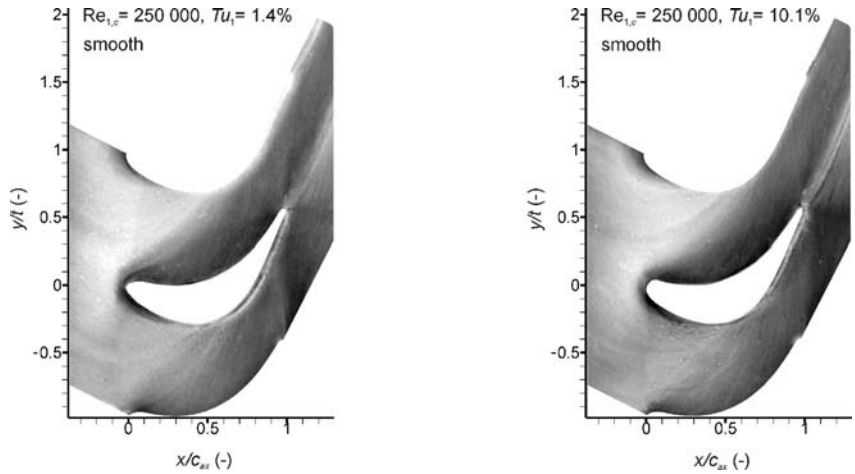

Fig. 14. Oil paint visualization on platform at different turbulence intensities.

endwall at $x/c_{ax} = -0.38$. This leads to a comparably high heat transfer in this region (compare with [28]). Mainly it can be observed that heat transfer increases as the flow accelerates from the left to the right because of the decreasing cross section through the passage. Regarding oil paint visualizations on the platform in Fig. 14 (dark color represents areas with high wall shear stress, bright color those with lower one), and comparing them to heat transfer measurements in Fig. 13, it may be observed that heat transfer and aerodynamics show a partly analogous behavior. Wall shear stress and heat transfer show a similar behavior in the outflow region (for $x/c_{ax} > 1$), where both are considerably higher than in the inflow region due to increased free stream velocity. Furthermore, locally increased heat transfer can be observed near the leading edge where both legs of the horseshoe vortex system cause rapid transport of fluid perpendicular to the platform. However, compared to oil paint visualization heat transfer is relatively low for $0 < x/c_{ax} < 1$ near the airfoil's pressure side, though in this area wall shear stress seems to be quite elevated. This phenomenon can be explained by the fact that cooled fluid from the airfoil's pressure side is moving on the platform perpendicular to the main passage flow towards the suction side of the neighboring airfoil. Thus, the local adiabatic wall temperature is decreased in this area leading to a lower wall heat flux.

In Fig. 15 it can be seen that endwall heat transfer is highly affected by surface roughness. Even if the roughness consisting of truncated cones is equally distributed over the platform, its effect on heat transfer is quite nonuniform. Besides a tendency to higher local Nusselt numbers due to surface roughness it can be seen that the roughness induced heat transfer augmentation is largest near the airfoil reaching a maximum increase of about 240%.

In order to quantitatively compare platform heat transfer on smooth and rough platforms at various inlet Reynolds numbers and different freestream turbulence, Fig. 16

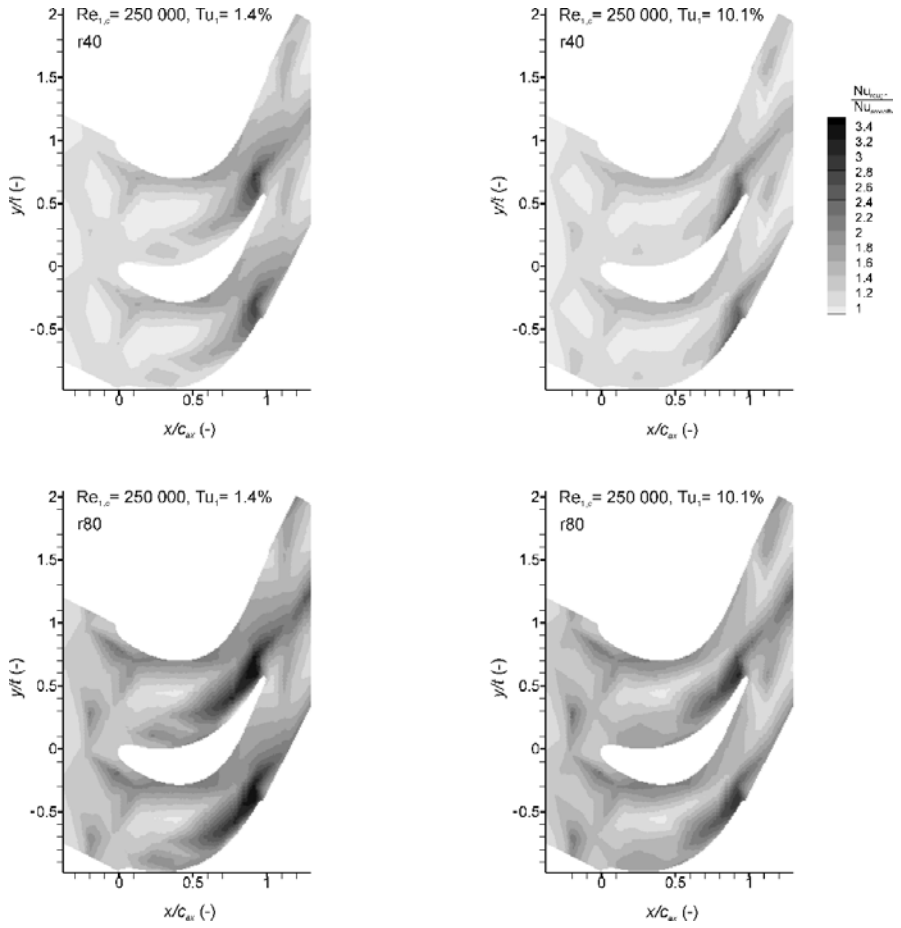

Fig. 15. Platform heat transfer augmentation due to surface roughness at different surface roughness and freestream turbulence.

shows the laterally averaged heat transfer. It may be observed that heat transfer level for smooth surfaces increases with higher Reynolds numbers but does not depend much on freestream turbulence. For small Reynolds numbers the surface roughness has no noticeable effect on heat transfer. However, at increasing Reynolds numbers heat transfer is elevated in the (turbulent) boundary layer of this highly three-dimensional flow. It also can be seen that the highest Nusselt number augmentation takes place in the outflow region, after the flow through the blade cascade has been accelerated. Moreover, it can be observed that the critical Reynolds number above which roughness affects heat transfer, depends obviously on the roughness height. The maximum augmentation in laterally averaged Nusselt number appears for the highest inlet Reynolds number at the largest surface roughness height and is about 110% at $x/c_{\mathrm{ax}} \approx 0.8$.

Figure 17 illustrates the laterally averaged heat transfer increase due to the surface roughness for a variety of operating conditions (varying turbulence intensity and inlet

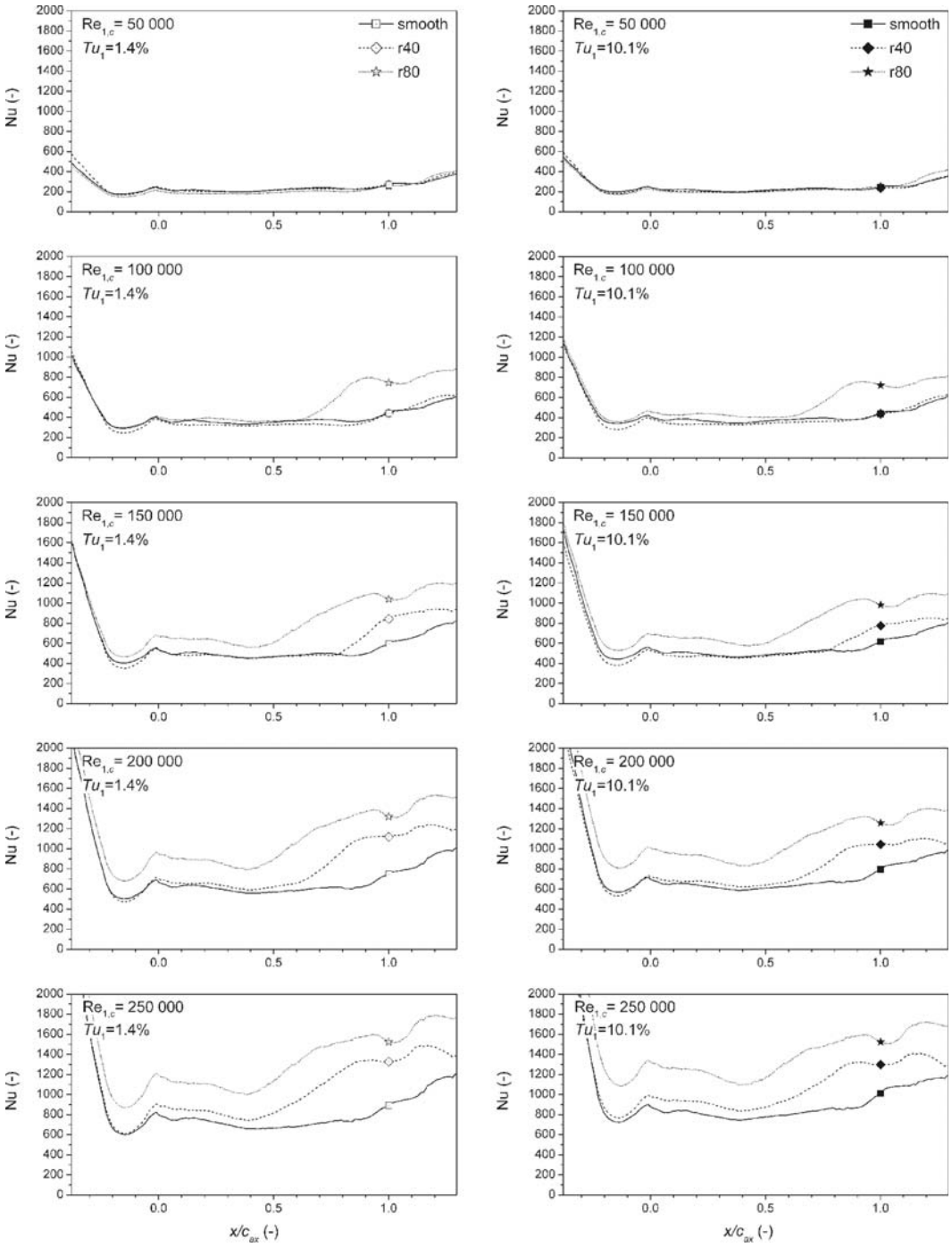

Fig. 16. Laterally averaged platform heat transfer at varying Reynolds number and freestream turbulence for different surface roughness.

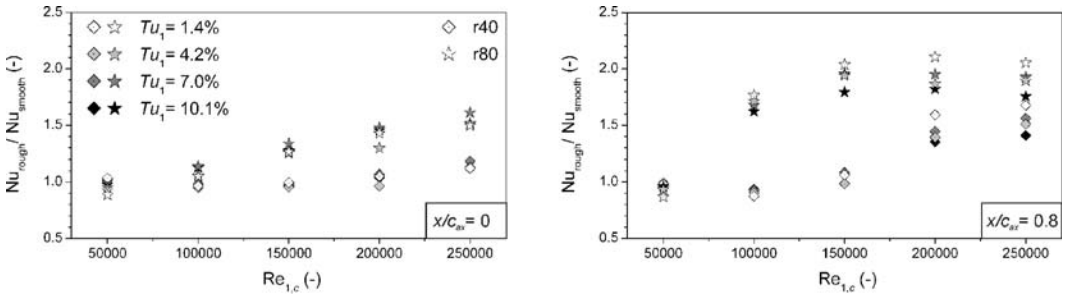

Fig. 17. Increase in laterally averaged platform heat transfer at varying Reynolds number and freestream turbulence for different surface roughness.

Reynolds number) at two locations, the cascade inlet plane (x/c_{ax} = 0) and at the location of maximum heat transfer increase (x/c_{ax} = 0.8). Whereas roughness does not affect heat transfer significantly for low inlet Reynolds numbers, heat transfer augmentation rises for increasing Reynolds numbers. At x/c_{ax} = 0.8, where the complex vortex system dominates the flow and, in addition, local freestream velocity is much higher, this dependency is much more distinct than in the inlet plane. Moreover, at x/c_{ax} = 0.8 a saturation in heat transfer augmentation can be observed: Above a distinct critical Reynolds number (which seems to depend on the roughness height) the increase in the Nusselt number only depends on the roughness height and no longer on the Reynolds number. This leads to the presumption that for the flow at x/c_{ax} = 0.8 the surface is fully rough whereas it is not for x/c_{ax} = 0. A further increase in the inlet Reynolds number should then lead mostly to an increase in heat transfer around the area of the cascade inlet where the local freestream velocity and respectively the Reynolds numbers are rather moderate.

A further issue that can be observed in Fig. 17 is that turbulence intensity plays an increasingly important role with a rising Reynolds number. There seems to be a tendency to lower heat transfer augmentation for increasing freestream turbulence. However, a definite dependency is not visible, which indicates a further influencing parameter. A slightly varying inlet boundary layer thickness at varying turbulence intensity (in different turbulence grid configurations), which is known to have an impact on secondary flow [16], may be a reason for the scatter observed. However, compared to the roughness-induced heat transfer increase, these effects are small.

In order to investigate the influence of boundary layer thickness on platform heat transfer, additional measurements at varying platform boundary layer thickness have been performed. Figure 18 reveals that thin aerodynamic boundary layers lead to slightly decreased heat transfer in the inflow and outflow areas (for $x/c_{ax} < 0$ and $x/c_{ax} > 1$), while heat transfer increases at $0 < x/c_{ax} < 1$ for thin boundary layers. The decreased heat transfer for thin boundary layers in the inflow arises from the smaller aerodynamic boundary layer thickness, which also can be considered as a decreased uncooled starting length of the boundary layer. Kays and Crawford [27] show that

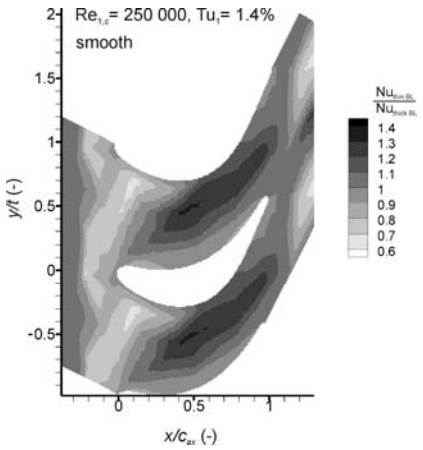

Fig. 18. Comparison of platform heat transfer at different inlet boundary layers ($\delta_{1,\text{thin BL}}$ = 0.3 mm, $\delta_{1,\text{thick BL}}$ = 1.0 mm).

flat plate heat transfer in the region of a starting thermal boundary layer strongly depends on the unheated (or uncooled) starting length. However, the deviation in the heat transfer distribution is below 40% and, considering roughness effects, of minor importance.

Furthermore, a comparison of measurements on the smooth airfoil at different platform surfaces shows that heat transfer in the near hub region increases only slightly with surface roughness where the maximum local augmentation is below 40% (rough platform with roughness r80 compared to smooth surface).

4. CONCLUSION

Measurements on a highly loaded low-pressure turbine blade and its platform have been presented accounting for secondary flow effects on external heat transfer. Surface roughness effects on endwall heat transfer have been investigated. It has been shown that airfoil heat transfer is highly affected by secondary flow effects near the endwall. Moreover, airfoil heat transfer is strongly influenced by freestream turbulence. It has been observed that turbulence intensity does not affect the endwall Nusselt number distribution to the same extent. However, surface roughness increases endwall heat transfer dramatically, leading to a maximum Nusselt number augmentation of 240% in some regions of the platform, whereas effects of varying platform boundary layer thickness and heat transfer augmentation on the (smooth) airfoil close to the endwall due to platform surface roughness are smaller by one order of magnitude.

ACKNOWLEDGMENTS

This work has been performed within a joint research project POWER PLANTS FOR THE 21st CENTURY (KW21) initiated by the German federal states of Baden-Wuerttemberg and Bayern and partly funded by MTU Aero Engines. The permission for publication is gratefully acknowledged by the authors.

NOMENCLATURE

c	chord length, = 65.23 mm
c_{ax}	axial chord length, = 58.00 mm
d	roughness element base diameter, m
h	heat transfer coefficient, = $\dot{q}_w/(T_{0,1} - T_w)$, W/m^2/K
h	airfoil span or wind tunnel width, = 0.1m
h_m	roughness meltdown height, m
k	roughness element height, m
k	thermal conductivity, W/m/K
k	turbulent kinetic energy, m^2/s^2
$k_{s,eq}$	equivalent sand grain roughness, m
K	acceleration parameter
L_ε	turbulent dissipation length, m
$\dot{m}$	mass flow, kg/s
M	Mach number
Nu	Nusselt number, = hc/k
p	pressure, Pa
$\dot{q}$	heat flux, W/m^2
R_a	arithmetic average roughness height, m
$Re_{1,c}$	inlet Reynolds number, = $u_1 c/v$
s	surface length, m
t	Pitch, = 49.45 mm
t_1, t_2	roughness element distance, m
T	temperature, K
Tu	turbulence intensity, %
u	velocity, m/s
V_R	roughness element volume, m^3
x	coordinate in axial direction, m
y	coordinate in lateral direction, m
z	coordinate in spanwise direction, m

Greek symbols

$\Delta A/A_S$	roughness surface increase, %
δ_1	displacement thickness, m
ε	turbulent dissipation rate, m^2/s^3
γ	isentropic exponent
Λ_R	roughness density parameter
ν	kinematic viscosity, m^2/s
Π	pressure ratio

Subcripts

0	refers to stagnation point
1	at cascade inlet

∞	in freestream
cl	coolant
is	isentropic
max	maximum
stat	static
w	wall
BL	boundary layer
TC	thermocouple.

REFERENCES

1. Schulz, A. Zum Einfluβ hoher Freistromturbulenz, intensiver Kühlung und einer Nachlaufströmung auf den äuβeren Wärmeübergang einer konvektiv gekühlten Gasturbinenschaufel, Dissertation, Institut für Thermische Strömungsmaschinen, Universität Karlsruhe, Germany, 1986.
2. Dullenkopf, K., Schulz, A., and Wittig, S. Turbine airfoil heat transfer under simulated wake conditions. In: *Proc. ICHMT, 1st Symp. Heat Transfer in Turbomachinery*, Vol. 0'1994, pp. 423–436, 1994.
3. Mayle, R. E. The role of laminar–turbulent transition in gas turbine engines, *J. Turbomachinery*, 1991, Vol. 113, pp. 509–537.
4. Dullenkopf, K. and Mayle, R. E. An account of free-stream-turbulence length scale on laminar heat transfer, *J. Turbomachinery*, 1995, Vol. 117, pp. 401–406.
5. Mayle, R. E., Dullenkopf, K., and Schulz, A. The turbulence that matters, *J. Turbomachinery*, 1998, Vol. 120, pp. 402–409.
6. Schiele, R., Sieger, K., Schulz, A., and Wittig, S. Heat transfer investigations on a highly loaded, aerothermally designed turbine cascade. In: *Proc. 12th Int. Symp. Air Breath. Engines*, pp. 1091–1101, Melbourne, 1995.
7. Bons, J. P. and McClain, S. T. The effect of real turbine roughness with pressure gradient on heat transfer, J. Turbomachinery, 2004, Vol. 126, pp. 385–394.
8. Stripf, M., Schulz, A., and Wittig, S. Surface roughness effects on external heat transfer of a HP turbine vane, *J. Turbomachinery*, 2005, Vol. 127, pp. 200–208.
9. Stripf, M., Schulz, A., Bauer, H.-J., and Wittig, S. Extended Models for Transitional Rough Wall Boundary Layers With Heat Transfer — Part I: Model Formulations, *J. of Turbomachinery*, 2009, Vol. 131, pp. 031016-1–10.
10. Sieverding, C. H. Recent progress in the understanding of basic aspects of secondary flows in turbine blade passages, *J. Eng. Gas Turbines Power*, 1985, Vol. 107, pp. 248–257.
11. Langston, L. S. Secondary flows in axial turbines — a review, *Annals New York Acad. Sci.*, 2001, Vol. 107, pp. 11–26.
12. Langston, L. S., Nice, M. L., and Hooper, R. M. Three-dimensional flow within a turbine cascade passage, *J. Eng. Power*, 1977, Vol. 99, pp. 21–28.

13. Wang, H. P., Olson, S. J., Goldstein, R. J., and Eckert, E. R. G. Flow visualization in a linear cascade of high performance turbine blades, *J. Turbomachinery*, 1997, Vol. 119, pp. 1–8.
14. Chen, P. H. and Goldstein, R. J. Convective transport phenomena on the suction surface of a turbine blade including the influence of secondary flows near the endwall, *J. Turbomachinery*, 1992, Vol. 114, pp. 776–787.
15. Goldstein, R. J., Wang, H. P., and Jabbari, M. Y. The influence of secondary flows near the endwall and boundary layer disturbance on convective transport from a turbine blade, *J. Turbomachinery*, 1995, Vol. 117, pp. 657–665.
16. Graziani, R. A., Blair, M. F., Taylor, J. R., and Mayle, R. E. An experimental study of endwall and airfoil surface heat transfer in a large scale turbine blade cascade, *J. Eng. Power*, 1980, Vol. 102, pp. 257–267.
17. Blair, M. F., An experimental study of heat transfer in a large-scale turbine rotor passage, *J. Turbomachinery*, 1994, Vol. 116, pp. 1–13.
18. Stripf, M., Schulz, A., and Bauer, H.-J. Roughness and secondary flow effects on turbine vane external heat transfer, *J. Propul. Power*, 2007, Vol. 23, No. 2, pp. 283–291.
19. Lorenz, M., Stripf, M., Schulz, A., and Bauer, H.-J. External heat transfer measurements on a turbine airfoil in a linear cascade. In: *Proc 19th Int. Symp. Transport Phenomena*, Reykjavik, 2008, ISTP-19 Paper No. 135.
20. Schiele, R. Die transitionale Grenzschicht an Gasturbinenschaufeln: Experimentelle Untersuchungen und Entwicklung eines neuen Verfahrens zur numerischen Beschreibung des laminar-turbulenten Umschlags, Dissertation, Institut für Thermische Strömungsmaschinen, Universität Karlsruhe, Germany, 1999.
21. Kline, S. J. and Mc Clintock, F. A. Describing uncertainties in single-sample experiments, *Mech. Eng*., 1953, Vol. 77, pp. 3–8.
22. Stripf, M. Einfluss der Oberflächenrauigkeit auf die transitionale Grenzschicht an Gasturbinenschaufeln, Dissertation, Institut für Thermische Strömungsmaschinen, Universität Karlsruhe, Germany, 2007.
23. Turner, A. B. Heat Transfer Instrumentation, AGARD-CP-73, 1970.
24. Wittig, S., Schulz, A., and Bauer, H.-J. Effects of Wakes on the Heat Transfer in Gas Turbine Cascades, AGARD-CP-390, 1985.
25. Stripf, M., Schulz, A., and Bauer, H.-J. Surface roughness and secondary flow effects on external heat transfer of a high pressure turbine vane, *AIAA J. Propul. Power*, 2005, Vol. 23, pp. 283–291.
26. Waigh, D. R. and Kind, R. J. Improved aerodynamic characterization of regular three-dimensional roughness, *AIAA J*., 1998, Vol. 36, No. 6, pp. 1117–1119.
27. Jones, W. P. and Launder, B. E. The prediction of laminarization with a two-equation model of turbulence, *Int. J. Heat Mass Transfer*, 1972, Vol. 15, pp. 301–314.
28. Kays, W. M. and Crawford, M. E. *Convective Heat and Mass Transfer*, Third Ed., New York: McGraw-Hill, 1993.

□◆◆◆□

Heat Transfer Research, 2010, Vol. 41, No. 8

Experimental Study of Heat Transfer from Impinging Jet with Upstream and Downstream Crossflow

DANIEL THIBAULT, MATTHIEU FÉNOT, GILDAS LALIZEL,

and EVA DORIGNAC*

Laboratoire d'Études Thermiques — UMR CNRS 6608,
ENSMA — University of Poitiers,
BP 40109 — 86961 Chasseneuil Cedex France

Numerous geometrical and flow parameters can affect the heat transfer in the impinging jet cooling methods. In this study, a configuration close to a real case of vane cooling was adopted. It consists of a main crossflow flowing into an injection hole of diameter D perpendicular to the main flow through a thin plate of thickness t equal to D and the Reynolds number of the injection is fixed to 23,000. A secondary crossflow with a Reynolds number of 1000 is fixed between the exit of the jet and the impingement region, to simulate the flow stream evacuation from the leading edge to the trailing edge of the vane. This geometry is very different from a jet issued from a long pipe as described in many previous studies. The flow field of the jet in the present case has a three-dimensional behavior due to its complex geometry. High levels of turbulence at the exit of the nozzle are observed with Particle Image Velocimetry measurements. The fields of the reference temperature and convective heat transfer coefficient on the impingement surface are calculated from infrared thermography measurements. The results show a significant drop of the heat transfer in such geometry.

* * *

Keywords: forced convection, impingement, upstream crossflow, downstream crossflow, infrared thermography, particle imaging velocity, heat transfer coefficient, velocity distribution, turbulent intensity distribution

*Address all correspondence to Eva Dorignac E-mail: eva.dorignac@ensma.fr

ISSN1064-2285

1. INTRODUCTION

Jet impingement methods are widely used in industrial application for cooling, heating or drying. Some examples are cooling metal and glass, drying paper and textiles, and cooling electrical equipment. In a gas turbine, jet impingement has been commonly used for cooling combustion liners, transition pieces, and airfoils. These components are exposed to high thermal stresses since gas temperature is around 2000 K, which is above the metal melting point (around 1400 K). Thus, it is necessary to cool these elements with effective cooling methods, since it affects the components' longevity and the performances of the engine. This study focuses on internal vane cooling by jet impingement method. The flow and heat transfer from an impinging jet depend on many parameters such as nozzle-to-wall spacing, Reynolds numbers, position from the stagnation point, design of the injection. The most commonly used injection geometries in previous studies are axisymmetric (circular) orifice or pipe [1] and slot (two-dimensional) nozzles [2]. The flow field [3] of an impinging jet issued from a long pipe can be divided into three zones (see Fig. 1): the free jet prior to the impingement, the impingement region, and the wall region. The free jet region can also be divided into three zones depending on the nozzle-to-wall spacing: the potential core, the transition zone, and the fully developed zone. In the potential core, the velocity at the centerline is maintained while the shear layer is growing. This shear layer begins to perturb the centerline of the jet in the transition zone, until the velocity profiles reach a self-similar behavior in the fully developed zone. It appears that the maximum of heat transfer occurs for nozzle-to-wall spacing corresponding to the length of the potential core (typically 4 to 6 slot widths or hydraulic diameters).

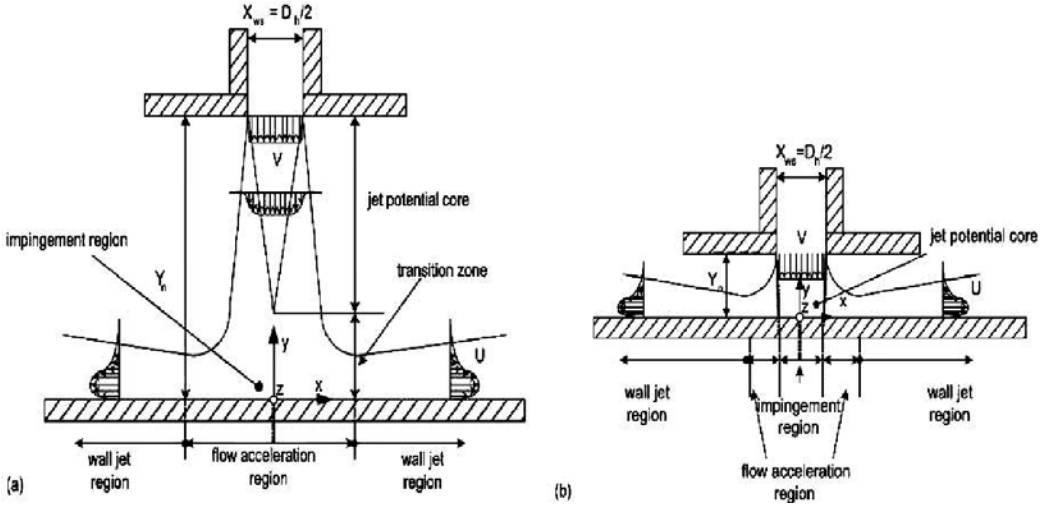

Fig. 1. Schematic of a transitional jet (a) and a potential-core jet (b) impingement on a flat surface (from [4]).

Several experimental studies have dealt with heat transfer and/or fluid mechanics aspect investigating different parameters. Gardon and Akfirat [5] correlated the influence of streamwise turbulence intensity of free jet on the heat transfer for a slot configuration. Yokobori et al. [6, 7] focused on the behavior of turbulence for transitional jet impingement and confirmed the existence of pairs of counter-rotating, large scale, streamwise vortices at stable nodal locations and discussed their relation with the upstream shear layer vortices. It has been deduced that these coherent structures influenced the heat transfer. Other studies have shown a nonmonotonic trend in the repartition of the local heat transfer coefficient in low nozzle-to-wall spacing cases ($H/D \leq 2.5$). Hoogendoorn [8] and Lytle and Webb [2] reported the existence of two peaks in the radial distribution of heat transfer coefficient for axisymmetric jets. The first peak occurs at $r/D = 0.5$ and was attributed to the thinning of the accelerating boundary layer. Then, a minimum is observed around $r/D = 1.2$, and Hoogendoorm related it to a minimum in turbulence intensity and a maximum in radial velocity at the same position in radial distribution. Goldstein et al. [9] have concluded that the existence and the position of the secondary peak depend on the Reynolds number of the injection, the nozzle-to-wall spacing, and the nozzle geometry. It was observed when the thickness of linear momentum in the mixing layer is very small compared to the hydraulic diameter of the injection. Several explanations have been proposed for this secondary peak such as transition of the boundary layer to a turbulent flow and creation of secondary vortices near the impingement wall. Many prior studies focused on other parameters such as specific nozzle geometry, confinement [10, 11], angle of incidence between a jet and impingement wall [12], and curve of the impingement wall [13]. Carcasci [14] studied the influence of multiple jets with crossflow downstream the injection when this crossflow is minor compared to the injection flow field. He concluded that the crossflow has no significant effects near the impingement plate but has a little influence on the upstream vortices. According to [15], these effects grow up when the crossflow intensity become comparable with the one encountered in the injection flow field and degrade the heat transfer performance. The influence of the upstream crossflow was not studied as an independent parameter.

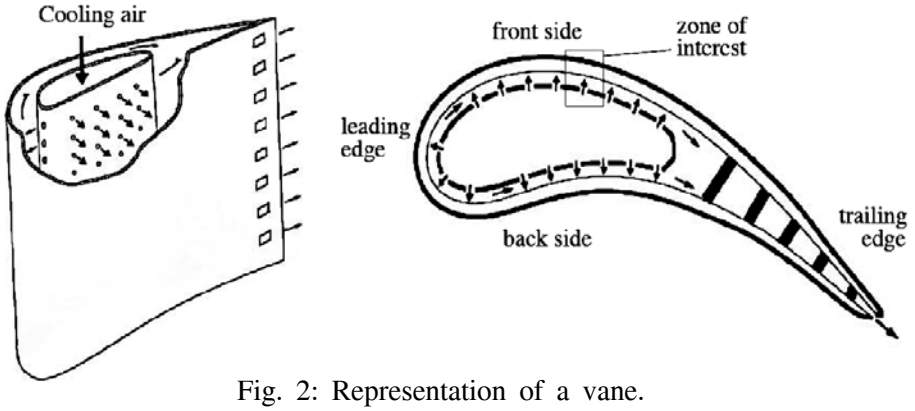

Fig. 2: Representation of a vane.

This lack of information motivates the following investigations on both the aerodynamic and thermal sides dealing with a single jet impinging on a flat plate with the presence of upstream and downstream crossflows. In this way, the present study is close to a real configuration of internal cooling at the back side and the front side of a vane (see Fig. 2).

2. EXPERIMENTAL SETUP

The experimental setup is designed so that Thermography and PIV measurements could have an access to convective heat transfer coefficient distribution and velocity fields.

2.1 Test Section

The test section consists of a main rectangular pipe along the y-axis where the main upstream crossflow goes with y decreasing (see Fig. 3). A hole for injection of diameter D is made in the injection plate (one of the walls of the main rectangular pipe) of thickness D. A jet emerges along the z-axis from this injection hole and impinges on the wall representing the external part of the vane. The duct formed by the injection plate and the impingement wall is called air-gap and the nozzle-to-wall spacing is H taking the values H/D = 2, 4, 5, 6, 8, and 10. A downstream crossflow is fixed along the x-axis between the exit of the nozzle and the impingement wall, simulating evacuation of the flow stream from the leading edge to the trailing edge. The secondary crossflow passing through the air-gap is characterized by a Reynolds number Re_{gap} of 1000. The injection Reynolds number Re_{inj} takes the value of 23,000. The main flow of the internal cooling jacket has a Reynolds number Re_{jack} of 20,000, 40,000, and 60,000. The test section is feed by a fan (see Fig. 4) followed by a water cooling jacket. Thus, the temperature of the air circulating in the test section is controlled and maintained to the ambient temperature. Venturi meters and valves are present at the inlets and the exits of the internal cooling jacket as well as the air-gap pipes in order to fix the different Reynolds number of the different flows.

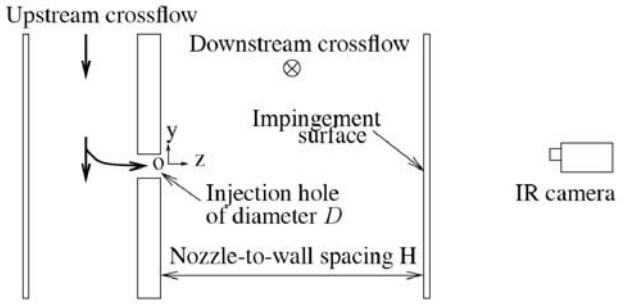

Fig. 3. Plan of the test section.

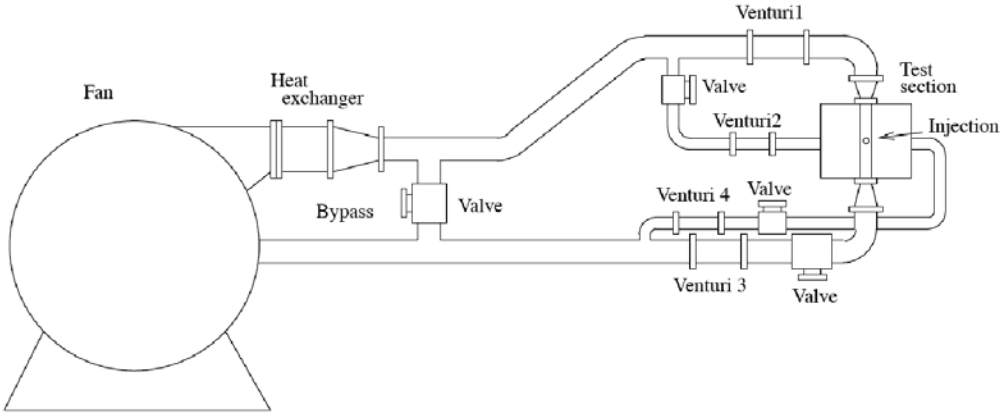

Fig. 4. Schematic diagram of the experimental setup.

2.2 PIV Measurements

Several plans are scanned for standard PIV measurements (see Fig. 5). An Nd–Yag laser at 8-Hz frequency with a camera of resolution 1248 × 1024 was used with the FlowManager software to obtain mean and rms velocity fields. The flows are being seeded with paraffin oil drops of 1 μm diameter. The different plans are of *xz* and *yz* type located in the air-gap to measure the flow field of the jet. Three parallel and equidistant plans of *xz* type are located on both sides of the hole at $y = -0.5D$, $y = 0$, and $y = 0.5D$. Five other plans of type *yz* go from side to side of the hole at $x = -0.5D$, $x = -0.25D$, $x = 0$, $x = 0.25D$, and $x = 0.5D$.

2.3 Heat Transfer Measurement

The jet exits from the injection hole and impinges on the front side of the impingement wall. This wall is a 0.8-mm-thick epoxy plate of measured thermal con-

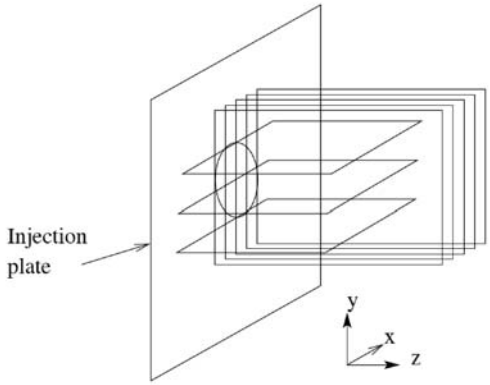

Fig. 5. Families of PIV measurements plans.

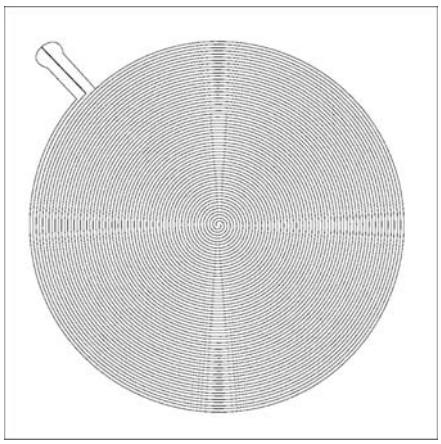

Fig. 6. Design of the heating plate.

ductivity of $k = 0.320 \pm 8.10^{-3}$ W/m·K, with an electric circuit of copper of thickness 35 μm on the front side, which is supplied with power to produce a constant heat flux. Since the electric circuit has a spiral design (see Fig. 6), no direction is privileged, and the conductive heat flux in the copper circuit is limited. The plate is covered with black paint of known emissivity $\varepsilon = 0.95 \pm 0.02$. An infrared camera (CEDIP Jade) measures the backside of the plate temperatures T_b and so, the reference temperatures T_{ref} and the fields of the convective heat transfer coefficients h can be calculated (see Fig. 7) using the method detailed by Fénot et al. [16]. It consists in electrically heating the copper circuits. This enables the experimenter to calculate the extract electrical flux density dissipated by Joule effect $\dot{q}_{elec}$. Radiative and convective losses $\dot{q}_{rad,f}$, $\dot{q}_{rad,b}$, and $\dot{q}_{conv,b}$ must be calculated to obtain the convective heat flux density on the front side $\dot{q}_{conv,b}$, which represents the exchange between plate and jet. Temperature is measured at the back, side of the plate, and the front tem-

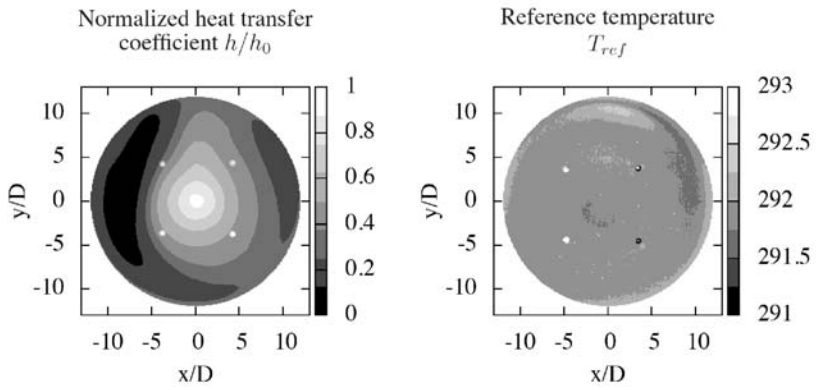

Fig. 7. Example of heat transfer coefficient normalized with heat transfer coefficient at the stagnation point and reference temperature cartography on impingement side with $Re_{inj} = 23{,}000$ and $H/D = 2$.

perature can be calculated from the back temperature according the following equation:

$$T_f = T_b + \frac{t}{k}(\dot{q}_{conv,b} + \dot{q}_{rad,b}) \ . \tag{1}$$

The front side temperature T_f and the convective heat flux on the front side $\dot{q}_{conv,b}$ are obtained making the balance of the different heat fluxes on the impingement plate:

$$\dot{q}_{conv,f} = \dot{q}_{elec} - \dot{q}_{conv,b} - \dot{q}_{rad,f} - \dot{q}_{rad,b} \ , \tag{2}$$

with

$$\dot{q}_{rad,b} = \varepsilon\sigma(T_b^4 - T_{ambient}^4) \ , \tag{3}$$

$$\dot{q}_{rad,f} = \varepsilon\sigma(T_f^4 - T_{ambient}^4) \ , \tag{4}$$

$$\dot{q}_{conv,b} = h_b(T_b - T_{ambient}) \ , \tag{5}$$

where h_b is previously measured by a similar method isolating the front side. Then, four different electrical heat flux densities are injected, and the corresponding convective heat flux density and wall temperature are measured. Linking each couples of values ($\varphi_{f,conv}$, T_f) with a straight line using a linear regression determines $1/h$ which is the slope and T_{ref} which is the y-intercept, according to the following relation:

$$\dot{q}_{rad,f} = h(T_f - T_{ref}) \ . \tag{6}$$

Uncertainties are calculated using a statistical approach, NF ENV 13005 [17]. Errors due to electrical, radiative, and convective fluxes, and to emissivity are taken into account. Random uncertainty for the Nusselt numbers is no higher than 5% and overall uncertainty is no higher than 11%.

3. RESULTS AND DISCUSSION

The PIV measurements reveal the highly 3D shape of a flow field that is very different from the description made for a jet issued from a long pipe. The flow field drives the heat transfer at the impingement surface and explains the characteristics of the convective heat transfer distribution.

3.1 Flow Field Topology

Figure 8 shows a jet with a Reynolds number equal to 23,000 and a nozzle to-wall spacing of $6H/D$. The quantity U_q is the mean velocity based on the Reynolds number of the injection and normalized velocity U/U_q, and turbulence intensity fields are represented at 5 equidistant plans, parallel to the yz plan, and passing by $x/D = -0.5$, -0.25, 0, 0.25, and 0.5. The majority of the flow passes only through the lower half part of the injection hole ($-0.5 \le y/D \le 0$). The jet axis makes a slight angle with the

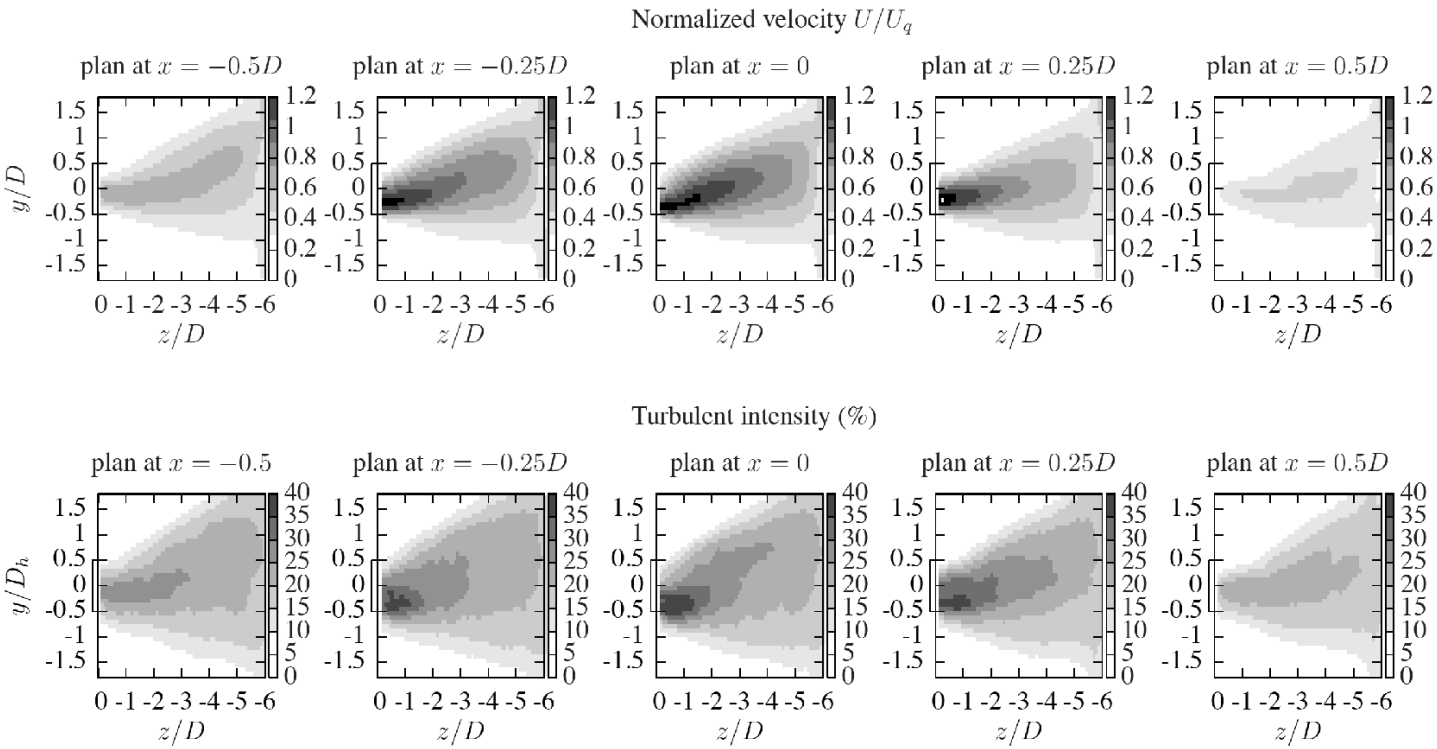

Fig. 8. Normalized velocity U/U_q and turbulent intensity fields at yz type plans with Re_{inj} = 23,000 and H/D = 6.

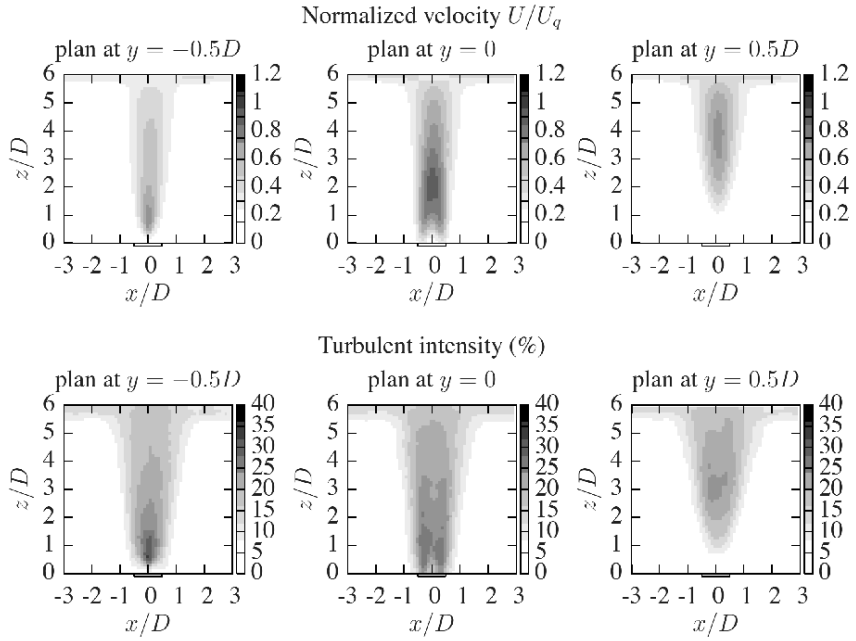

Fig. 9. Normalized velocity U/U_q and turbulent intensity fields at *xz* type plans with Re_{inj} = 23,000 and *H*/*D* = 2.

z-axis meaning that a part of the main flow collides with the lower half part of the injection hole and bounces in the opposite direction (0 ≤ *y*). The stagnation point position is still near the center position despite the prior influences, and this is observed at *H*/*D* = 4, 5 or 6. The turbulence intensity is very important at the exit of the nozzle and presents a topology similar to the mean velocity. This distribution is far from the mean and rms velocity fields encountered in the case of a jet issued from a long pipe.

Measurements in equidistant plans, parallel to the *xz* plan, and passing by *y*/*D* = –0.5, 0, and 0.5 show that the flow field is more complicated. In Fig. 9, the velocity fields in the plan *y* = –0.5 present high levels at the center of the nozzle, in the plan *y* = 0 the velocity is weak at the center and important at the sides, and in the plan *y* = 0.5 the velocity is nil. The jet appears to exit the injection hole through the half lower part, and the zone with few velocities at the center of the hole means that the jet exits the nozzle in a crescent-shape way. This could be explained by the presence of the upstream crossflow that suddenly changes its direction. This makes the velocity fields concentrated on the lower part of the hole and create a dead zone at the upper part. The analysis of these velocity fields confirms the jet has an inclination with the *z*-axis. The influence of the secondary crossflow is not significant on the shape of the mean velocity distribution because of its weak linear momentum compared to the injection linear momentum (ratio around 0.003). The turbulence intensity levels are also investigated at the same plans of measurements. In the reference case, the turbulence

intensity is low (%) and presents a homogeneous distribution at the exit of the nozzle, thereafter it grows up in the mixing layer. In the case of the present study, the distribution of the turbulent intensity presents the same crescent-shape of the mean velocity. The jet exits the nozzle with extremely high turbulence, around 30–40%, which is far from the levels encountered in a situation of a long pipe impinging jet. The levels of turbulent intensity drops rapidly after the nozzle. The influence of these different characteristics on heat transfer is investigated with the aid of infrared thermography.

3.2 Heat Transfer Distribution

The way the heat transfer coefficient is distributed is directly driven from the flow field topology. In this case, the behavior of the jet is very complex and different from a jet issued from a long pipe. It makes the heat transfer distribution difficult to estimate. Figure 10 compares the profiles of the convective heat transfer coefficient for a jet issued from a long pipe and for the present configuration. A nonaxisymmetric distribution of the convective heat transfer coefficient appears for the case of the present study. This behavior is expressed by an ovoid shape along the *y*-axis. The original crescent-shaped of the velocity distribution observed at the exit of the nozzle is an element of explication for the characteristic of nonaxisymmetry. The particular shape of heat transfer coefficient distribution could also be explained by the angle the jet makes with the *z*-axis. As shown in Fig. 8, the mean and rms velocity fields present higher levels in the upper part ($0 \leq y$) near the impingement wall. It contributes to an increase in heat transfer in this zone and induces a deviation of the heat transfer distribution with y increasing. The influence of the secondary crossflow is significant, and some deviation effects along the *x*-axis appear. The profile of a jet issued from a long pipe presents a peak at low nozzle-to-wall distance that does not appear

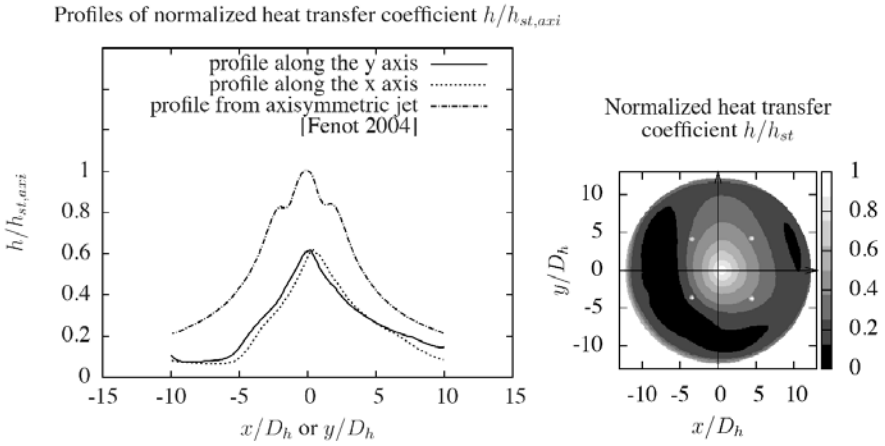

Fig. 10. Heat transfer coefficient distribution and comparison with a jet issued from a long pipe [18] at Re_{inj} = 23,000 and H/D = 2.

in the case of the present study. The extracted profiles of heat transfer coefficient are monotonic and show variations along the different axis, and the levels of heat transfer are lower than in the reference case by about 30%. The particularities of the flow field topology lead to a very complex heat transfer distribution with different influences. The high levels of turbulent intensity at the exit of the nozzle decrease rapidly, and could be responsible for making the turbulent energy less powerful when reaching the impingement plate. It also could be responsible for the absence of the peaks in heat transfer distribution destroying the coherent structures observed in the reference case. The secondary crossflow must disturb the structure of the jet making the velocity and turbulent intensity to dissipate more rapidly.

4. CONCLUSIONS

The complex geometry of the injection presented in this study lead to a particular flow field topology. The distribution of the velocity and the turbulent intensity is of crescent shape at the exit of the nozzle, with high levels of turbulence, and these values decrease rapidly to low levels after the injection. This provides a nonaxisymmetric distribution of the convective heat transfer coefficient with low levels compared to the reference case.

ACKNOWLEDGMENTS

This study is supported by SNECMA from SAFRAN group, and the authors would thank Mr. Laurent Descamps and Mr. Christophe Scholtes for their participation.

REFERENCES

1. Jambunathan, J. E., Lai, E., Moss, M. A., and Button, B. L. A review of heat transfer data for single circular jet impingement, *Int. J. Heat Fluid Flow*, 1992, Vol. 13, No. 2, pp. 106–115.
2. Lytle, D. and Webb, B. W. Air jet impingement heat transfer at low nozzle-plate spacing, *Int. J. Heat Mass Transfer*, 1994, Vol. 37, pp. 1687–1697.
3. Viskanta, R. Heat transfer to impinging isothermal gas and flames jets, *Exp. Therm. Sci.*, 1993, Vol. 6, pp. 111–134.
4. Narayanan, V., Seyed-Yagoobi, J., and Page, R. H. An experimental study of fluid mechanics and heat transfer in an impinging slot jet flow, *Int. J. Heat Mass Transfer*, 2004, Vol. 47, Nos. 8–9, pp. 1827–1845.
5. Gardon, R. and Akfirat, J. C. The role of turbulence in determining the heat transfer characteristics of impinging jets, *Int. J. Heat Mass Transfer*, 1965, Vol. 8, No. 10, pp. 101–108.
6. Yokobori, S., Kasagi, N., Hirata, M., and Nishiwaki, N. Role of large-scale eddy structure on enhancement of heat transfer in stagnation region of two-dimen-

sional, submerged, impinging jet, *6th Int. Heat Transfer Conf.*, Toronto, pp. 305–310, 1978.
7. Yokobori, S., Kasagi, N., Hirata, M., Nakamura, M., and Haramura, Y. Characteristic behavior of turbulence and transport phenomena at the stagnation region of an axisymmetrical impinging jet. In: *Proc. 2nd Symp. Turbulent Shear Flows*, London, 1979, pp. 4.12–4.17
8. Hoogendoorn, C. J. The effect of turbulence on heat transfer at a stagnation point, *Int. J. Heat Mass Transfer*, 1977, Vol. 20, No. 12, pp. 1333–1338.
9. Goldstein, R. J., Behbahani, A. I., and Heppelmann, K. K. Streamwise distribution of recovery factor and the local heat transfer coefficient to an impinging circular air jet, *Int. J. Heat Mass Transfer*, 1986, Vol. 29, No. 8, pp. 1227–1235.
10. Asforth-frost, S. and Jambunathan, K. Effect of nozzle geometry and semi-confinement on the potential core of a turbulent axisymmetric jet, *10th Int. Heat Transfer Conf.*, Brighton, 1994.
11. Asforth-frost, S., Jambunathan, K., and Whitney, C. F. Velocity and turbulence characteristics of a semi-confined orthogonally impinging slot jet, *Exp. Fluid Sci.*, 1997, Vol. 14, pp. 60–67.
12. Yan, X. and Saniei, N. Heat transfer from an obliquely impinging circular, air jet to a flat plate, *Int. J. Heat Fluid Flow*, 1997, Vol. 18, pp. 591–599.
13. Lee, D., Chung, Y., and Wong, S. The effect of concave surface curvature on heat transfer from a fully developed rough impinging jet, Int. J. Heat Mass Transfer, 1999, Vol. 42, No. 13, pp. 2489–2497.
14. Carcasci, C. An experimental investigation on air impinging jets using visualization methods, *Int. J. Therm. Sci*., 1999, Vol. 38, pp. 808–818.
15. Wang, T., Lin, M., and Bunker, R. S. Flow and heat transfer of confined impinging jets cooling using a 3-D transient liquid crystal scheme, *Int. J. Heat Mass Transfer*, 2005, Vol. 48, pp. 4887–4903.
16. Fénot, M., Vullierme, J. J., and Dorignac, E. A heat transfer measurement of jet impinging with high injection temperature, *Comptes Rendus Mécaniques*, 2005, Vol. 333, No. 10, pp. 778–782.
17. Bureau Qualité-Statistique Estimation des incertitudes de mesures, *LNE*, NF ENV 13005, 1997.
18. Fénot, M. Etude du Refroidissement par Impact de Jets — Application aux aubes de Turbines, Ph.D. Thesis, ENSMA Therm. Study Dept., Poitiers, 2004.

□◆◆◆□

Heat Transfer Research, 2010, Vol. 41, No. 8

Experimental and Theoretical Analysis of Heat Transfer Characteristics in a Rectangular Duct with Jet Impingement*

U. UYSAL,[a*] F. SAHIN,[b] and M. K. CHYU[c]

[a]Department of Mechanical Engineering, Sakarya University, 54187 Sakarya, TURKEY

[b]General Directorate of Highways, 07000 Antalya, TURKEY

[c]Department of Mechanical Engineering and Materials Science, University of Pittsburgh, PA, USA

The heat transfer characteristics are analyzed in a rectangular cross section duct where impingement jet technique is applied for the purpose of heating and cooling. Heat transfer characteristics on surfaces are calculated using commercial CFD software, Fluent. Numerical results are compared with the experimental results obtained through a transient liquid crystal technique. To better present the heat transfer results, different cross-sectional size geometric models are used. The geometric models are of six in-line circular jets housed in a confined rectangular channel. As the jet temperature varies with time during a transient test, a time-depended solution method was selected in Fluent. One of the primary varying parameters in the present study is the magnitude of spacing between the jet exit and target plate. The jet Reynolds numbers range from 14,000 to 40,000 for every geometry. The effects of crossflow on the overall flow characteristics in the housed channel and heat transfer distributions on both target surface and jet-issuing plate are investigated. Comparison was made between the present numerical results and experimental data obtained earlier by the lead author, Uysal et al. [1]. The companion experimental study was based on the transient thermochromic liquid crystal (TLC) measurements on detailed local heat transfer distributions on both the target surface and jet-issuing surface.

* * *

*Address all correspondence to U. Uysal E-mail: uysal@sakarya.edu.tr

ISSN1064-2285

Key words: impingement jets, thermochromic liquid crystals, forced convection in ducts, gas turbines cooling

1. INTRODUCTION

Among heat transfer enhancement techniques, jet impingement is of great potential to increase the local heat transfer coefficient significantly. This is attributable to the impingement boundary layers that are much thinner, and often the spent flow after the impingement serves to further agitate the surrounding fluid. Impinging jets provide an effective and flexible approach to transfer energy or mass between a surface and the fluid in various applications. Heat transfer applications include cooling of stock materials during forming processes, heat treatment, cooling of electronic components, heating of optical surfaces, cooling of turbine airfoils, and many other industrial processes. In addition, the impingement cooling approach typically offers a compact design arrangement with no additional moving parts.

Convective heat transfer with jet impingement has been a subject of intensive studies in the open literature for several decades. Relatively recent studies relevant to the present work are given as follows. Lim et al. [2] using the steady thermochromic liquid crystal (TLC) technique, measured the heat transfer coefficients on hemispherical surfaces. Huang et al. [3] used the similar TLC method but in a transient mode to study jet impingement heat transfer on various target surfaces. Ichimiya and Yamada [4] numerically examined the heat transfer and flow characteristics of a single circular laminar impinging jet including buoyancy force in a comparatively narrow space with a confined wall. Aldabbagh et al. [5] numerically investigated the flow and heat transfer characteristics of an impinging laminar square jet with crossflow by solving the three-dimensional Navier–Stokes and energy equations under steady-state conditions. San and Lai [6] studied the effects of jet-to-jet spacing on the local Nusselt number for confined circular air jets impinging on a flat plate. They used five jets in equilaterally staggered arrays and evaluated optimal ratios of jet-to-jet spacing, Re and jet height on the stagnation Nusselt number. Azad et al. [7] experimentally examined the jet impingement heat transfer for array of in-line air jets of a four by three array with the effects of dimpled (rough) target surfaces. Ai et al. [8] conducted two separate tests with different injection flow temperature rises under the same free-stream temperature and flow conditions. Lee and Lee [9] investigated the local and average heat transfer characteristics of an axisymmetric submerged air impinging jet in the stagnation region. Gao and Ekkad [10] investigated impingement heat transfer in applications that have hole-spacing linearly stretched for better coolant coverage. Muhammad and Raghavan [11], carried out a numerical simulation of heat transfer with crossflow under the conditions of mixed convection for cooling of electronic circuit boards. Huang et al. [3] investigated the detailed heat transfer coefficient distributions using the transient TLC method for jet arrays of orthogonal impingement. Kiger et al. [12] studied single-nozzle spray cooling heat transfer phenomena with varying amounts of dissolved gas.

In addition to the studies aforementioned, most of experimental and numerical findings on jet impingement heat transfer have been summarized in [13]. There are several key parameters that dictate the characteristics of impingement heat transfer and need to be considered for optimizing design of practical systems. The shape of jet nozzle, layout of jet holes, distance between the impinging and issuing jet plates and jet orientations all have significant effects on the magnitude as well as the spatial distributions of heat transfer coefficient over both the target and jet-issuing surfaces. In general, the overall average heat transfer on both participating surfaces is inversely proportional to the spacing between the plates [14]. Whereas other applications may involve various jet shapes and jet-to-target spacing, typical jet impingement configurations for cooling of turbine airfoils have a spacing-to-jet-diameter ratio H/D of about 1 to 3 [15]. Often reported in the literature is that for the cases with a relatively narrow spacing (e.g., H/D = 1), the heat transfer pattern is evidenced by the presence of a secondary peak near the primary impingement region. To achieve a better thermal design while eliminating hot spots, both the overall average heat transfer information and its local spatial distribution are necessary. In addition, a jet impingement cooling system implemented for turbine airfoil cooling is essentially a compact heat exchanger where every participating surface will contribute toward the overall cooling duty. Therefore, to gain detailed knowledge of local heat transfer coefficient on both jet issuing plate (or simply jet plate) and jet impinging plate is critical, and thus is one of the main objectives of this study. As mentioned earlier, the present study involves both experimental measurement using transient TLC and CFD simulation based on FLUENT.

2. NUMERICAL METHOD

Figure 1 shows the geometry of the model channel. A smooth outlet extension with a length of X/D_h = 4.55 to 37.1 was included to avoid influence of the outlet

Table 1.
Positions of jets

Uniform jet diameter D_h = 7.94 mm					
Jet	X, mm	X/D_h	G1 H = 6.4 mm H/D_h	G2 H = 12.7 mm H/D_h	G3 H = 19.1 mm H/D_h
1	36.2	4.55	0.81	1.6	2.41
2	87.8	11.05	0.81	1.6	2.41
3	139.4	17.55	0.81	1.6	2.41
4	191.0	24.05	0.81	1.6	2.41
5	242.6	30.55	0.81	1.6	2.41
6	294.2	37.05	0.81	1.6	2.41

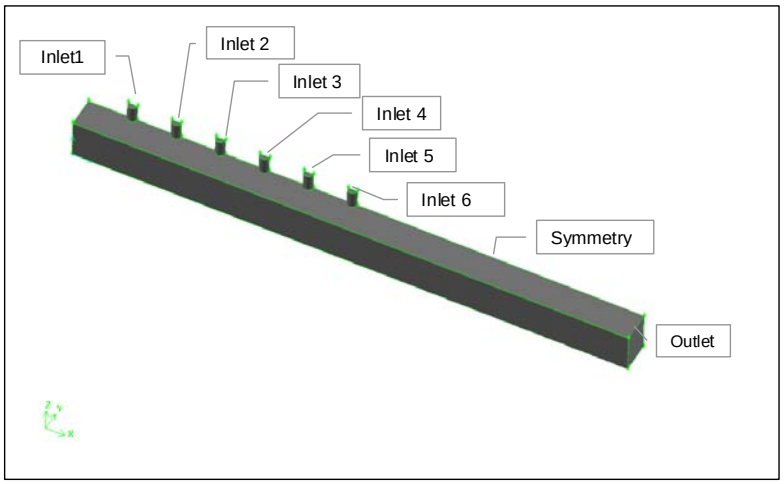

Fig. 1. Geometry of the investigated numerical model.

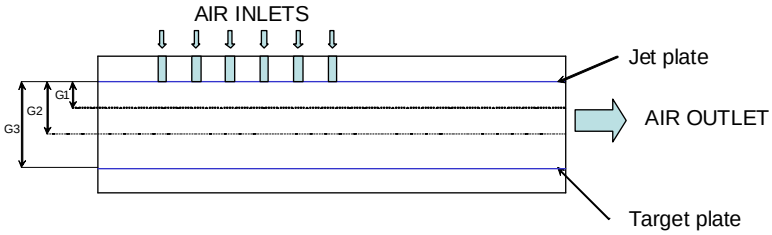

Fig. 2. Cross section of the domain.

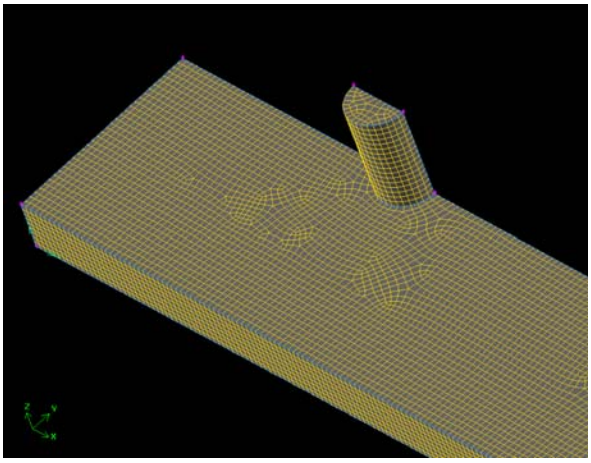

Fig. 3. Detailed grid topology for one of the jet in the investigated domain.

boundary condition on the main area of interest. Due to symmetry, only half of the channel was used to reduce the computational domain and grid size. The effects of distance between the jet issuing plate and jet impinging plate were evaluated based on three different spacings, as presented in Table 1. Figure 2 shows the planar view of cross section along the axial direction. The magnitudes of G1, G2, and G3 represent the physical distance between the jet exit and the target wall.

The domain is meshed by a grid generator GAMBIT associated with FLUENT, which consists of 176,569 nodes and 148,068 elements. The numerical grids were meshed using hexahedral elements and the grid topology as shown in Fig. 3. No-slip boundary condition was imposed on the walls. The turbulence intensity at both inlet and outlet is set at 5%. Air, as the working fluid, was assumed incompressible, but the properties other than density were treated as temperature-dependent. Modeling of turbulence used the standard k-ε model. A converged solution was obtained when the residuals were less than 10^{-6} in the energy equation and 10^{-3} in the momentum, continuity, and turbulence equations.

3. EXPERIMENTAL STUDY

The experiments complementary to the numerical study used a test setup schematically shown in Fig. 4. The supply of the mainstream air flow utilized an in-house air compressor, metered using an ASME orifice. Prior to the experiment, air is ducted away, using solenoid valves, from the test section while being heated by a series of in-line electric heaters. The air temperature is controlled using a variable transformer connected to the heaters. When the diverted air stream reached a desired steady temperature, the heated air was directed into the test section. The image of the test surface was captured with a CCD camera mounted perpendicular to the test section.

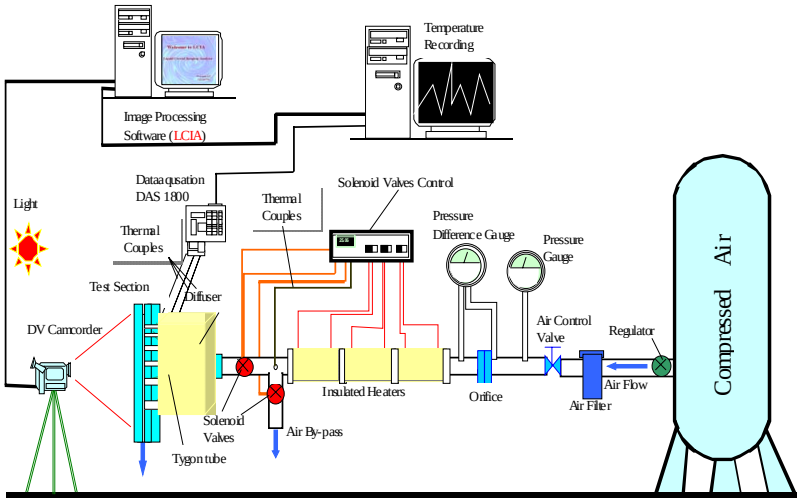

Fig. 4. The experimental setup.

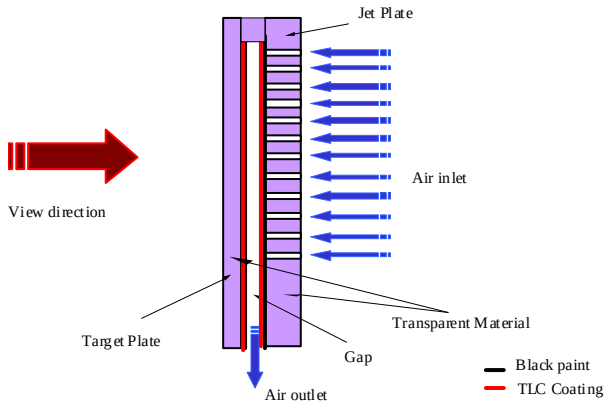

Fig. 5. Cross-sectional view of test section.

Simultaneously, the air temperature profile in the test section was measured using thermocouples connected to the data acquisition and storage systems.

The test section, a rectangular channel 50.8 mm wide and 457.2 mm long, is made of 12.7 mm thick Plexiglas. The jet issuing plate houses six in-line circular jet holes of 7.9 mm in diameter. The distance between jet issuing plate and the jet impinging plate ranges from 6.4 mm to 19.1 mm. Details of other parameters are presented in Tables 1 and 2. To simulate the crossflow, one side of the channel end is closed and the other side is open for crossflow discharge. The gap between the jet plate and the target plate ranges from 6.4 to 19.1 mm. Figure 5 illustrates the side view of the channel cross section, indicating the setting of a six-jet array and crossflow.

The measurement of local heat transfer coefficient employed the transient liquid crystal technique in conjunction with the solution of one-dimensional transient heat conduction in a semi-infinite solid by Metzger and Larson [15] and Chyu et.al. [16]. Under a convection boundary condition at its surface, the temperature on the surface of a semi-infinite solid, T_w, can be expressed by

Table 2.
Boundary inlet conditions

Inlet and outlet hydraulic diameters			1		2		3		4		5	
	D_{hi}, mm	D_{ho}, mm	V_{jet1}, m/s	R_{e1}	V_{jet2}, m/s	R_{e2}	V_{jet3}, m/s	R_{e3}	V_{jet4}, m/s	R_{e4}	V_{jet5}, m/s	R_{e5}
G1, 6.4 mm	7.94	10.22	29.32	14,000	45.10	22,000	57.14	28,000	67.44	34,000	76.74	40,000
G2, 12.7 mm	7.94	16.93	29.32	14,000	45.10	22,000	57.14	28,000	67.44	34,000	76.74	40,000
G3, 19.1 mm	7.94	21.80	29.32	14,000	45.10	22,000	57.14	28,000	67.44	34,000	76.74	40,000

$$\frac{T_w - T_i}{T_r - T_i} = \exp\left(\frac{h^2 \alpha t}{k^2}\right) erf\left(\frac{h\sqrt{\alpha t}}{k}\right). \quad (1)$$

T_i represents the initial temperature of the solid; T_r is the reference temperature for the convection system, which is chosen as the jet temperature T_j; h is the convective heat transfer coefficient based on T_w and T_r (or T_j); k and α are the thermal conductivity and diffusivity of the solid, respectively.

4. RESULTS AND DISCUSSION

4.1 Local Heat Transfer Coefficient

Figure 6 shows the distributions of local heat transfer coefficient on both target plate (a, b) and jet plate (c, d) obtained experimentally for Re = 14,000 to 40,000.

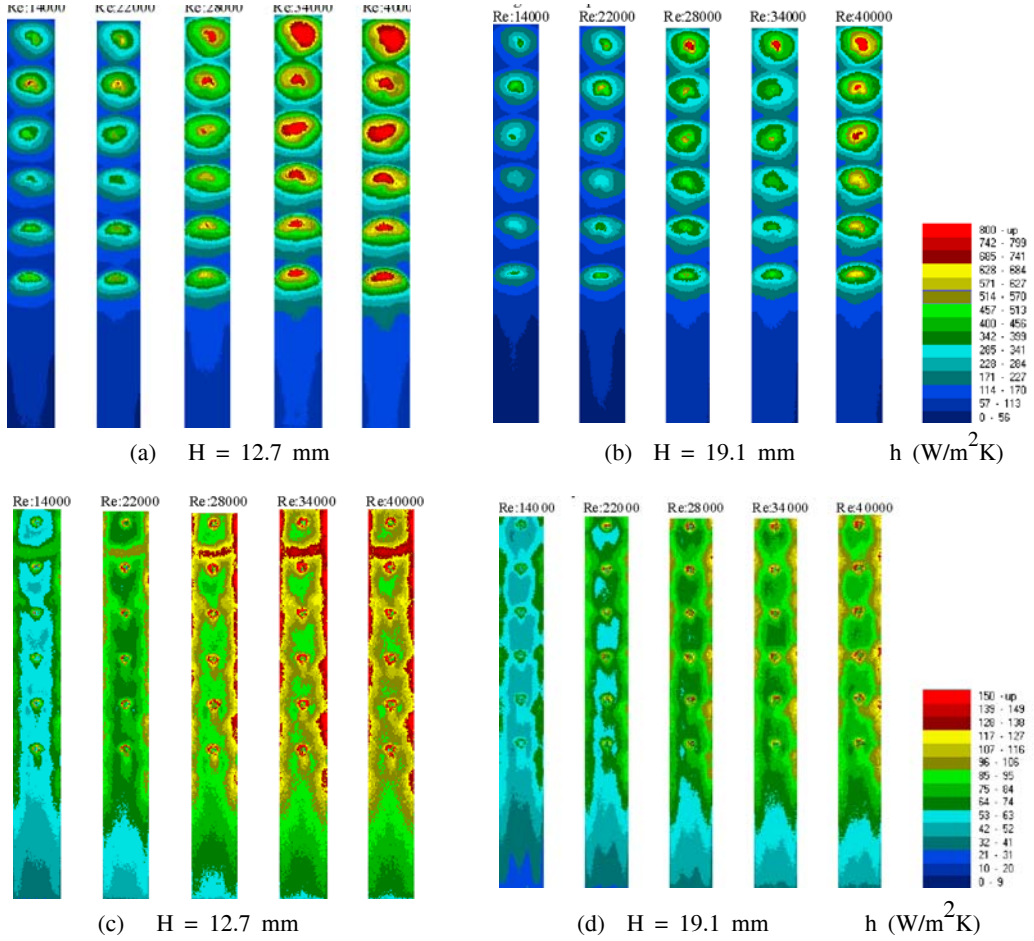

(a) H = 12.7 mm (b) H = 19.1 mm h (W/m^{2}K)

(c) H = 12.7 mm (d) H = 19.1 mm h (W/m^{2}K)

Fig. 6. Local heat transfer coefficients distribution on jet impinging plate (a, b) and jet issuing plate (experimental results) (c, d).

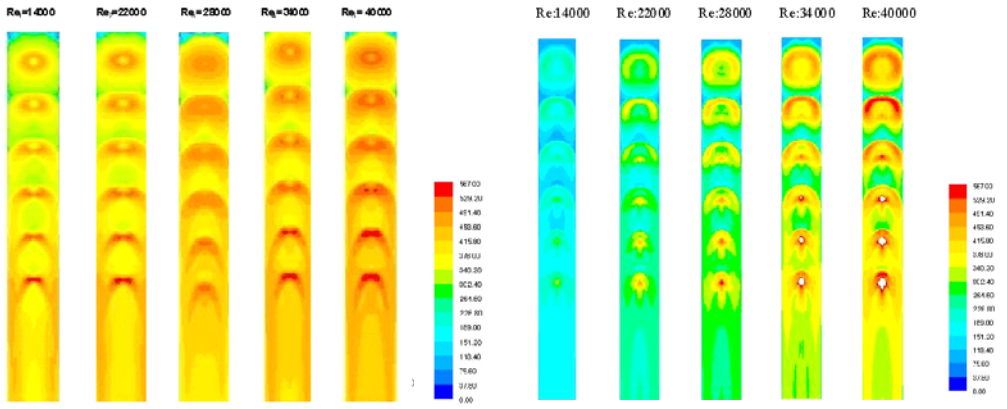

(a) H = 12.7 mm h (W/m^{2}K) (b) H = 19.1 mm h (W/m^{2}K)

Fig. 7. Local heat transfer coefficients distribution on jet impinging plate (numerical results).

The Reynolds number is defined based on jet mean velocity and hydraulic diameter of the housed channel.

One significant trend revealed in Fig. 6a and b is that the heat transfer coefficient on the target plate reaches a peak value at the stagnation zone directly impinged by each jet. In between the jets, the heat transfer is rather low, about 50% of that at the stagnation zone. Unlike the single impinging jet cases, part of the post-impingement flow tends to entrain back to the region between the adjacent jets, which likely results in low heat transfer in the region. All cases presented in Fig. 6 reveal a similar trend, and the local heat transfer coefficient tends to increase with Re.

Figure 7a and b exhibits the numerically simulated local distributions of heat transfer coefficient corresponding to the experimental data shown in Fig. 6c and d. Both results are comparable in distribution trend and detailed magnitude. Although no other Reynolds number cases are shown here, the value of heat transfer coefficient on the jet impinging plate tends to increase with Re.

Figures 8 and 9 show the streamwise-averaged Nusselt number for both jet target plate and jet issuing plate. The overall comparisons reveal that the heat transfer from the jet target plate is about 2 to 3 times higher as compared to the Dittus-Boelter correlations ($Nu = 0.023Re^{0.8}Pr^{0.4}$) and 3 to 4 times higher than the jet issuing plate. From Fig. 8, the results show that the crossflow effects are not evident for the target plate, as the heat transfer reaches a peak in the vicinity of each individual jet. In addition, at each stagnation zone, the heat transfer coefficient is about 2 times higher than the wall jet region. The Nusselt number is significantly reduced after the 6th jet. The influence of crossflow is clearly visible in both Figs. 8 and 9 as the peaks of Nusselt number on the target plate shift toward downstream, following the exit direction of the crossflow. The heat transfer distribution for the jet issuing plate is fairly uniform in the jets region up to about H/D_h = 2.5.

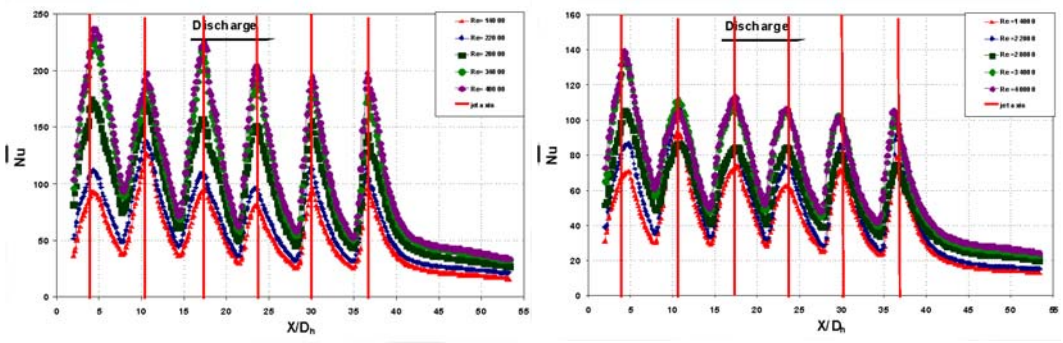

(a) H = 12.7 mm (b) H = 19.1 mm

Fig. 8. Streamwise-averaged Nu for jet impinging plate (experimental results) (a, b).

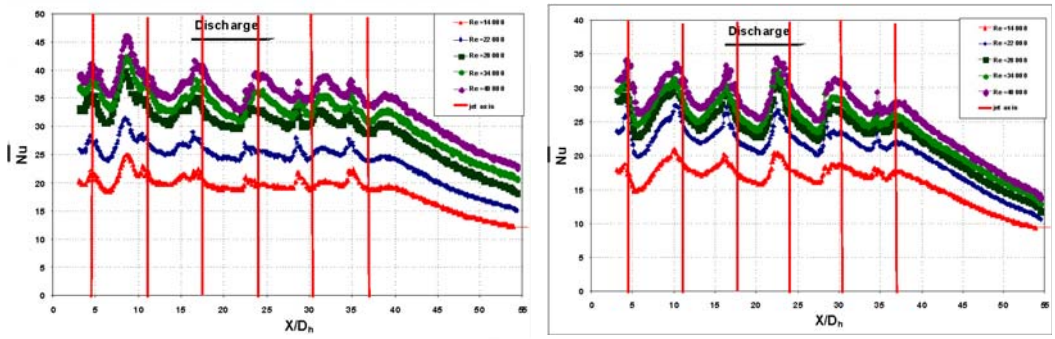

(a) H = 12.7 mm (b) H = 19.1 mm

Fig. 9. Streamwise-averaged Nu for jet issuing plate (experimental results) (a, b).

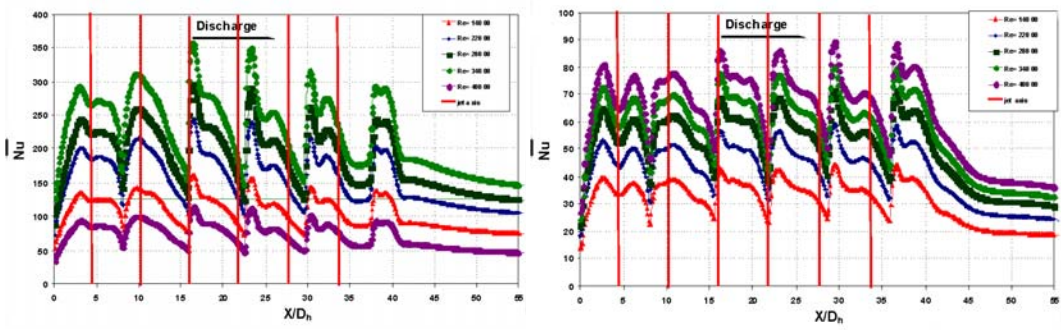

(a) H = 12.7 mm (b) H = 19.1 mm

Fig. 10. Streamwise-averaged Nu for target plate (numerical results) (a, b).

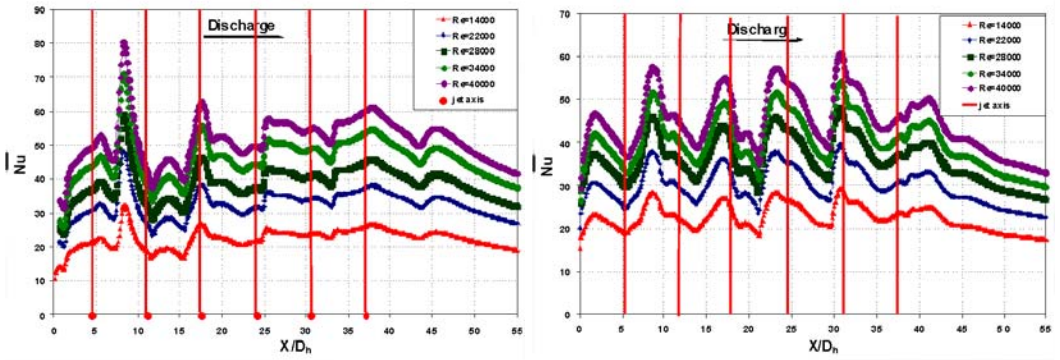

(a) H = 12.7 mm (b) H = 19.1 mm

Fig. 11. Streamwise-averaged Nu for jet issuing plate (numerical results).

The numerical results shown in Figs. 10 and 11 are plotted in the same manner as in Figs. 8 and 9 for direct comparison. A notable finding observed in Fig. 11 is that, for all cases, the value of heat transfer reaches a peak in between the first and second jets. This may be induced by the interaction between the jets that deflected some of the flow towards the jet issuing plate, which, in turn, contribute to higher heat transfer. Such effects seem to decrease towards the downstream region. Overall, the comparison between the numerical and experimental results for the jet issuing plate is quite reasonable, with an exception that the peak Nusselt number around the second jet obtained numerically is about 50% higher than its experimental counterpart.

4.2 Distance Effect between Jet Issuing Plate and Jet Impinging Plate

The overall-averaged h_{ave} based on all data, collected from this study, can be correlated in a h_{ave} H/D_h power form, as shown in Fig. 12. The heat transfer on the jet target plate is about 50% higher than the jet issuing plate. A significant findings revealed from Fig. 12 is that the overall heat transfer coefficient tends to increase as the distance between the two plates decreases. However, this is only observed for

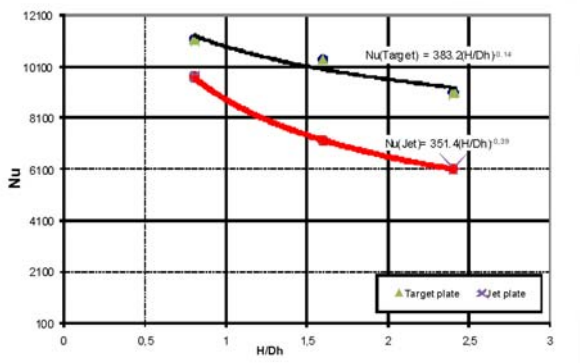

Fig. 12. Overall averaged Nu vs. H/D_h.

H/D_h up to about 2.5. For H/D_h higher than 2.5, the overall heat transfer coefficient seems to be converged towards a constant value. This may be due to the shrinkage of the flow areas in jet system as the distance (H) between the jet and target plate decreases. A best fit correlation for Re = 40,000 can be given as follows:

$$\mathrm{Nu}(Target) = 383.2\cdot(H/D_h)^{-0.14} \quad \text{for the target plate,}$$

$$\mathrm{Nu}(Jet) = 351.5\cdot(H/D_h)^{-0.39} \quad \text{for the jet issuing plate.}$$

Adversely, the jet cannot penetrate the target plate as the distance is too great. This is consistent with the study of Brevet et al. [17]. Therefore, H/D_h in the range of 2.5 to 3 could be the optimal configuration for jet impingement cooling with crossflow.

5. CONCLUSIONS

In the present study, the heat transfer characteristics in a rectangular duct with jet impingement are explored experimentally and computationally for 14,000 < Re < 40,000. Detailed local heat transfer distributions over major participating surfaces, i.e., both jet target plate and jet issuing plate, are presented. While the average results from the experiments and computations are reasonably comparable, local peak data from the computation can be 15–50% higher than their experimental counterparts. This is due largely to the imperfection of turbulence modeling. Major findings from the present study can be summarized below.

(1) The magnitude of average heat transfer on the target plate is about 2–3 times higher than the Dittus–Boelter correlation for a smooth channel. Meanwhile, the magnitude of average heat transfer on the jet issuing plate is comparable to that of Dittus–Boelter correlation.
(2) Crossflow significantly reduces heat transfer on the target plate, as the streamwise-resolved heat transfer decreases along the crossflow direction toward the channel exit.
(3) Crossflow also causes reduction of heat transfer on the jet issuing plate. However, the effect is much moderate compared to the target plate.
(4) The magnitude of heat transfer on both the target plate and jet issuing plate increases with the value of Reynolds number.
(5) The value of overall heat transfer over all the participating surfaces in the house channel decreases with an increase in jet-to-target spacing (H/D_h). Under the current geometry and test conditions, this trend somewhat diminishes as the average Nusselt number reaches a constant when H/D_h is higher than 2.5.

NOMENCLATURE

h	local heat transfer coefficient, $W/m^2\cdot K$
T_w	local surface temperature, K

k	thermal conductivity, W/m·K
T_i	initial temperature, K
D_h	hydraulic diameter, m
D_{hi}	inlet hydraulic diameter, m
D_{ho}	outlet hydraulic diameter, m
Nu	Nussellt number, = hD_h/k
Re	Reynolds number, = VD_h/ν
V_{jet}	velocity in jet inlets, m/s
TLC	Thermochromic Liquid Crystal
H	jet-target space, m
G	jet-target space, m
S	space between jets, m
X	axial location, m

Greek symbol

ν	kinematic viscosity, m^2/s.

REFERENCES

1. Uysal, U., Li, P. W., Chyu, M. K., and Cuhna, F. J. Heat transfer on internal surfaces of a duct subjected to impingement of a jet array with varying jet hole-size and spacing, *ASME J. Turbomachinery*, 2006 Vol. 128, No. 1, pp. 158–165.
2. Lim, K. B. and Lee, C. H. An experimental study on the characteristics of heat transfer on the turbulent round impingement jet according to the inclined angle of convex surface using the liquid crystal transient method, *Exp. Thermal Fluid Sci*., 2006, Vol. 31, pp. 711–719.
3. Huang, Y., Ekkad, S. V., and Han, J. C. Detailed heat transfer distributions under an array of orthogonal impinging jets, *J. Thermophys. Heat Transfer*, 1998, Vol. 12, No. 1, pp. 73–79.
4. Ichimiya, K. and Yamada, Y. Three-dimensional heat transfer of confined circular impinging jet with buoyancy effects, *Trans. ASME*, *J. Heat Transfer*, 2003, Vol. 125, pp. 250–257.
5. Aldabbagh, I., Sezai, I. and MOHAMMAD, A. A. Three-dimensional investigation of a laminar impinging square jet interaction with crossflow, *J. Heat Transfer*, 2003, Vol. 125, pp. 243–249,
6. San, J. Y. and. Lai, M. D. Optimum jet to jet spacing of heat transfer for staggered arrays of impinging air jets, *Heat Mass Transfer*, 2001, Vol. 44, pp. 3997–4007.
7. Azad, G. M. S., Huang, Y., and Han, J. C. Impingement heat transfer on dimpled surface using a transient liquid crystal technique, *J. Thermophys. Heat Transfer*, 2000, Vol. 14, No. 2, pp. 186–193.

8. Di Ai, Ding, P. P., and Chen, P. H. The selection criterion of injection temperature pair for transient liquid crystal thermograph on film cooling measurements, *Heat Mass Transfer*, 2001, Vol. 44, pp. 1389–1399.
9. Lee, J. and Lee, S.-J., Stagnation region heat transfer of a turbulent axisymetric jet impingement experimental, *Heat Transfer*, 1999, Vol. 12, pp. 137–156.
10. Gao, L. and Ekkad, S. V. Impingement heat transfer under linearly stretched arrays of holes. In: *Proc. ASME Turbo Expo 2003*, June 16–19, Atlanta, Georgia, USA.
11. Muhammad, M. R. and Raghavan, J. Transient response of protruding electronic modules exposed to horizontal crossflow, *Int. J. Heat Fluid Flow*, 1999, Vol. 20, pp. 48–59.
12. Kiger, T. and Jungho, K. Single nozzle spray cooling heat tansfer mechanism, *Int. J. Heat Mass Transfer*, 2005, Vol. 48, pp. 1425–1438.
13. Zuckermann, N. and Lior, N. Impingement heat transfer: correlations and numerical modeling, *J. Heat Transfer*, 2005, Vol. 127, pp. 544–552.
14. Viskanta, R. Heat transfer to impinging isothermal gas and flame jets, *J. Exp. Thermal Fluid Sci.*, 1993, Vol. 6, pp. 111–134.
15. Metzger, D. E. and Larson, D. E. Use of melting point surface coatings for local convection heat transfer measurements in rectangular channel flows with 90-deg turns, *J. Heat Transfer*, 1986, Vol. 108, pp. 48–54.
16. Chyu, M. K., Ding, H., Downs, J. P., and Soechting, F. O. Determination of local heat transfer coefficient based on bulk mean temperature using a transient liquid crystals technique, *J. Exp. Thermal Fluid Sci.*, 1998, Vol. 18, pp. 142–149.
17. Brevet, P., Dejeu, C., Dorignac, E., Jolly, M., and Vullierme, J. J. Heat transfer to arrow of impinging jets in consideration of optimization, *Int. J. Heat Mass Transfer*, 2002, Vol. 45, pp. 4191–4200.

□◆◆◆□

HEAT TRANSFER RESEARCH

Guest Editors:
Terrence W. Simon & Richard J. Goldstein

Volume 41, Number 6 2010

Special Issue 1 of 5:
Turbine-09 symposium, Antalya, Turkey, August 9–14, 2009

Preface: Gas Turbine Heat Transfer

Film Cooling Simulation and Control
S. Acharya

Film Cooling: Breaking the Limits of Diffusion Shaped Holes
R.S. Bunker

Effect of Gap Geometry on the Cooling Effectiveness of the Wheelspace Coolant Injection Upstream of a Row of Rotor Blades
M. Papa, V. Srinivasan, R.J. Goldstein, and F. Gori

An Experimental and Numerical Investigation of Impingement Heat Transfer in Airfoils Leading-Edge Cooling Channel
M.E. Taslim and A. Abdelrasoul

A Correlation-Based Methodology to Predict the Flow Structure of Flows Emanating from Cylindrical Holes with Application to Film Cooling
S.A.D. Kampe and S. Völker

Volume 41, Number 7 2010

Special Issue 2 of 5:
Turbine-09 symposium, Antalya, Turkey, August 9–14, 2009

Preface: Gas Turbine Heat Transfer

Turbine Aero-Heat Transfer Studies in Rotating Research Facilities
C. Camci

Turbine Airfoil Aerothermal Characteristics in Future Coal–Gas-Based Power Generation Systems
M. K. Chyu and M. A. Alvin

Investigation of Film-Cooled Rough Surfaces Using Large Eddy Simulation
P. Kalghatgi and S. Acharya

Effect of Internal Rib Configurations on the Discharge Coefficient of a 30^{o} Inclined Film Cooling Hole
C. Heneka, A. Schulz, and H.-J. Bauer

PIV Measurements of the Flow in a Rotating Cavity with a Radial Inflow
X. Yu, X. Luo, J. N. Sun, G. Q. Xu, H. W. Deng, and E. N. Shen

Volume 41, Number 8 2010

Special Issue 3 of 5:
Turbine-09 symposium, Antalya, Turkey, August 9–14, 2009

Preface: Gas Turbine Heat Transfer

Recent Studies in Turbine Blade Internal Cooling
J-C. Han and M. Huh

Heat Transfer and Flow Testing in Engine HP Turbine Cooling System Development
P. Ireland, V. Mittal, D. Jackson, and H. Namgoon

Trailing Edge Film Cooling of Gas Turbine Airfoils-Effects of Ejection Lip Geometry on File Cooling Effectiveness and Heat Transfer
T. Horbach, A. Schulz, and H-J. Bauer

An Experimental Study of Airfoil and Endwall Heat Transfer on a Linear Turbine Blade Cascade-Secondary Flow and Surface Roughness Effects
M. Lorenz, A. Schulz, and H-J. Bauer

Experimental Study of Heat Transfer from Impinging Jet with Upstream and Downstream Crossflow
D. Thibault, M. Fénot, G. Lalizel, and E. Dorignac

Experimental and Theoretical Analysis of Heat Transfer Characteristics in a Rectangular Duct with Jet Impingement
U.Uysal, F. Sahin, and M.K. Chyu

Volume 42, Number 1 2011

Special Issue 4 of 5:
Turbine-09 symposium, Antalya, Turkey, August 9–14, 2009

Preface: Gas Turbine Heat Transfer

Turbine Airfoil Leading-Edge Stagnation Aerodynamics and Heat Transfer - A Review
L.S. Langston and B.M. Holley

Recent Progress in Numerical Simulation of Highly Three-Dimensional Turbulent Flows and Endwall Heat Transfer in Turbine Blade Cascades
E. M. Smirnov

Effects of Stator/Rotor Leakage Flow and Axisymmetric Contouring on Endwall Adiabatic Effectiveness and Aerodynamic Loss
R. Erickson and T. Simon

Augmented Heat Transfer of an Internal Blade Tip by Full or Partial Arrays of Pin-Fins
G. Xie, B. Sunden, L. Wang and E. Utriainen

Study on the Thermal and Flow Fields of Shaped Film Cooling Holes
K. Takeishi, T. Kitamura, M. Komiyama, Y. Oda, and S. Mori

Volume 42, Number 2 2011

Special Issue 5 of 5:
Turbine-09 symposium, Antalya, Turkey, August 9–14, 2009

Preface: Gas Turbine Heat Transfer

Multiple Jet Impingement-A Review
B. Weigand and S. Spring

Influence of Internal Cyclone Flow on Adiabatic Film Cooling Effectiveness
A. Lerch and H.-P. Schiffer

Advanced Aero-Thermal Investigation of High Pressure Turbine Tip Flows
P. Vass and T. Arts

Liquid Crystal Thermography for Transient Heat Transfer Measurements in Complex Internal Cooling Systems
R. Poser and J. von Wolfersdorf

HEAT TRANSFER RESEARCH

Volume 41 Contents 2010

Number 1

1 Generation of Helicity and the Critical Transitions in a Twisted Flow of a Single-Phase Liquid
O.V. Mitrofanova

21 Heat Transfer in Rough Tubes with an Inserted Twisted Tape
G.K. Il'in, S.É. Tarasevich, A.V. Shchelchkov, and *A.B. Yakovlev*

33 Experimental Study of the Influence of a Twisted Tape on Local Heat Transfer
A.N. Varava, A.V. Dedov, E.M. Zakharov, A.T. Komov, and *S.A. Malakhovskii*

41 Mathematical Simulation of a Twisted Flow in a Cylindrical-Conical Hydrocyclone
R.I. Ibyatov, L.P. Kholpanov, and *T.Sh. Murtazin*

59 Correlation of Data on the Critical Heat Loads in the Case of Flow Twisting in Straight and Helical Tubes
A.F. Krug, Yu.A. Kuzma-Kichta, and *A.S. Komendantov*

75 Processes in the Two-Phase Layer Near the Heated Surface of the Ocean and Generation of Atmospheric Vortices
O.A. Sinkevich, V.V. Glazkov, and *S.E. Chikunov*

93 Investigation of Near-Wall Turbulent Flows in a Vortex Chamber
É.P. Volchkov, V.V. Lukashov, R.Kh. Abdrakhmanov, and *A.D. Bogdanova*

Number 2

107 Natural Convective Heat and Fluid Flow in a Two-Dimensional Enclosure with an Isoflux Partition Utilizing Different Fluids
S.H. Anilkumar and *B.T. Kuzhiveli*

129 Modes of Heat Transfer in the Leidenfrost Effect
R.I. Rabady

137 Numerical Study of Buoyancy-Opposed Wall Jet Flow
A. Abdel-Fattah

155 Highly Nonlinear Temperature-Dependent Fin Analysis by Variational Iteration Method
F. Fouladi, E. Hosseinzadeh, A. Barari, and *G. Domairry*

167 The Effect of Suspended Particles on Marginal Stability of Magnetized Ferrofluid with Internal Angular Momentum
S. Kumar, P. Chand, and *A. Mahajan*

187 Flow Diverter Optimum Angle to Enhance Free Convection Heat Transfer from a Vertical Array of Isothermal Tubes
M. Ashjaee, S. Farahmand, E. Chavoshi, and *T. Yousefi*

Number 3

207 Preface

209 Experiments and Simulations in Transient Conjugated Conduction-Convection-Radiation
C.P. Naveira-Cotta, M. Lachi, M. Rebay, and *R.M. Cotta*

233 Numerical Modeling and Parametric Studies of Steam Reformers
C. Ventura and *J.L.T. Azevedo*

247 Numerical Resolution of Conjugate Heat Transfer Problem in a Parallel-Plate Micro-Channel
Y. Kabar, M. Rebay, M. Kadja, and *C. Padet*

265 Minimum of Exergy Consumption in a Horizontal Fluidized Heat Exchanger
A. Poświata and *Z. Szwast*

283 Theoretical and Experimental Study of a Water Phase-Change Solar Collector
A. Thiam, Y. Mandiang, D. Azilinon, V. Sambou, and *M. Adj*

299 Experiments on Natural Convection Heat Transfer from an Isothermal Plate on a Semi-Infinite Surface and from a Constrained Horizontal Plate in Air
C. Oleskowicz-Popiel and *J. Wojtkowiak*

313 Pitchfork Bifurcation of the Mixed Convection in a Vertical Channel
O. Kholai, S. Boudebous, Z. Nemouchi, and *M. Rebay*

325 Dynamic Characterization of Adsorption in Metal Hydrides
C. Sobrinho, N. Santos, and *J.L.T. Azevedo*

339 Experimental Study on Thermal Conductivity and Viscosity of Water-Based Nanofluids
I. Tavman, A. Turgut, M. Chirtoc, K. Hadjov, O. Fudym, and *S. Tavman*

Number 4

353 Formation of Vortex Structures in a Vertical Enclosure with Finning of Its Both Walls
VV. Terekhov and *V.I. Terekhov*

369 Heat Transfer in Boiling of a Moving Liquid in a Microchannel
V.V. Kuznetsov and *A S. Shamirzaev*

389 Aerodynamics and Heat Transfer on Impingement of Twisted Impact Jets on Spherical Cavities
V.I. Terekhov and *Yu.M. Mshvidobadze*

401 Reduction of Resistance and Heat Transfer Enhancement in Flow Past a Cylinder with Jet and Vortex Generators
T.A. Baranova, V.L. Zhdanov, Yu.V. Zhukova, and *S.A. Isaev*

413 Vortical Intensification of Heat Transfer in Microchannels with Oval Dimples
S.A. Isaev, E. Leonardi, V. Timchenko, and *A.E. Usachov*

425 Experimental Verification of the Methods of Calculation of a Flow and Mixing of a Gaseous Fuel Behind a Swirling Frontal Module
V.V. Tret'yakov, A.K. Mironov, and *V.P. Maslov*

445 Experimental Modeling of the Structure of a Reacting Twisted Flow Behind a Swirl Burner
S.V. Alekseenko, V.M. Dulin, Yu.S. Kozorezov, D.M. Markovich, M.P. Tokarev, and *S.I. Shtork*

465 Vortex Precession in a Gas–Liquid Flow
S.V. Alekseenko, P.A. Kuibin, V.L. Okulov, and *S.I. Shtork*

479 Investigation of Nonstationary Heat Transfer in Boiling of Freon 113 on Dimpled Spherical and Cylindrical Surfaces under the Conditions of Free Convection
V.M. Zhukov, Yu.A. Kuzma-Kichta, and *A.M. Agal'tsov*

Number 5

493 Influence of Torsion on the Laminar Flow and Convective Heat Transfer in Coiled Tubes Arranged in a Rectangular Pattern
I. Conté, X.-f. Peng, and *A. Campo*

509 Numerical Investigations of Opposing Mixed Convection Heat Transfer in Vertical Flat Channel.
1. Laminar Mixed Convection and Transition to Vortex Flow in the Case of Symmetrical Heating
A. Sirvydas and *R. Pos(kas*

521 Numerical Investigations of Opposing Mixed Convection Heat Transfer in a Vertical Flat Channel.
2. Vortex Flow in the Case of Symmetrical Heating
A. Sirvydas and *R. Pos(kas*

531 Dimensionless Local and Average Boiling Heat Transfer Correlation for Saturated Liquids
M.K. Das, S.C. Gupta, and *V.K. Agarwal*

559 Comparison of Analytical and Experimental Data for Shear Stresses on Fuel Rods
B. Cesna

573 Augmentation or Suppression of Natural Convective Heat Transfer in Horizontal Annuli Filled with Air and Partially Filled with a Porous Matrix Layer
M. Ait Saada, S. Chikh, and *A. Campo*

Number 6

Special Issue 1 of 5:
Turbine-09 symposium, Antalya, Turkey, August 9–14, 2009

Guest Editors:
Terrence W. Simon & Richard J. Goldstein

599 Preface: Gas Turbine Heat Transfer

601 Film Cooling Simulation and Control
S. Acharya

627 Film Cooling: Breaking the Limits of Diffusion Shaped Holes
R.S. Bunker

651 Effect of Gap Geometry on the Cooling Effectiveness of the Wheelspace Coolant Injection Upstream of a Row of Rotor Blades
M. Papa, V. Srinivasan, R.J. Goldstein, and F. Gori

669 An Experimental and Numerical Investigation of Impingement Heat Transfer in Airfoils Leading-Edge Cooling Channel
M.E. Taslim and A. Abdelrasoul

687 A Correlation-Based Methodology to Predict the Flow Structure of Flows Emanating from Cylindrical Holes with Application to Film Cooling
S.A.D. Kampe and S. Völker

Number 7

Special Issue 2 of 5:
Turbine-09 symposium, Antalya, Turkey, August 9–14, 2009

Guest Editors:
Terrence W. Simon & Richard J. Goldstein

701 Preface: Gas Turbine Heat Transfer

703 Turbine Aero-Heat Transfer Studies in Rotating Research Facilities
C. Camci

737 Turbine Airfoil Aerothermal Characteristics in Future Coal–Gas-Based Power Generation Systems
M.K. Chyu and M.A. Alvin

753 Investigation of Film-Cooled Rough Surfaces Using Large Eddy Simulation
P. Kalghatgi and S. Acharya

769 Effect of Internal Rib Configurations on the Discharge Coefficient of a 30°-Inclined Film Cooling Hole
C. Heneka, A. Schulz, and H.-J. Bauer

787 PIV Measurements of the Flow in a Rotating Cavity with a Radial Inflow
X. Yu, X. Luo, J.N. Sun, G.Q. Xu, H W. Deng, and E.N. Shen

Number 8

Special Issue 3 of 5:
Turbine-09 symposium, Antalya, Turkey, August 9–14, 2009

Guest Editors:
Terrence W. Simon & Richard J. Goldstein

801 Preface: Gas Turbine Heat Transfer

803 Recent Studies in Turbine Blade Internal Cooling
J-C. Han and M. Huh

829 Heat Transfer and Flow Testing in Engine HP Turbine Cooling System Development
P. Ireland, V. Mittal, D. Jackson, and H. Namgoon

849 Trailing Edge Film Cooling of Gas Turbine Airfoils-Effects of Ejection Lip Geometry on File Cooling Effectiveness and Heat Transfer
T. Horbach, A. Schulz, and H-J. Bauer

867 An Experimental Study of Airfoil and Endwall Heat Transfer on a Linear Turbine Blade Cascade-Secondary Flow and Surface Roughness Effects
M. Lorenz, A. Schulz, and H-J. Bauer

889 Experimental Study of Heat Transfer from Impinging Jet with Upstream and Downstream Crossflow
D. Thibault, M. Fénot, G. Lalizel, and E. Dorignac

901 Experimental and Theoretical Analysis of Heat Transfer Characteristics in a Rectangular Duct with Jet Impingement
U.Uysal, F. Sahin, and M.K. Chyu

HEAT TRANSFER RESEARCH

Volume 41 Author Index 2010

Abdel-Fattah, A., 137
Abdelrasoul, A., 669
Abdrakhmanov, R.Kh., 93
Acharya, S., 601, 753
Adj, M., 283
Agal'tsov, A.M., 479
Agarwal, V.K., 531
Ait Saada, M., 573
Alekseenko, S.V., 445, 465
Alvin, M.A., 373
Anilkumar, S.H., 107
Ashjaee, M., 187
Azevedo, J.L.T., 233, 325
Azilinon, D., 283

Baranova, T.A., 401
Barari, A., 155
Bauer, H.-J., 769, 849,
867Bogdanova, A.D., 93
Boudebous, S., 313
Bunker, R.S., 627

Camci, C., 703
Campo, A., 493, 573
Cesna, B., 559
Chand, P., 167
Chavoshi, E., 187
Chikh, S., 573
Chikunov, S.E., 75
Chirtoc, M., 339
Chyu, M.K., 737, 901
Conté, I., 493
Cotta, R.M., 209

Das, M.K., 531
Dedov, A.V., 33
Deng, H W., 787
Domairry, G., 155
Dorignac, E., 889
Dulin, V.M., 445

Farahmand, S., 187
Fénot, M., 889
Fouladi, F., 155
Fudym,O., 339

Glazkov, V.V., 75
Goldstein, R.J., 599, 651, 701, 801
Gori, F., 651
Gupta, S.C., 531

Hadjov, K., 339
Han, J-C., 803
Heneka, C., 769
Horbach, T., 849
Hosseinzadeh, E., 155
Huh, M. 803

Ibyatov, R.I., 41
Il'in, G.K., 21
Ireland,P., 829
Isaev, S.A., 401, 413

Jackson, D., 829

Kabar, Y., 247
Kadja, M., 247
Kalghatgi, P. 753
Kampe, S.A.D., 687
Kholai, O., 313
Kholpanov,L.P., 41
Komendantov, A.S., 59
Komov, A.T., 33
Kozorezov, Yu.S. , 445
Krug, A.F., 59
Kuibin, P.A., 465
Kumar, S., 167
Kuzhiveli, B.T., 107
Kuzma-Kichta, Yu.A., 59, 479
Kuznetsov, V.V., 369

Lachi, M., 209
Lalizel, G., 889
Leonardi, E., 413
Lorenz, M., 867
Lukashov, V.V., 93
Luo, X., 787

Mahajan, A., 167
Malakhovskii, S.A., 33
Mandiang, Y., 283
Markovich, D.M., 445
Maslov, V.P., 425
Mironov, A.K., 425
Mitrofanova, O.V., 1
Mittal, V., 829
Mshvidobadze, Yu.M., 389
Murtazin, T.Sh., 41

Namgoon, H., 829
Naveira-Cotta, C.P., 209
Nemouchi, Z., 313

Okulov, V.L., 465
Oleskowicz-Popiel, C., 299

Padet, C., 247
Papa, M., 651
Peng, X.-F., 493
Pos(kas, R., 509, 521
Poświata, A,. 265

Rabady, R.I., 129
Rebay, M., 209, 247, 313

Sahin, F., 901
Sambou, V., 283
Santos, N., 325
Schulz, A., 769, 849, 867
Shamirzaev, A S., 369
Shchelchkov, A.V., 21
Shen, E.N., 787
Shtork, S.I., 445, 465
Simon, T.W., 599, 701, 801
Sinkevich,O.A., 75
Sirvydas, A., 509, 521
Sobrinho, C., 325
Srinivasan, V., 651
Sun, J.N., 787
Szwast, Z., 265

Tarasevich, S.É., 21
Taslim, M.E., 669
Tavman, I., 339
Tavman, S., 339
Terekhov, V.I., 353, 389
Terekhov, V.V., 353
Thiam, A., 283
Thibault, D., 889
Timchenko, V., 413
Tokarev, M.P., 445
Tret'yakov, V.V., 425
Turgut, A., 339

Usachov, A.E., 413
Uysal, U., 901

Varava, A.N., 33
Ventura, C., 233
Volchkov, É.P., 93
Völker, S., 687

Wojtkowiak, J., 299

Xu, G.Q., 787

Yakovlev, A.B., 21
Yousefi, T., 187
Yu, X., 787

Zakharov, E.M., 33
Zhdanov, V.L. , 401
Zhukov, V.M., 479
Zhukova, Yu.V., 401